12-2016

A Probabilistic-Based Approach to Monitoring Tool Wear State and Assessing Its Effect on Workpiece Quality in Nickel-Based Alloys

Farbod Akhavan Niaki
Clemson University, fakhava@g.clemson.edu

A PROBABILISTIC-BASED APPROACH TO MONITORING TOOL WEAR STATE AND ASSESSING ITS EFFECT ON WORKPIECE QUALITY IN NICKEL-BASED ALLOYS

A Dissertation
Presented to
the Graduate School of
Clemson University

In Partial Fulfillment
of the Requirements for the Degree
Doctor of Philosophy
Automotive Engineering

---

by
Farbod Akhavan Niaki
December 2016

Accepted by:
Dr. Laine Mears, Committee Chair
Dr. Sez Atamturktur
Dr. Beshah Ayalew
Dr. Joachim Taiber

ABSTRACT

The objective of this research is first to investigate the applicability and advantage of statistical state estimation methods for predicting tool wear in machining nickel-based superalloys over deterministic methods, and second to study the effects of cutting tool wear on the quality of the part. Nickel-based superalloys are among those classes of materials that are known as hard-to-machine alloys. These materials exhibit a unique combination of maintaining their strength at high temperature and have high resistance to corrosion and creep. These unique characteristics make them an ideal candidate for harsh environments like combustion chambers of gas turbines. However, the same characteristics that make nickel-based alloys suitable for aggressive conditions introduce difficulties when machining them. High strength and low thermal conductivity accelerate the cutting tool wear and increase the possibility of the in-process tool breakage. A blunt tool nominally deteriorates the surface integrity and damages quality of the machined part by inducing high tensile residual stresses, generating micro-cracks, altering the microstructure or leaving a poor roughness profile behind. As a consequence in this case, the expensive superalloy would have to be scrapped. The current dominant solution for industry is to sacrifice the productivity rate by replacing the tool in the early stages of its life or to choose conservative cutting conditions in order to lower the wear rate and preserve workpiece quality. Thus, monitoring the state of the cutting tool and estimating its effects on part quality is a critical task for increasing productivity and profitability in machining superalloys.

This work aims to first introduce a probabilistic-based framework for estimating tool wear in milling and turning of superalloys and second to study the detrimental effects of functional state of the cutting tool in terms of wear and wear rate on part quality. In the milling operation, the mechanisms of tool failure were first identified and, based on the rapid catastrophic failure of the tool, a Bayesian inference method (*i.e.*, Markov Chain Monte Carlo, MCMC) was used for parameter calibration of tool wear using a power mechanistic model. The calibrated model was then used in the state space probabilistic framework of a Kalman filter to estimate the tool flank wear. Furthermore, an on-machine laser measuring system was utilized and fused into the Kalman filter to improve the estimation accuracy. In the turning operation the behavior of progressive wear was investigated as well. Due to the nonlinear nature of wear in turning, an extended Kalman filter was designed for tracking progressive wear, and the results of the probabilistic-based method were compared with a deterministic technique, where significant improvement (more than 60% increase in estimation accuracy) was achieved. To fulfill the second objective of this research in understanding the underlying effects of wear on part quality in cutting nickel-based superalloys, a comprehensive study on surface roughness, dimensional integrity and residual stress was conducted. The estimated results derived from a probabilistic filter were used for finding the proper correlations between wear, surface roughness and dimensional integrity, along with a finite element simulation for predicting the residual stress profile for sharp and worn cutting tool conditions.

The output of this research provides the essential information on condition monitoring of the tool and its effects on product quality. The low-cost Hall effect sensor

used in this work to capture spindle power in the context of the stochastic filter can effectively estimate tool wear in both milling and turning operations, while the estimated wear can be used to generate knowledge of the state of workpiece surface integrity. Therefore the true functionality and efficiency of the tool in superalloy machining can be evaluated without additional high-cost sensing.

DEDICATIONS

To my MOTHER

For her unconditional love, support, and prayers

To My FATHER

For his support and guidance

ACKNOWLEDGMENTS

I would like to express my deepest appreciation to my advisor Dr. Laine Mears for his guidance and support through my PhD journey. It was a great honor working for you and thanks for letting me explore and experience. I am very grateful of the lessons you taught me both in research and real life.

Next, I would like to thank my dearest friend Dr. Durul Ulutan for his support, guidance and friendship in different stages of my PhD. Thanks for sharing your experiences with me and helping me make better decisions for my life. Also I want to thank my teammates Brandt, Vassilis, Abram, Mathew, Jamie, Lujia, and Martin for all of the support. I really enjoyed sharing many of the best moments of my life in United States with you.

I would like to thank Dr. Atamturktur for her time, comments, and detailed review of this manuscript, as well as Dr. Ayalew and Dr. Taiber of my research committee.

Last but not least, I am so grateful of my mom and dad for their support. Everything that I have in life is simply because of your support and prayers. Also, I would like to thank Sahba, for being the best sister anyone can dream of.

TABLE OF CONTENTS

Page

Table of Contents (Continued)

Page

Table of Contents (Continued)

Page

Table of Contents (Continued)

Page

LIST OF TABLES

Table Page

LIST OF FIGURES

Figure Page

List of Figures (Continued)

Figure Page

List of Figures (Continued)

Figure Page

List of Figures (Continued)

Figure Page

List of Figures (Continued)

Figure Page

List of Figures (Continued)

Figure Page

List of Figures (Continued)

Figure Page

List of Figures (Continued)

Figure Page

List of Figures (Continued)

Figure Page

List of Figures (Continued)

Figure Page

CHAPTER ONE

1. INTRODUCTION

Research Objective

The objective of this research is first to investigate the applicability and advantage of statistical state estimation methods for predicting tool wear in machining nickel-based superalloys over deterministic methods, and second to study the effects of cutting tool wear on the quality of the part. This work aims to describe cutting tool functionality in machining nickel-based superalloys as a combination of tooling condition and workpiece quality, in order to maximize the useful life of the tool, and to reduce tooling cost in addition to preserving the end-product quality. This is achieved by using stochastic-based filters for tracking progressive tool wear in both milling and turning operations by utilizing a low cost power sensing, followed by extensive experimental study for identifying the relationship of the tool wear and workpiece quality parameters, *i.e.*, surface roughness, dimensional tolerances and residual stresses.

Motivation

With advances in the aerospace and power generation industry designs, demand is increasing for materials with better fatigue and fracture resistance. Nickel-based superalloys are a special class of material with exceptional corrosion and temperature resistivity, which makes them an ideal candidate for manufacturing advanced engines or gas turbines. Therefore, there has been a rapid acceleration in development of a new generation of Ni-based alloys that can handle operational stresses at higher temperatures. As shown in Figure 1-1, advanced processing, alloy development, thermal barrier coating

and effective cooling schemes have led to a 4°F increase per year in temperature resistance capability of these materials [1]. Nickel-based superalloys are among those materials that are also classed as hard-to-machine alloys. These materials exhibit a unique combination of maintaining strength at high temperatures and high resistance to corrosion and creep. Therefore, more than 50% of a typical jet engine as shown in Figure 1-2, including turbine blades, turbine exhaust case and combustion chambers, are made of Ni-based alloys [2].

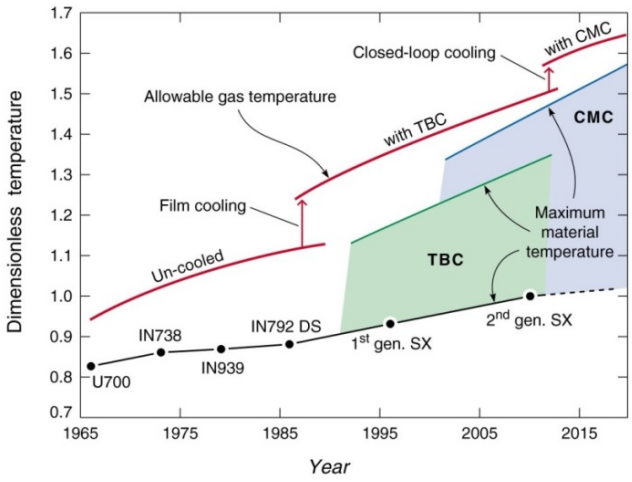

Figure 1-1: Increase in temperature resistance capability of Ni-based alloys (dimensionless temperature is the ratio of gas-to-metal temperature difference over gas-to-coolant temperature difference). [1]

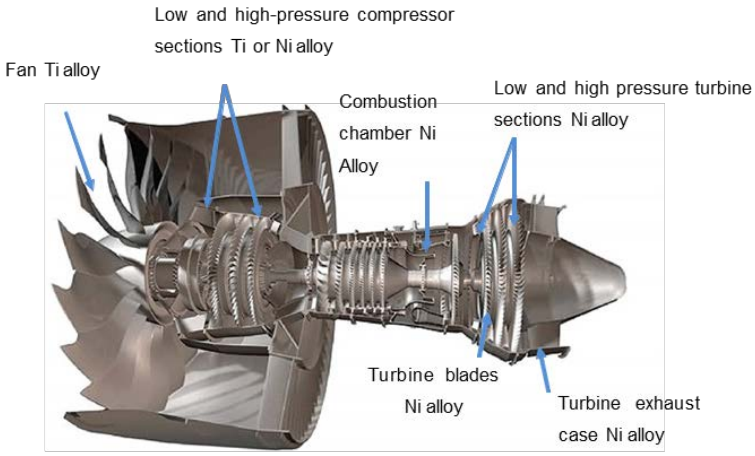

Figure 1-2: Ni-based alloys used on various compartment of a Pratt & Whitney jet engine [2]

Several traditional and non-traditional machining processes used for manufacturing Ni-based alloys from raw materials are summarized by Thakur and Gangopadhyay [3] for different sections of a jet engine as shown in Figure 1-3. While these materials have found extensive use in power generation designs, the low thermal conductivity and high strength make machining them a challenging task. High tool wear rate of Ni-based alloys leads to more frequent change of the cutting tool and therefore decreases the productivity rate, and increases the idle time of the machine.

Traditional Methods	
Type of Method	**Jet Engine Parts**
Drilling	Vanes and Bosses
Turning	Outside Envelope on Disks
Milling	Airfoils
Grinding	Turbine Disks
Broaching	Fir-tree slots of disks
Non-traditional Methods	
Electro-Discharge Machining (EDM)	Bosses and holes
Electro-Chemical Machining (ECM)	Bosses and holes
Laser drilling	Bosses and holes
Wire EDM	Fir-tree slots of disks
Abrasive water jet	Fir-tree slots of disks

Figure 1-3: Machining operation on different parts of a jet engine [3]

A worn-out tool deteriorates the surface finish (see Figure 1-4) and dimensional integrity of the end product in addition to inducing high tensile residual stress on the machined surface, which can accelerate micro-crack nucleation and cause early fatigue failure (see Figure 1-5). Hence, estimating and monitoring the tool wear and its rate, as well as the corresponding effects of wear on a part quality is a critical task.

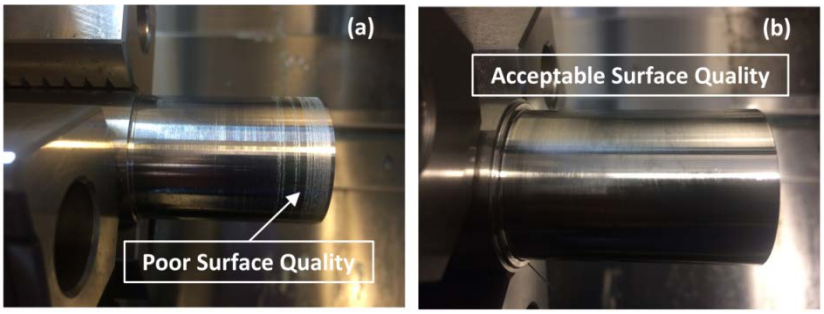

Figure 1-4: Poor quality of machined surface (R_a>1500µm) compared to acceptable surface quality (R_a<800µm) in a typical machining application.

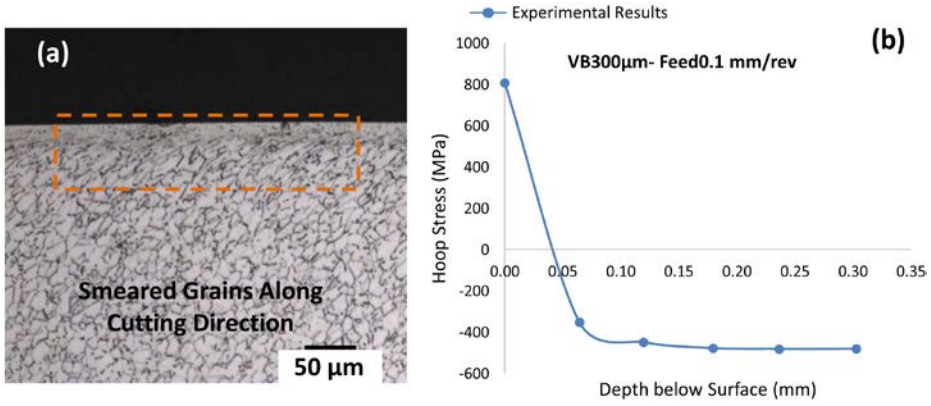

Figure 1-5: Subsurface damage due to tool wear: (a) plastically-deformed grains (work-hardened area) along the cutting direction, and (b) resultant high tensile residual stress (=800MPa) on the surface

Problem Statement

Machining operations can be studied from different aspects. In general, the state of health of machining can be divided into three approaches: (1) health of the tool, (2) health of the workpiece, and (3) health of the machine; these are depicted in Figure 1-6. The state of health for the tool is described as the ability of the tool to properly cut the material. The typical metrics describing it are tool wear, tool wear rate, tool run-out, or a combination of these parameters. The state of health for the workpiece is the ability of the workpiece to meet the quality standards. Quality metrics such as surface roughness, dimensional tolerances and subsurface damage are typical parameters used for describing part quality. Lastly, the state of health of the machine describes the overall performance of the machine in terms of maintenance intervals, average time between failure of components, and prediction of impending faults. As an example, bearing vibration levels over a frequency spectrum, temperature and lubrication state are typical metrics for rotational machinery. Each of these three states of health, individually or together give rise to productivity and profitability of a manufacturing process. Therefore, to maximize the productivity and minimize cost it is important to actively monitor the most influential health factors (tool, part, and machine), and also understand the interactions between them.

Tool wear is known to have significant influence on the machining productivity rate since 20% of the machining downtime is rooted in changing a dull or damaged tool [4].While several models are proposed for describing the progressive wear, all of the existing models are based on simplifying the process, by ignoring or reducing the parameters considered affecting wear generation.

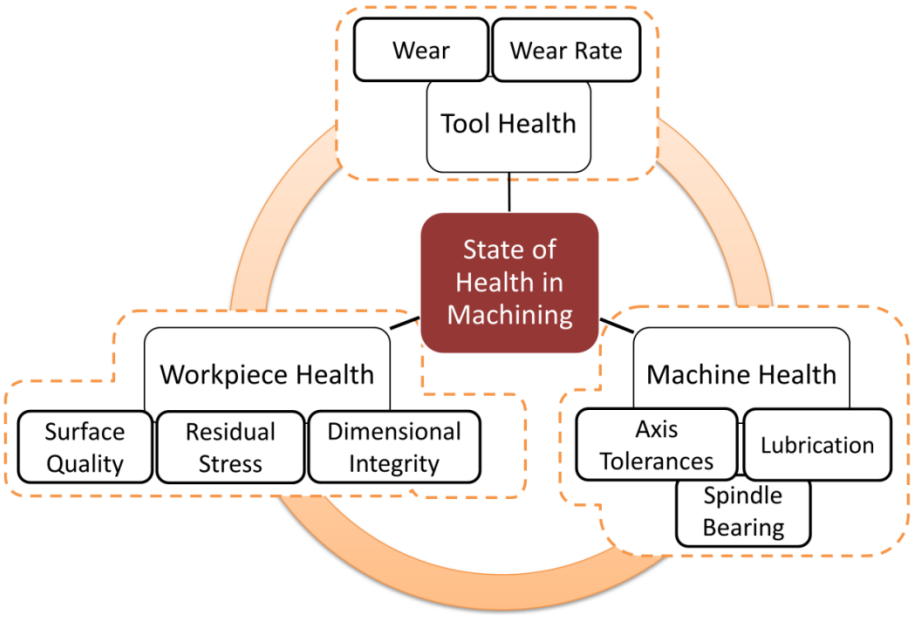

Figure 1-6: State of health in machining operations

The complex dynamics and lack of understanding of the evolution of wear during machining leads to introducing several wear formulations based on different assumptions. Factors such as residual stresses, tool run-out, tolerances, and lubrication can significantly affect the process and makes extending the traditional monitoring models based on deterministic modeling of the tool wear unsuccessful. The high tool wear rate in machining Ni-based alloys also introduces an additional challenge in developing wear models, since fewer experiments are available, and the resultant lack of information affects the accuracy of the model. All of these factors can be categorized as sources of uncertainties in the system, and can be divided into the following:

1. Material: This includes the material properties and material structure. For example, in Ni-based alloys; existence of residual stress beneath the surface, percent concentration of hard carbide or boride particles on grain boundaries, difference in

the weight distribution of elements in the γ' phase in addition to inhomogeneity in material structure, give different machining characteristics to one particular alloy or different alloys.

2. Lubrication: Machining lubrication such as dry cutting, wet cutting with flood coolant, minimum quantity lubrication or cryogenic significantly affect the cutting process and wear behavior.
3. Cutting tool: Ceramic tools or type of tool coating (*e.g.* coated, uncoated tools) in addition to tool geometry (*e.g.* tool nose radius and rake angle) can accelerate or decelerate tool wear rate.
4. Machine dynamics: Design and dynamic stability in terms of machine stiffness can also affect the wear behavior in terms of undesired self-exciting vibrations, such as chatter which shortens the tool life and damages workpiece quality.

Modeling all of these factors is not possible in practice. However, they can be introduced into a modeling framework as uncertainty parameters which change the tool wear as a deterministic state of the operation to probabilistic state and stochastic-based tools must be utilized for tracking the probability distribution of it. The other critical factor that should be studied alongside the wear evolution is the influence of wear on the workpiece quality. In process planning and execution, specific care should be given to avoid any damage to the workpiece due to factors like excessive tool wear. Although significant attention has been given to understand effects of tool coating, geometry, lubrication or cutting conditions on the surface integrity of nickel-based alloys, few literature sources have discussed or considered the role of wear in machining health.

Therefore it is critical to be able to identify and estimate the detrimental effects of wear on the process performance.

Research Questions

In order to fulfill the above research objective, the following research questions will be addressed in this work:

Research Question 1: What is the applicability of Bayesian inference in model parameter calibration when limited experimental data is available? How is the accuracy of such a modeling approach, and how can a probabilistic-based estimation framework be utilized for tracking progressive wear in machining Ni-based alloys?

Research Question 2: What are the parameters representative of surface integrity for Ni-based alloys, and what is the relationship between tool wear, tool wear rate and workpiece quality? Is it possible to use the developed tool condition monitoring methods in RQ1 to preserve a product quality in addition to maximizing tool life?

CHAPTER TWO

2. BACKGROUND

Material Characteristics of Nickel-Based Superalloys

The same reasons making Ni-based superalloys exceptional candidate for high temperature/stress applications, make machining them a challenging task. Ni-based alloys exhibit a unique combination of low-thermal conductivity, high work-hardening, and the ability to preserve ultimate stress at elevated temperatures. Hence, they are categorized as hard-to-machine materials. It is known that the generated temperature at tool-workpiece contacting surface is the main factor affecting the conventional machining operations (*e.g.* milling, turning, drilling, and grinding) [2-3-5]. Therefore, due to the low thermal conductivity of these alloys, heat is accumulated at the tool tip and elevated temperature degrades the coating and damages the tool. Moreover, accumulated heat at the tool-workpiece contacting surface induces a large plastic deformation region in the form of compressive residual stress and work-hardened region beneath the machined surface. Therefore, enormous cutting force is required for cutting the material on the next machining pass. This excessive cutting force can easily damage the tool or cause catastrophic failure in addition to deteriorating the surface integrity and quality of workpiece. The ability of these materials for maintaining their strength at high temperature is attributed to the existence of γ and γ' phase in their microstructure. At the micro level, Ni-based alloys are distinguished with three phases in their microstructure as the following:

1. Gamma (γ) phase: γ phase is a Face Centered Cubic (FCC) matrix of austenite phase that mostly contains elements like nickel, cobalt, chromium, tungsten, and molybdenum [6].

2. Gamma-prime (γ') phase: γ' phase contains the strengthening precipitates that are dispersing in the γ phase. Titanium, Aluminum, and Tantalum are the three major elements that stabilize the γ' phase [7] in the FCC γ phase. The percentage of γ' precipitates and their growth rate are highly dependent on the cooling rate of γ phase [6]. The dispersion of this phase in FCC γ matrix gives an exceptional strength at elevated temperature to these materials. An Image of transmission electron microscopy (TEM) used by Doi *et al.* is shown in Figure 2-1. The cuboidal shapes are the γ' in the direction of γ matrix. The perfect compatibility between the matrix and the precipitate give an exceptional chemical compatibility to the γ' phase. The ductility of the γ' phase provides the strength to the matrix in addition to lowering the fracture toughness [8].

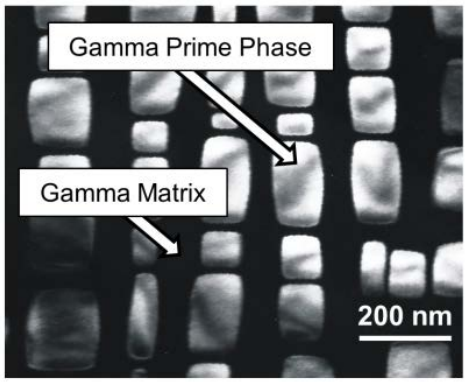

Figure 2-1: Dispersion of cuboidal $\boldsymbol{\gamma'}$ phase in $\boldsymbol{\gamma}$ matrix for Ni-8.5Al-5.4Ti alloy aged at 1213K for 2.7×10^3 seconds [9]

3. Carbide and borides particles: Small quantities (< 0.5%) of elements such as boron and carbon are added to the microstructure to control the grain boundaries and material properties. These carbide and boride particles will reside at the grain boundaries to protect it during wrought processing [6]. According to Bowman, there is no consensus about the carbide particles, whether they are detrimental or beneficial to the superalloys properties. But the in general opinion, the carbide particles help maintain the strength at high temperatures [8]. The alloy elements exist in the Ni-based superalloys structure is shown in Figure 2-2.

Machining Characteristics of Nickel-based Superalloys

As explained in previous section, Ni-based alloys maintain their strength during machining operation. Therefore, high cutting force and cutting power are produced during machining these materials compared to other conventional materials such as Aluminum or Steel. An extensive study in CU-ICAR machining lab was conducted to demonstrate the machinability performance of various difficult-to-machine alloys, which is shown in Figure 2-3.

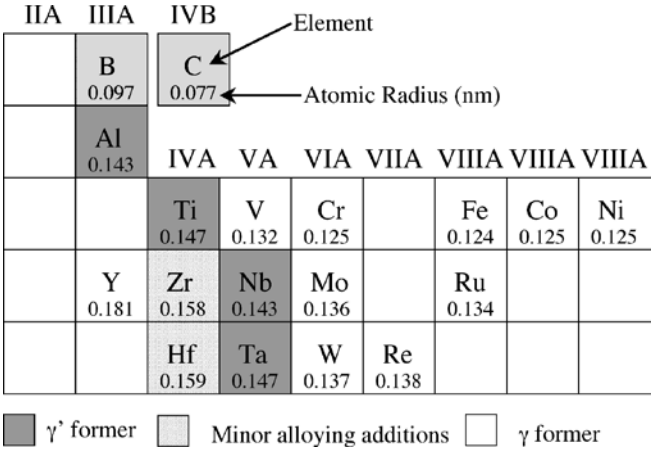

Figure 2-2: General alloy elements exist in Ni-based superalloys [6]

The comparison of cutting force for Ni-based alloys and Stainless Steel is also shown in Figure 2-4. It is clear from Figure 2-4 that cutting γ' strengthened alloys requires significantly higher force than 304-stainless steel.

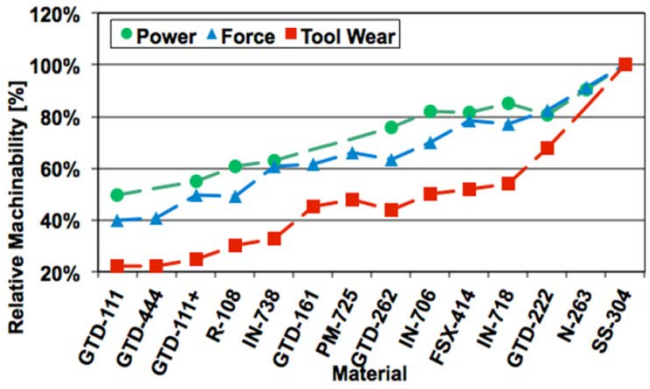

Figure 2-3: Machinability comparison of different Ni-based alloys and stainless steel alloys, the base materials is IN718 [10]

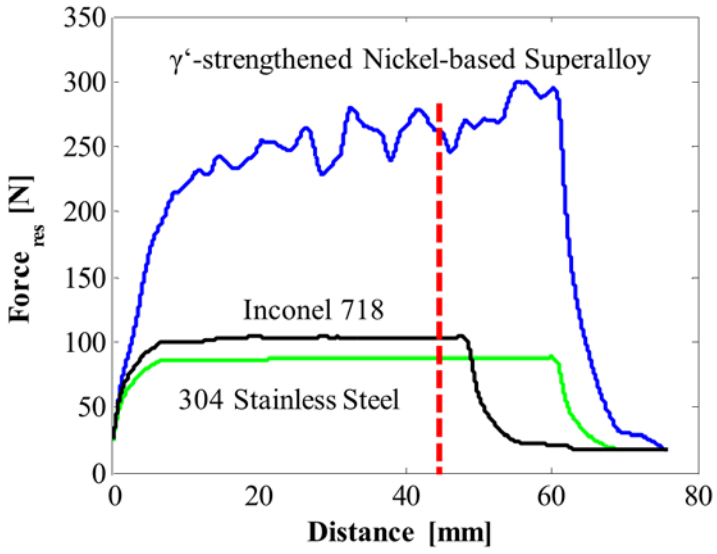

Figure 2-4: Resultant force comparison of Ni-based alloys and 304-stainless steel [11]

Another characteristic of Ni-based alloys are their high tool wear rate. Due to generation of high temperature up to 900-1000^{o}C [12] at the tool tip and low thermal

conductivity, the degradation rate of tool is significantly high. High tool wear rate increases the frequency of tool change, which eventually leads to a higher machine downtime and lower productivity rate. Moreover, excessive tool wear can damage the surface quality and dimensional accuracy of the workpiece and in severe case can damage the machine. Therefore, studying tool wear in Ni-based alloys has significant importance to avoid any catastrophic damage.

The literature existing in the field of tool wear study of Ni-based alloys can be divided into three categories. The first is those works studying the mechanisms of tool wear and parameters affecting them in the micro or macro level. The second category is those works using empirical methods or first principles to model the tool wear in different machining operations and the third category belongs to works that are intending to estimate or predict the tool wear. In the following, each category and their significant findings will be reviewed.

Tool Wear Mechanisms in Machining Ni-based Superalloys

ISO-8688 standard defines the tool wear as a change to the shape of tool during cutting process [13]. This is due to the thermo-mechanical interaction combined with thermochemical reaction of tool and workpiece. There are several wear failure mechanisms observed in research articles in milling, turning and drilling of superalloys with different inserts and cutting conditions. These mechanisms have been reviewed comprehensively by several researchers. According to the state of the art paper of Zhu *et al.* and Akhtar *et al.*, wear failure mechanisms in Ni-based alloys are classified as abrasive, adhesive, diffusion, oxidation (chemical), and debonding failures [14-15].

Existence of each wear failure mechanism is highly dependent on the workpiece material; insert geometry, and cutting conditions. In some cases, the wear progress is only dependent on one particular mechanism, in some other cases multiple wear mechanisms progress together or sometimes tool wear starts with a particular mechanism (abrasive wear) and will be replaced halfway by the nucleation of another mechanisms (adhesion and diffusion) until failure occurs [16]. In the following, each wear mechanism will be discussed briefly.

Abrasive Wear

This type of wear exists in all the machining operations including milling, turning, drilling and grinding. The main cause for abrasive wear is the extreme rubbing and sliding motion of hard particles from the tool into the workpiece or vise-versa. As shown in Figure 2-5. In machining Ni-based alloys, the hard peeled off particles from tool substrate and hard carbide particles in workpiece are responsible for scratching the tool cutting face and cause abrasive wear [15]. A Scanning Electron Microscopy (SEM) of abrasive wear in cutting Inconel 718 (IN718) with ceramic inserts is shown in Figure 2-6. As can be seen in this figure, abrasive wear is identifiable on the cutting (flank) face of ceramic insert as the regions with parallel grooves.

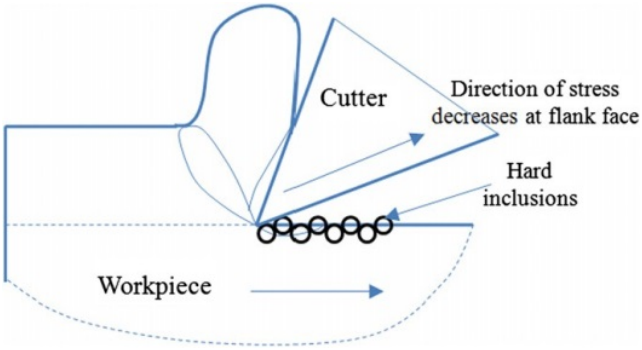

Figure 2-5: Inclusion of hard carbide particles into cutting face of the insert (sliding motion from left to right) [17]

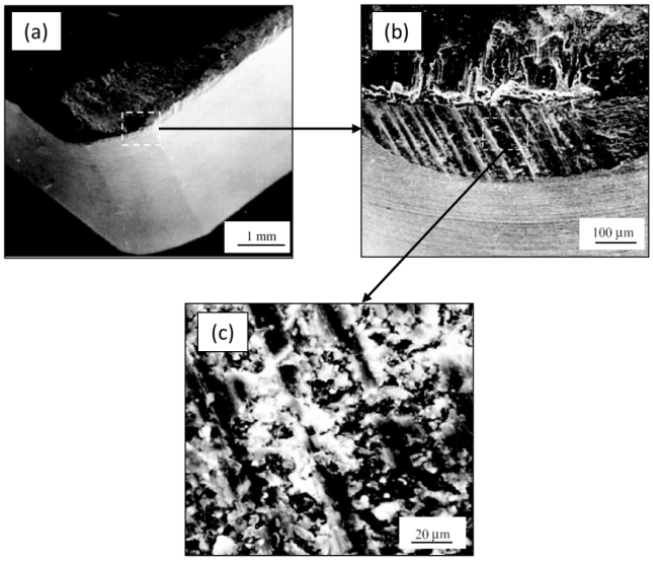

Figure 2-6: SEM micrographs of the wear profile of ceramic coated cutting tool when machining IN718 nickel-based alloys [18]

Adhesive Wear

Adhesive wear or cold welding happens when workpiece material under high temperature and pressure adheres to the rake or flank face of the cutting tool which can be observed in the shape of Build-Up Edge (BUE) or Build-Up Layer (BUL). BUE and BUL eventually peel off from the surface in subsequent cutting passes and cause damage

to the surface quality of workpiece. Moreover, BUE and BUL work as insulation units and prevent heat from dissipating from the tool tip, cause higher temperatures in machining Ni-based alloys and consequently lower tool life. High temperature which constantly exists in cutting superalloys is the main cause of adhesive wear [19-20]. The BUE generated on a coated insert while machining IN718 is shown in Figure 2-7.

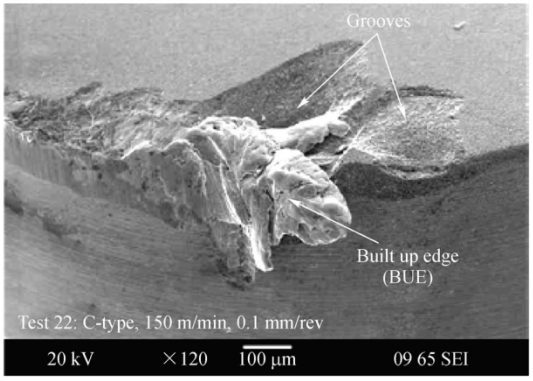

Figure 2-7: BUE generation in worn out insert in high speed cutting of Inconel 718 with coated insert [21]

Diffusion Wear

Diffusion wear occurs in high temperatures at the tool-workpiece and tool-chip interface. Diffusion happens when an element or particle from the tool or the workpiece diffuses into the other. Deng *et al.* found the existence of diffused Ni and Co element into the tool material using ceramic insert [18]. Chen *et al.* observed extensive diffusion wear with TiAlN coated insert when milling IN718 with more than 30 m/min cutting speed [22]. Existence of diffusion wear as the major tool failure mechanism was reported by several researchers in turning, drilling and milling of Ni-based alloys [23-25].

Oxidation and Chemical Wear

Oxidation occurs when the tool substrate is exposed to the air. At very high temperatures, a chemical reaction can happen between surrounding environment (such as oxygen in the air) and the tool elements. As stated by Akhtar *et al.*, although high temperature exists in machining Ni-based superalloys, but this type of wear is less reported in the literature. Since chemical wear can be interpreted as diffusion wear [15].

Debonding Wear

Debonding wear is the most complex type of wear, which is a consequence of accumulation of several types of wear such as abrasive, adhesion, diffusion and oxidation. In this type of wear, pieces of tool are peeled off from the tool surface. Debonding while machining Nickel-based alloys was reported in the work of several researchers as chipping, flaking, notch wear or catastrophic failure [26-29]. Flank wear, chipping, notch wear and flaking are shown in Figure 2-8.

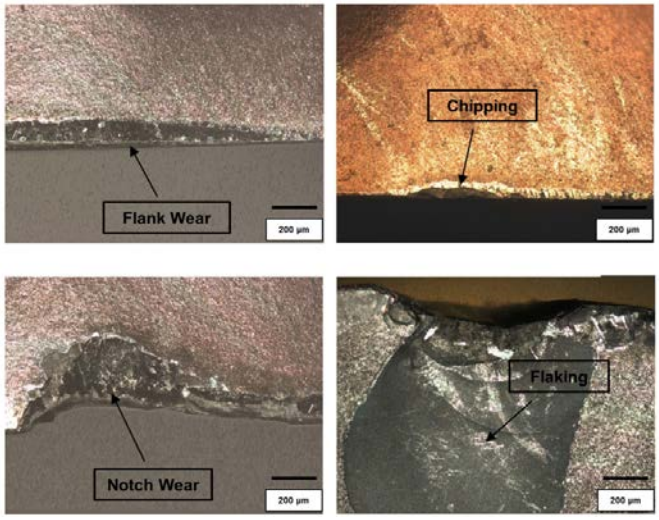

Figure 2-8: Common type of wear in milling IN718. (a) Flank wear, (b) Chipping, (c) Notch wear and (d) Flaking [29]

Tool Wear Maps

Tool wear maps are commonly used for identifying the dominant wear mechanisms in different cutting conditions for optimal cutting selection. Lim carried out an extensive study on designing the wear map for flank and crater faces of the uncoated carbide tools in dry turning. He found an interesting results that even an small change in feed can change the wear rate significantly [30]. The result of his work for High Strength Steel (HSS) uncoated tools is shown in Figure 2-9. Later on, Lim *et al.* found the wear map for TiC coated tools in addition to safety regions for flank wear where tool wear rate are the lowest as shown in Figure 2-10.

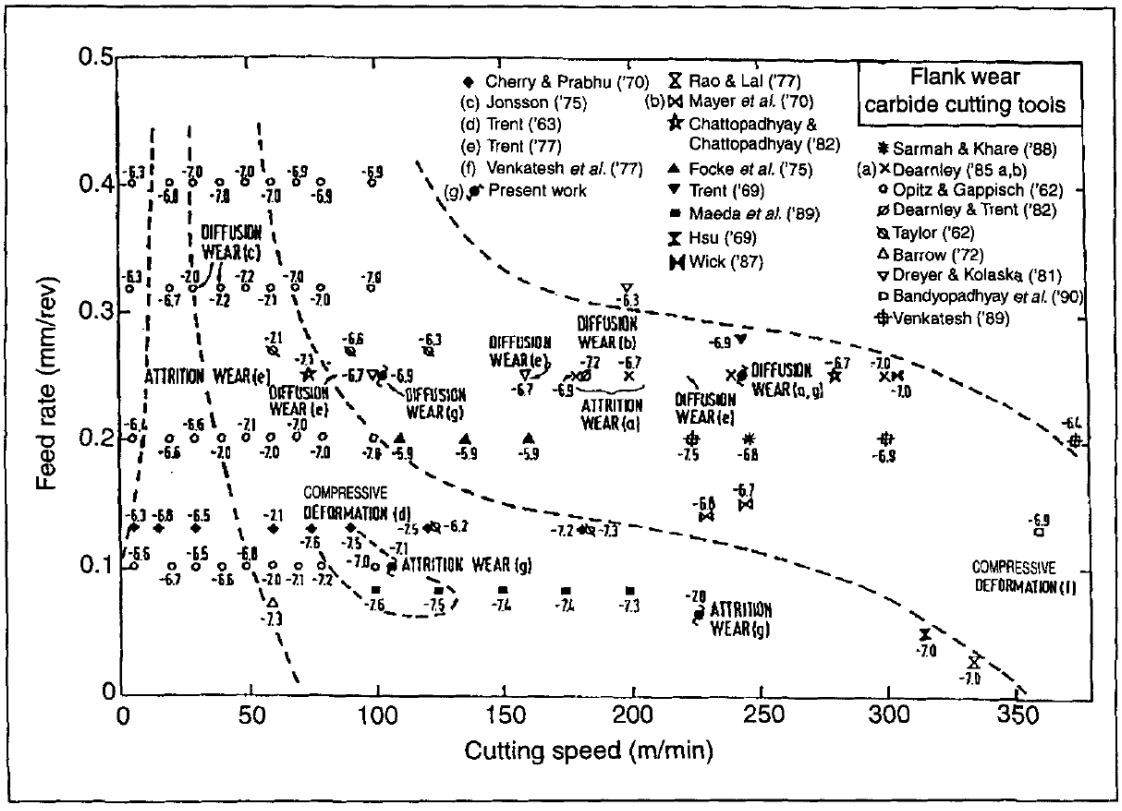

Figure 2-9: Tool wear map on the flank side for carbide cutting tools [30]

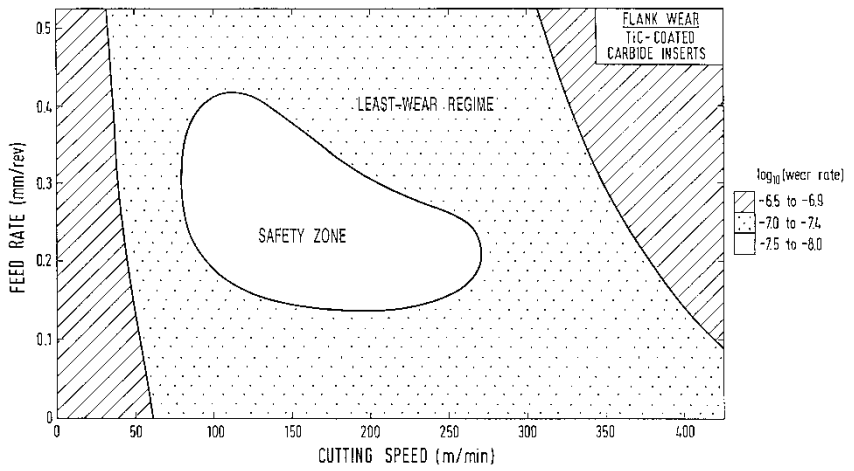

Figure 2-10: Tool wear map for TiC coated inserts in dry turning [31]

Jaffery and Mativenga performed the similar experiments for finding the wear map in P10 carbide insert in dry turning of EN8 Steel [32]. Their result is shown in Figure 2-11. Recently Kuttolamadom [33] studied the wear failure mechanisms of Ti6Al4V in end-milling with WC uncoated insert, however his map (shown in Figure 2-12) was designed based on limited experiments.

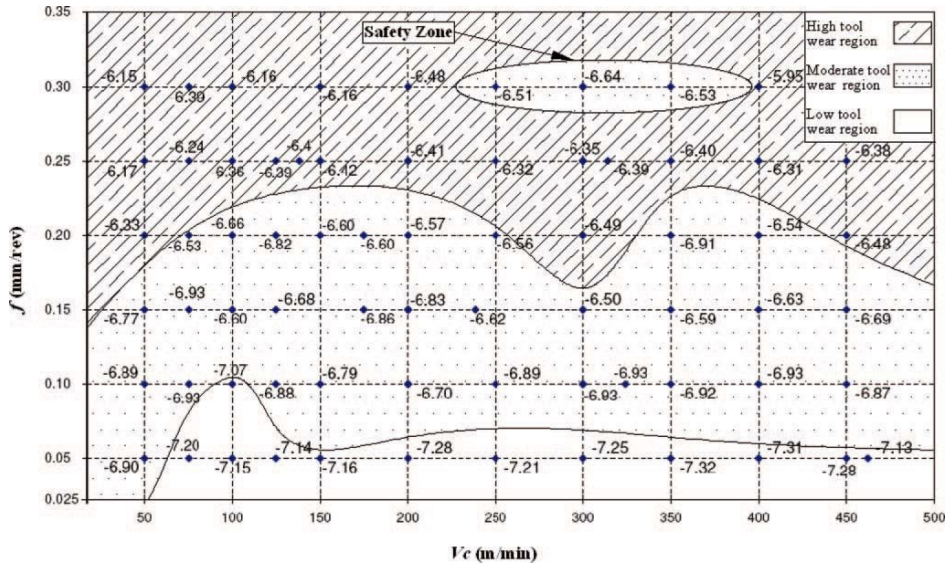

Figure 2-11: Wear map in dry turning of EN8 with P10 carbide tool [32]

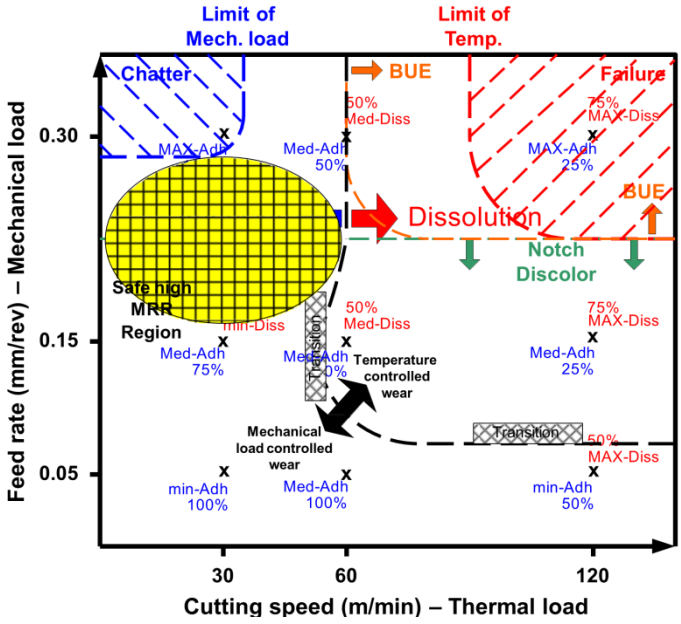

Figure 2-12: Tool wear map in end-milling of Ti6Al4V with WC uncoated insert [33]

Tool Wear Assessment in Nickel-based Superalloys and Measurement Metrics

It is known that tool wear in machining has detrimental effects on the overall performance of the machine. As explained above, BUE or chipping of tool during operation can deteriorate the surface quality or cause abrupt dimensional inaccuracy. Deteriorated surfaces can cause the workpiece to be scrapped at the end of the production line due to quality control metrics. This is a particularly critical consideration when dealing with Ni-based alloys since these materials are expensive. The cost for a bar of 1′ long and 2″ diameter in 2014 of some Ni-based alloys are compared in Figure 2-13 to the other widely used materials in industry, where their cost is about 50 times greater than Aluminum, AISI steel and stainless steel and 2.6 times greater than the cost of Ti-based alloys.

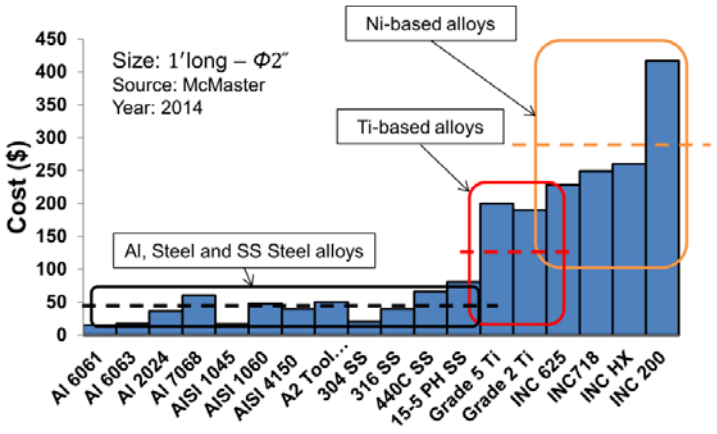

Figure 2-13: Cost comparison of different materials used in industry (source: McMaster-Carr, date accessed: November 2015)

Secondly, the detrimental effect of tool wear induces tensile residual stress at the contacting surface of workpiece. Therefore, a worn out tool increases the likelihood of early failure and reduces the fatigue life. This effect is reported in the literature by many researchers studying the effect of tool condition on residual stress [34-36]. The change in magnitude of tensile residual stress at the surface of machined IN718 for sharp and worn inserts are selected from the work of Sharman *et al.* [34] and is shown in Figure 2-14.

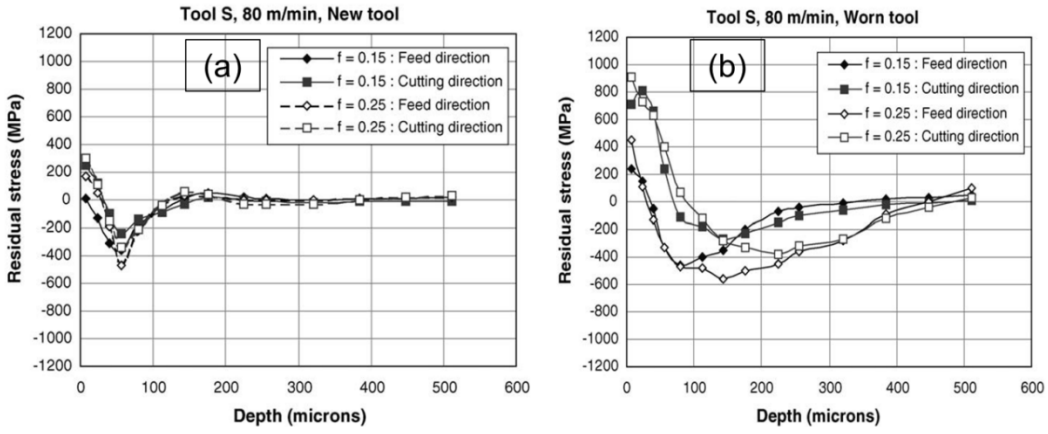

Figure 2-14: Surface and subsurface residual stress in turning IN718 with coated insert. (a) Sharp insert (b) Worn-out insert [34]

Third, the detrimental effect of a worn tool is the tearing, generation of micro-cracks and inclusion of carbide particles on the surface of workpiece which is shown in Figure 2-15. This inclusions and micro-cracks reduce the fatigue life and cause early failures in the operation.

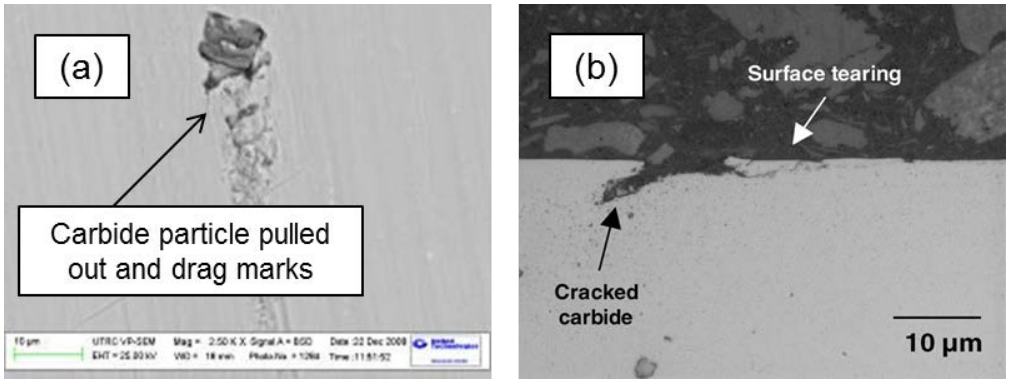

Figure 2-15: Surface damage due to worn tool in turning IN718. (a) Dragged carbide particle on the surface of workpiece [37] (b) Tearing and cracking of the surface [34]

The importance of tool wear in manufacturing Ni-based alloys emerges when all the above effects are taken into consideration. Particularly by considering the major application of Ni-based alloys, which is in sensitive industries like aerospace and power generation, where any unpredicted failure can lead to millions of dollars damage.

Tool wear is conventionally measured on two surfaces, *i.e.* flank face and rake face. The flank face is in direct contact with the surface of workpiece and directly influences the surface quality of workpiece. The wear area on the flank face, which is called flank wear and its average width, is considered as the primary measure of flank wear. According to ISO-8688 standard, a tool with maximum of 300µm flank wear is considered “worn-out.” On the other hand, the rake face is in contact with the chip flow of material and usually the depth of crater generated by sliding the chip on the rake face

is measured as crater wear. Flank and rake faces with their wear area are shown in Figure 2-16. Chipping, notch wear and flaking are another types of wear which are already shown in Figure 2-8.

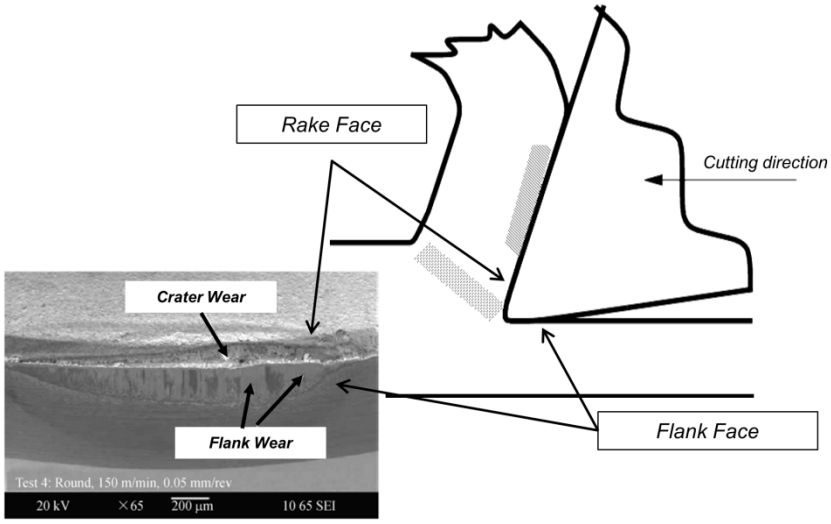

Figure 2-16: Flank and rake face with corresponding flank and crater wear

Tool Condition Monitoring

In automated manufacturing systems, accurate estimation and monitoring of important process states (*e.g.* tool wear) is a critical factor to reduce downtime, avoid catastrophic failure, and preserve the quality of the final product. In Ni-based materials, the wear rate of inserts during machining is relatively high compared to conventional materials [14]. Such a high tool wear rate while machining makes establishing an accurate tool wear model a challenging task because only a limited number of experiments can be completed before tool failure.

Tool wear studies can be divided into two major categories: the first is the empirical or semi-empirical study based on the observed relationships of cutting conditions such as feed and cutting speed to tool wear. Taylor tool life model is the most commonly used

empirical model developed and still widely in use in the machining industry [38]. While convenient to use, Taylor tool life model is blind to the tool wear mechanisms and cannot be used for modern machining such as high speed machining [39]. The second category is model-based studies that use pre-developed mechanistic models for certain mechanisms of tool wear. Such studies include the Takeyama and Murata model of tool flank wear that considers mechanical abrasion and physicochemical type of wear [40], the Usui model of crater wear that uses a 3-dimensional heat transfer model of the chip to derive the wear characteristic Equation assuming only the diffusion mechanism exists [19], the Koren model where only abrasion and diffusion mechanisms were considered for wear model development [41], and the Rabinowicz model where only the abrasive mechanism was investigated for modeling tool wear [42]. Numerical studies are a subcategory of mechanistic methods that are based on finite element analysis (FEA) of mechanical interactions between the tool and the workpiece material [39-43]. While FEA is accurate in modeling tool wear, the major drawback is its time inefficiency which makes it impractical for industrial use. One of the subcategories of empirical models are data-driven methods. As implied from its name, these methods rely on input data and its correlation to tool wear. The advantages of data-driven techniques are mostly realized in situations where the process model is not available. This feature is particularly useful for studying tool wear in machining Ni-based materials due to the lack of mechanistic models.

To use data-driven methods, three main decisions need to be made: The type of signal to use, the features of the signal to extract, and the method to select. Force data is the

most widely used measurement signal in tool wear studies. Despite being precise, the measurement device (*i.e.* dynamometer) needs continuous calibration [44], limits the workpiece size [45], and is expensive, making it almost impossible to implement in industrial machine shops. Vibration and Acoustic Emission (AE) signals have shown good capability in studying tool wear; however, the mounting location of the AE sensor or the accelerometer has significant influence on their performance [44-46]. On the other hand, Hall effect sensors used for power sensing are relatively inexpensive, they can be easily mounted in the machine, and they do not limit the size of the workpiece, which make them suitable candidates for machining performance assessment in industrial applications. However, the power signal, which is representative of the resultant force, is not always as sensitive to the tool condition as cutting force [47]. Due to the differences in the nature of sensors, each can capture different information from the system. Thus, by using sensor fusion methods, it is possible to extract more informative information from the signals. Wang *et al.* fused two sensors for flank wear estimation of ASSAB718 steel in dry milling, namely a vision system (direct measurement) and a force sensor (indirect measurement) [48]. Their results were promising for flank wear estimation. However, their method was only applicable for dry milling. The flow of coolant in machining titanium and nickel-based materials makes using the vision measurement systems almost impossible. Segreto *et al.* combined force, AE and vibration sensors for tool wear classification of Inconel 718 with a backpropagation neural network in wet machining [46-49]. They could achieve a success rate of 98% for discrimination between a sharp and worn insert. They also reported small contribution of the vibration sensor due to the

environmental noise in machining. While the use of classifiers, make combining the effect of multiple tool wear mechanisms possible, the output is less informative than estimators since no information will be provided on the evolution of particular tool wear mechanisms. Similar work on tool wear classification of AISI4340 steel was conducted by Cho *et al.* [50]. They compared the performance of different classifiers, multilayer perception neural network, radial basis function neural network, support vector machine, and machine learning ensemble, in fusing 4 different sensors (Force, Vibration, AE and Power) with 11 different combinations [50]. According to their results, machine learning ensemble had the highest accuracy with 97% success rate with the combination of vibration and force sensors. Vibration and power sensors, which are well suited for industrial applications, were fused in the work of Trejo-Hernandez *et al.*. They created a FPGA (Field Programmable Gate Array) smart sensor for predicting tool wear area in turning of AISI 1045 and showed, by fusion of the aforementioned sensors, that estimation results improved 3 times as compared with a single sensor [51]. In the recent work of Zhang *et al.*, AE and cutting sound (microphone) sensors were utilized in turning superalloy GH2135 for flank wear estimation with support vector regression for predicting tool wear and support vector machine for classifying the tool state [52]. Based on their results the prediction accuracy of fused sensors is very close to the prediction result of a single AE sensor, which makes using sound sensors a redundant choice [52]. Moreover, linear behavior was observed in their result, which enables using simpler methods such as linear regression and time series modeling.

In addition to available data driven tools, several works in the literature studied feature selection techniques. The features of the acquired signal related to tool wear are categorized as time domain, frequency domain, and time-frequency domain features. Scheffer *et al.* used correlation and the statistical overlap factor of statistical features of force signals in the time domain, and showed that the standard deviation of the force signal is the most sensitive feature in turning to tool wear [53]. In another effort, Segreto *et al.* used time domain features of AE, vibration, and force signals in addition to principal component analysis and linear predictive analysis for tool wear classification of Inconel 718 in turning [46-49]. Fang *et al.* studied the frequency domain features of the fast Fourier transform of the vibration signal for tool edge wear assessment of Inconel 718 [54]. Time-frequency decomposition of the signal using wavelet transforms has been considered by different researchers. As mentioned by Xiaoli, a successful feature selection method should be as sensitive as possible to tool wear and insensitive to changes in cutting conditions and other external factors [44]. Xiaoli used Continuous Wavelet Transform (CWT) for decomposing AC motor current and Discrete Wavelet Transform (DWT) for decomposing AC servomotor current for small drill bit breakage detection [44]. Choi *et al.* studied the relationship between Root Mean Square (RMS) of Discrete Wavelet Transform of a force signal in ramp cuts of AISI 1018, and showed that the RMS value of the wavelet coefficient exhibits a linear relationship to tool wear in different cutting conditions [55]. However, they proposed a separate model for each cutting condition and could not develop a generalized tool wear model. Chuangwen and Hualing used the Wavelet Packet Decomposition (WPD) of the vibration signal and

introduced a new feature selection procedure for eliminating the effect of cutting conditions [56]. In another effort, Jemielniak *et al.* introduced two new correlation coefficients for selecting the statistical features of wavelet coefficients of WPD for rough turning of Inconel 625 [57]. The variability of different feature selection methods is shown in Table 2.1. The focus of the majority of literature in the field of Tool Condition Monitoring (TCM) is on conventionally available material such as steel. Recently the attention is shifted toward nickel-based alloys, but mainly on classification purposes, which does not provide information on tool wear evolution.

One of the challenges in tool wear monitoring is the complexity of its dynamics, and quantifying the effect of various variables such as tool coating, tool geometry, material structure, lubrication, tool run-out and initial residual stresses. Since controlling all these parameters is impossible, they act as the sources of uncertainties in machining. Therefore a stochastic-based method can be used for analyzing the state of the tool. One of the early works in this field is the work of Schmitz *et al.* on stochastic estimation based on mesh grid method for identification of unknown parameters in 2-D Merchant model [58].

Table 2.1: Selected sensors and features for TCM

Authors	Signal	Method	Feature	Material
[59]	AE	WPD	Root Mean Square	40Cr Steel
[60]		DWT	Energy of wavelet coefficient	AISI 6150
[61]		WPD	Peak to valley / Crest factor / Mean / Variance / Kurtosis	AISI 45
[56]	Vibration	WPD	Normalized energy	-
[62]		Time Domain	Mean / Variance / Skewness / Kurtosis	-
[63]		Time Domain /	Root Mean Square	AISI 45

		WPD		
[64]		DWT	Mean / Variance of local maxima	ASSAB 760
[55]		DWT	RMS	AISI 1018
[65]	Force	Time Domain	Variance / Energy around certain frequency	Aluminum alloy
[53]		Time Domain – Frequency Domain	Variance / Energy around certain frequency	Aluminum alloy
[66]		SOM	Average / Variance over one revolution	ASSAB 718HH
[48]		WPD	Energy of signal	ASSAB 718HH
[45]	Current	DWT	Low frequency in wavelet coefficients	AISI 1018
[67]		WPD	Mean	Mild steel
[68]	Image (Vision)	WPD	Energy	25Cr3Mo3NiNb
[54]	Force / Vibration	WPD	Root Mean Square	Inconel 718
[57]	Force / AE	WPD	Root Mean Square / log- energy / Skewness / Kurtosis / Ring down counts / pulse width	Inconel 625
[46]	Force / AE / Vibration	Time Domain	Coefficients of Principal Component Analysis	Inconel 718
[49]		Time Domain	Linear predictive analysis	Inconel 718
[44]	Motor/Axis Current	CWT / DWT	-	AISI 45 quench steel

The identified parameters were fed into the model for predicting cutting force and its uncertainty and experimentally validated on turning AISI-1045 steel [58]. In another effort by Karandikar *et al.*, the authors used the mesh grid method and Markov Chain Monte Carlo (Metropolis algorithm) for Bayesian parameter inference on Taylor tool life and extended Taylor life in milling of AISI-4137 steel. They compared the results with deterministic approach (maximum likelihood estimation) and showed that by using the

Bayesian method and combining the prior knowledge to the likelihood function, fewer experiments were required for parameter inference [69-70]. An alternative stochastic approach for tool wear studies is based on reliability and injury theory. Salonitis and Kolios investigated the applicability of using Monte Carlo simulation and first order reliability method for characterizing the probability of tool failure in different feed and cutting speed [71]. In an interesting research by Braglia and Catellano and Braglia *et al.*, they derived the distribution of the tool life based on progressive behavior of the tool wear with diffusion theory and Fokker-Plank equation. They calculated the average and the uncertainty of progressive tool wear which were in agreement with experimental results [72-73]. While diffusion theory is successful in tracking progressive tool wear, it cannot be used for chipping or breakage detection; this will limit the applicability of their method.

Concluding Remarks

In this chapter, material characteristics of nickel-based alloys, wear failure mechanism, its effect on surface integrity in addition to existing Tool Condition Monitoring (TCM) methods were reviewed. By looking at the state-of-the-art literatures reviewing tool wear mechanisms and surface integrity of Ni-based alloys [2-3-5-14-15], the existing research gap in selecting the proper signal, proper feature and proper TCM method is still observable. In over 300 papers reviewed by the recently-published superalloy machining state-of-the-art paper of Thakur and Gangopadhyay, none was about monitoring methods. The extensive literature review shows that, the total number of research articles about TCM specifically used for Ni-based are not more than 25

journal articles or conference proceedings. Moreover, while the effect of cutting conditions, tool coating or lubrication on surface integrity of nickel-based alloys have been widely studied, the tool wear effects as one of the most important features in machining superalloys has not been taken into consideration yet. Therefore, a secondary research gap in connecting the tooling health to the health of the end-product still exists.

CHAPTER THREE

3. BAYESIAN INFERENCE FOR POWER-MODEL PARAMETER CALIBRATION

Several models have been proposed to describe the relationship between cutting parameters and machining outputs such as cutting forces and tool wear. However, these models usually cannot be generalized, due to the inherent uncertainties that exist in the process. These uncertainties may originate from machining, workpiece material composition, and measurements, and are particularly significant in Ni-based alloys. A stochastic approach should be utilized to compensate for the lack of certainty in machining, particularly for rapid tool wear evolution leading into a small dataset. The Markov Chain Monte Carlo (MCMC) method is a powerful tool for addressing uncertainties in machining parameter estimation. The Hybrid Metropolis-Gibbs algorithm has been chosen estimate the unknown parameters in a mechanistic tool wear model for end milling of a Ni-based alloy and its performance is compared with the deterministic approach.

Theoretical Background

Bayes Rule

Bayesian data analysis is a powerful tool used for statistical inference. Thomas Bayes introduced the Bayesian inference and proposed the basic formulation, known as the Bayes rule, in the 18^{th} century [74]. According to the Bayes rule, the probability of an event θ, is derived by multiplying initial belief or previous knowledge to the likelihood

function $p(y|\theta)$ as in Equation 3-1. Where $p(\theta|y)$ is a posterior probability of event θ, $p(\theta)$ is the initial belief and $p(y)$ is a marginal distribution.

$$p(\theta \mid y) = \frac{p(y \mid \theta)p(\theta)}{p(y)},\ p(y) = \int p(y \mid \theta)p(\theta)d\theta \qquad 3\text{-}1$$

Assuming independent and identically distributed (i.i.d.) observations, the likelihood function, $p(y|\theta)$, is simplified as the product of each observation probability as in Equation 3-2. In many cases, finding a closed form solution for marginal distribution is somewhat tedious or even impossible [75], so it is convenient to treat *p(y)* as a normalizing and simplify Equation 3-1 to Equation 3-3. Although finding the closed form solution of posterior probability distribution -$p(\theta|y)$- in some cases is possible, in many cases numerical approximations such as Markov Chain Monte Carlo (MCMC) methods like Gibbs sampler or Random-Walk Metropolis algorithm are proposed to generate samples from the posterior probability instead of calculating it.

$$p(Y \mid \theta) = P(y_1, ..., y_2 \mid \theta) = \prod_{i=1}^{n} p(y_i \mid \theta) \qquad 3\text{-}2$$

$$p(\theta \mid Y) \propto p(Y \mid \theta)p(\theta) \qquad 3\text{-}3$$

Gibbs Sampler

The Gibbs sampler is proposed as one of the Markov Chain Monte Carlo methods to sample from a posterior distribution when a closed from solution of posterior probability distribution is not available [76]. To implement the Gibbs sampler, the closed form solution for the full conditional probability distribution of each parameter given all the remaining parameters is required. To illustrate how Gibbs sampler works, one needs to

consider a linear regression model as in Equation 3-4. Where $Y\epsilon\{y_1,\ldots,y_n\}$ is the set of observations, β_i is an unknown coefficient, $X=[x_1,\ldots,x_i]^T$ is a set of known variables and ε is a measurement error, which is assumed to be normally distributed with zero mean and unknown variance σ^2. In this case, there are two unknown values - β_i and σ^2 - that should be identified within Bayesian framework.

$$Y = \beta_i^T X + \varepsilon \tag{3-4}$$

Joint posterior probability density of the unknowns can be written as Equation 3-5. The term $p(\beta_i|\sigma^2, x_i, y_1,\ldots,y_n)$ is called the full conditional of β_i, and the term $p(\sigma^2|x_i, y_1,\ldots,y_n)$ is called the marginal distribution of σ^2 where calculating its closed form solution is tedious except with some special assumptions. However, the Gibbs sampler states that if the full conditional of unknown parameters β_i and σ^2 are known, samples taken from them belong to the their joint posterior distribution. Full conditional of β_i can be written as Equation 3-6, where $p(\beta_i)$ is an initial belief with mean β_0 and variance Σ_0.

$$p(\beta_i, \sigma^2 \mid X, y_1,\ldots y_n) \propto p(\beta_i \mid \sigma^2, X, y_1,\ldots y_n)\, p(\sigma^2 \mid X, y_1,\ldots y_n) \tag{3-5}$$

$$\begin{aligned} p(\beta_i \mid \sigma^2, X, y_1,\ldots y_n) &\propto p(y_1,\ldots y_n \mid \beta_i, \sigma^2, X)\, p(\beta_i \mid \sigma^2, X) \\ &= p(y_1,\ldots y_n \mid \beta_i, \sigma^2, X)\, p(\beta_i) \end{aligned} \tag{3-6}$$

Assuming i.i.d. observations and after some simplifications, full conditional of β_i is derived as a Normal distribution with the mean β_n and the covariance Σ_n as in Equations 3-7 to 3-9.

$$p(\beta_i \mid \sigma^2, X, y_1,\ldots y_n) \propto N(\beta_n, \Sigma_n) \tag{3-7}$$

$$\beta_n = (\sum_0^{-1} + \frac{\mathrm{X}^T\mathrm{X}}{\sigma^2})^{-1}(\sum_0^{-1}\beta_0 + \frac{\mathrm{X}^T\mathrm{Y}}{\sigma^2}) \quad 3\text{-}8$$

$$\sum_n = (\sum_0^{-1} + \frac{\mathrm{X}^T\mathrm{X}}{\sigma^2})^{-1} \quad 3\text{-}9$$

The next is finding the full conditional of σ^2. This can be written as Equation 3-10, where $p(\sigma^2)$ is the initial belief of measurement variance. It has been shown by Hoff, that this distribution can be considered as an inverse-gamma distribution (see Equation 3-11) with v_0 and σ_0^2 as a sample size and sample variance respectively [75].

$$\begin{aligned} &p(\sigma^2 \mid \beta_i, X, y_1, \ldots y_n) \propto p(y_1, \ldots y_n \mid \beta_i, \sigma^2, X)\, p(\sigma^2 \mid \beta_i, X) \\ &= p(y_1, \ldots y_n \mid \beta_i, \sigma^2, X)\, p(\sigma^2) \end{aligned} \quad 3\text{-}10$$

$$p(\sigma^2) \propto IG(\frac{v_0}{2}, \frac{v_0\sigma_0^2}{2}) \quad 3\text{-}11$$

By plugging in Equation 3-11into the Equation 3-10, the full conditional of measurement error variance is calculated as shown in Equation 3-12, where *SSE* is a sum of squared errors equivalent to $\sum_{i=1}^{n}(Y_i - \beta^T X)^2$ and n is a number of observations. Therefore, the full conditional probability distribution of unknown parameters in linear systems is available and the Gibbs sampler can be easily used to draw samples to characterize the posterior distribution. This algorithm is described in Figure 3-1.

$$\begin{aligned} &p(\sigma^2 \mid \theta, y_1, \ldots y_n) \propto \left((\sigma^2)^{\frac{n}{2}} \exp\left\{ -\sigma^2 \sum_{i=1}^{n} (y_i - \theta)^2 / 2 \right\} \right) \times \left((\sigma^2)^{\frac{v_0}{2-1}} \exp\{-\sigma^2 v_0 \sigma_0^2 / 2\} \right) \\ &= (\sigma^2)^{\frac{v_0+n}{2-1}} \times \exp\left\{ -\sigma^2 \times \left[v_0\sigma_0^2 + \sum (y_i - \theta)^2 \right] / 2 \right\} = IG(\frac{v_0 + n}{2}, \frac{v_0\sigma_0^2 + SSE}{2}) \end{aligned} \quad 3\text{-}12$$

- (0) Find the full conditional of unknowns
- (1) start with k=1
  - Draw a sample β_i^k from full conditional of β_i:

$$\beta_i^k \sim N(\beta_n, \Sigma_n)$$

- (2) Use the drawn sample β_i^k
  - Calculate sum of squared error:

$$- SSE = \sum_{i=1}^{n} \left(Y_i - \beta_i^{k^T} X_i\right)^2$$

  - Draw a sample σ_k^2 from the full conditional of σ^2:

$$- \sigma_k^2 \sim IG\left(\frac{v_0+n}{2}, \frac{v_0\sigma_0^2+SSE}{2}\right)$$

- (3) ADD (+1) to k and GO to line (1)

Figure 3-1: Gibbs sampler algorithm

Random-Walk Metropolis Algorithm

The Gibbs sampler is an easy to implement and practical method in the case of linear models, while it does not work for nonlinear models or in cases where closed form solution of the full conditional distributions of unknown parameters are not available. Another technique proposed by Metropolis *et al.*, where a distribution called proposal density is used to approximate the posterior distribution of parameters [77]. Since the proposal density does not fully capture the features of the posterior distribution, an acceptance-rejection method should be implemented to reject the samples that are generated from the regions with lower probability. Unlike the Gibbs sampler that accepts all the samples, the Metropolis algorithm accepts a portion of them. The step-by-step guide for the Metropolis algorithm is shown in Figure 3-2.

- (0) Select the proposal density function
- (1) Select the starting point as β_i^1 , σ_1^2
- (2) FOR k=1:N
  - Select a candidate point q_k from proposal density:
    $$q_k \sim N(0, \delta^2)$$
  - Calculate a candidate point β_i^*:
    $$\beta_i^* = \beta_i^k + q_k$$
- (3) Calculate the r ratio
$$r = \frac{p(\beta_i^* | \sigma^2, X, y_1, \dots, y_n)}{p(\beta_i^k | \sigma^2, X, y_1, \dots, y_n)}$$
$$= \exp\{\frac{-1}{2}[\frac{SSE(\beta_i^*) - SSE(\beta_i^k)}{\sigma_k^2} + N(\beta_0, \Sigma_0)|_{\beta_i^*} - N(\beta_0, \Sigma_0)|_{\beta_i^k}]\}$$
- (4) Select a point U from the uniform distribution
$$U \sim uniform[0,1]$$
- (5) Find the acceptance ratio
$$\alpha = \min\{1, r\}$$
- (6) IF $U<\alpha$
  - Accept the candidate point: $\beta_i^{k+1} = \beta_i^*$
- OTHERWISE
  - Reject the candidate point: $\beta_i^{k+1} = \beta_i^k$
- (8) END IF
- (9) END FOR

Figure 3-2: Metropolis algorithm

In practical applications, a symmetric probability density (*i.e.* a Normal distribution with zero mean and arbitrary variance δ^2) is used as the proposal density function. Lynch 2007 reported that finding the variance δ^2 is more of an art than science and it depends on the experience level of the user [78]. Therefore, several studies exist about techniques for finding an optimal proposal density variance [79-81]. The proper choice of the proposal density function, plays a critical role in the acceptance rate of candidate points. If a very small variance is chosen for δ^2, it takes a long time for the Markov-chain to converge to the true values and if a very large variance is chosen the rejection rate of drawn samples increases and this affects the efficiency of the chain. It is reported that the 25-35% acceptance rate can be considered as appropriate for the convergence of Markov chain

[75]. In this work, a method used by Solonen 2006 based on calculating the Jacobian matrix was used to find with the proposal density variance [82]. It is worth mentioning that in addition to Metropolis algorithm, there are many other algorithms developed such as Metropolis–Hasting algorithm, Delayed Rejection algorithm, and Adaptive Metropolis to increase the performance of sampling procedure [75-81-83]. The last part of this section explains the Solonen method to approximate the proposal density variance (δ^2). Solonen showed that an optimal value of the covariance matrix δ^2 can be approximated as Equation 3-13, where *MSSE* is the minimum sum of squared error derived after plugging in the optimal value of β_i that minimizes squared error function and *J* is a Jacobian matrix of outputs with respect to the unknowns as in Equation 3-14.

$$\delta^2 = (J^T J)^{-1} MSSE \tag{3-13}$$

$$J = \left[\frac{\partial Y}{\partial \beta_1^{opt}} \quad \dots \quad \frac{\partial Y}{\partial \beta_i^{opt}} \right] \tag{3-14}$$

Mechanistic Tool Wear Model

The tangential force in milling is proportional to the chip area as in Equation 3-15, where K_s is an unknown cutting pressure and *A* denotes chip area. There have been several attempts in the literature to find a closed-form solution for the cutting pressure. Koenigsberger and Sabberwal proposed that the cutting pressure is a function of average chip thickness [84], which was later confirmed by the other authors [85-89]. Therefore, assuming the cutting pressure is dependent on the average chip thickness ($\overline{h}$), Equation 3-15 can be written as Equation 3-17. Where K_s' and *c* are constants, a_p is the

depth of cut, f is the feed, m is the number of cutting tooth and φ is the instantaneous angle of rotation (see Figure 3-3).

$$F = K_s A_s \tag{3-15}$$

$$K_s = K_s' \bar{h}^c \tag{3-16}$$

$$F = K_s A_s = K_s a_p h \rightarrow F = K_s' \bar{h}^c a_p \frac{f}{m} \sin\varphi \tag{3-17}$$

$$F_t = K' \bar{h}^c a_p f \sin\varphi \tag{3-18}$$

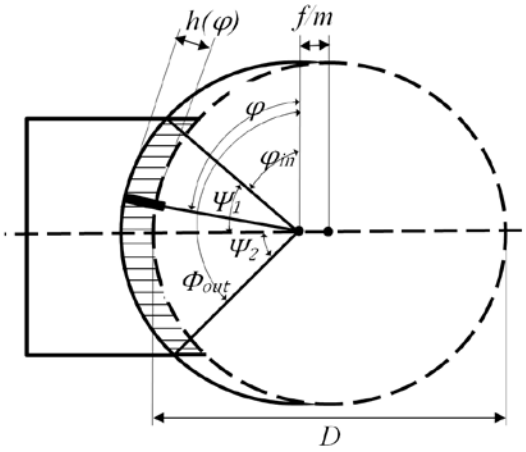

Figure 3-3: Milling Schematic [90]

The mean chip thickness $\bar{h}$ can be found in terms of the entrance and exit immersion angles (ψ_1 and ψ_2, respectively) as shown in Equation 3-19. Assuming the geometrical relationship as Equation 3-20, the relationship between average chip thickness and feed is derived in Equation 3-21. In conventional milling tests demonstrated in Figure 3-3, these two angles are constant. Thus, the Equation 3-19 reduces to Equation 3-22 with constant C_1.

$$\bar{h} = \frac{1}{\varphi_{out} - \varphi_{in}} \int_{\varphi_{in}}^{\varphi_{out}} h(\varphi) = \frac{1}{m} \frac{1}{\varphi_{out} - \varphi_{in}} \int_{\varphi_{in}}^{\varphi_{out}} f \sin(\varphi) d\varphi$$
$$= \frac{1}{m} \frac{1}{\varphi_{out} - \varphi_{in}} f[\cos(\varphi_{out}) - \cos(\varphi_{in})] \quad 3\text{-}19$$

$$\varphi_{in} = 90 - \psi_1, \ \varphi_{out} = 90 + \psi_2 \quad 3\text{-}20$$

$$\bar{h} = \frac{1}{m} \frac{1}{\psi_1 + \psi_2} f[\cos(90 + \psi_2) - \cos(90 - \psi_1)] = \frac{1}{m} \frac{1}{\psi_1 + \psi_2} f(\sin\psi_1 + \sin\psi_2) \quad 3\text{-}21$$

$$\bar{h} = C_1 f \quad 3\text{-}22$$

It was shown with an increase in the tool wear, the magnitude of the cutting force increases as well [91]. Rubenstein showed that the change in magnitude of tangential force F_t is a function of the material hardness H_h, friction coefficient μ, tool flank wear VB and tool wear length s represented by Equation 3-23, where s is assumed to be equal to the depth of cut a_p [92-93]. All the parameters in Equation 3-23 can be assumed constant in milling except for VB, which changes relative to the volume of removed material in the process. By adding Equation 3-23 to Equation 3-18, the resultant tangential force can be written as Equation 3-24, where C_2 is a constant summarizing the constant variables.

$$F_t^{wear} = \mu VBH_h s \quad 3\text{-}23$$

$$F_t = K'C_1 f^{c+1} a_p \sin\varphi + C_2 VB \quad 3\text{-}24$$

Waldorf *et al.* 1992 showed that the constant K' is dependent on cutting conditions including feed, and depth of cut [93] as in Equation 3-25, where C_3 is a constant, and α_1-α_2 denotes the feed and depth of cut exponents. Plugging Equation 3-25 into

Equation 3-24, the tangential force is derived as a function of cutting conditions. Multiplying the tangential force F_t with the cutter diameter D and spindle speed N yields to instantaneous cutting power P as in Equation 3-27. The average power can be simply determined by integrating Equation 3-27 from the entering angle to the exiting angle as in Equation 3-28, where K_1 to K_3 are unknown parameters that need to be identified.

$$K' = C_3 f^{\alpha_1} a_p^{\alpha_2} \quad 3\text{-}25$$

$$F_t = C_1 C_3 f^{c+\alpha_1+1} a_p^{\alpha_2+1} \sin\varphi + C_2 VB \quad 3\text{-}26$$

$$P = C_1 C_3 D f^{c+\alpha_1+1} N a_p^{\alpha_2+1} \sin\varphi + C_2 DNVB \quad 3\text{-}27$$

$$P = K_1 N f^{K_2} + K_3 NVB \quad 3\text{-}28$$

Milling Experimental Setup

Material used for this experimental study is a Ni-based superalloy known as Rene-108 (R-108). An OKUMA GENOS M460-VE 3-axis CNC machine was used to end-mill (in down-milling direction) rectangular blocks of size 60 mm× 80 mm× 25 mm, using a water-soluble coolant with 8% concentration. A 2-flute indexable tool holder with a diameter of 15.875 mm was used, and the width of cut was chosen to be 9.5 mm that corresponds to 60% tool engagement, as this was the maximum manufacturer recommendation for the particular tool holder. Full length of the blocks (60 mm) was utilized for machining. At the chosen width of cut, 8 tests were conducted on the block: 4 tests with 2 replications. 4 additional tests were also conducted to cover the full range of cutting conditions for validating the results. Depth of cut for each pass is kept constant at 0.5 mm, and cutting speed and feed were changed as excitation factors for parameter

identification. Tool Monitoring Adaptive Controller (TMAC) installed on the machine was used for measuring spindle current to monitor spindle power consumption in real time. However, due to the low sampling frequency of commercial software (~50 Hz), an external data acquisition device (DAQ) was programmed to capture the data with high sampling rate. To measure spindle power in high sampling frequency, the output of the transducer (Figure 3-4) was fed into a NI9215 analog input module mounted on NI-cRIO9103 chassis programmed with LabVIEW2010. Data was collected in voltage at sampling rate of 10.24 kHz.

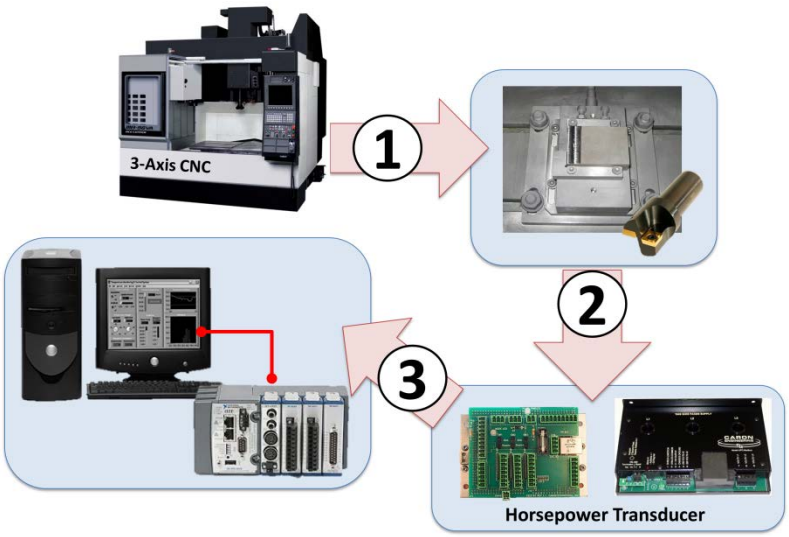

Figure 3-4: Data Acquisition with NI-cRIO9103

Tests for the R-108 were designed in a fashion that the effect of each parameter can be observed, therefore selecting a high and a low level of cutting speed and feed. Two levels of cutting speed at 25 and 50 m/min, two levels of feed at 0.1 and 0.2 mm/rev, and a constant depth of cut of 0.5 mm were used to identify the constants K_1, K_2 and K_3 in Equation 3-28. These cutting parameters were selected at both their relatively mild values

to show the behavior of the inserts under normal machining conditions, and at their relatively aggressive values to show the behavior of the inserts under high material removal rate condition. Cutting parameters for validation tests were selected between the mild and aggressive values. Design of Experiment (DoE) used in this work is shown in Table 3.1. Spindle power consumption was measured for each pass. The change in spindle power consumption is shown in Figure 3-5, where the increase in the power illustrates the developing flank wear during the cutting process. The mean value of cutting power between 42-48 mm cutting distances (70-80% of total cutting distance) was selected as the average cutting power affected by the tool flank wear at each test. One portion of this value is contributed to the power required to cut the workpiece (*i.e.* $K_1 N f^{K_2}$), and another portion is due to the effect of the tool wear on increasing cutting power magnitude (*i.e.* $K_3 NVB$).

Inserts used in this work were Sandvik Coromill (R390-11 T3 08M-PM 1030) coated insert. The 1030 grade is recommended by Sandvik for milling R-108 due to its resistance to material build-up on the cutting edge and plastic deformation [94]. The shape of the insert and the tool holder is shown in Figure 3-6 and Figure 3-7 with their corresponding dimensions in Table 3.2 and Table 3.3. Fresh unworn inserts were used for each test, and the flank wear on the bottom edge of each insert was measured using an Olympus optical microscope and average flank wear was calculated. Measured tool flank wear for tests 1-4 is shown in Figure 3-8.

Table 3.1: DoE table for end-milling R-108 Ni-based superalloy

Test [#]	V_c [m/min]	f [mm/rev]	P [$\times 10^{-3}$ hp]	VB [µm]
1	25	0.1	36	88
2	25	0.2	57	73
3	50	0.1	82	85
4	50	0.2	154	113
5	25	0.1	36	88
6	25	0.2	47	82
7	50	0.1	62	97
8	50	0.2	165	82

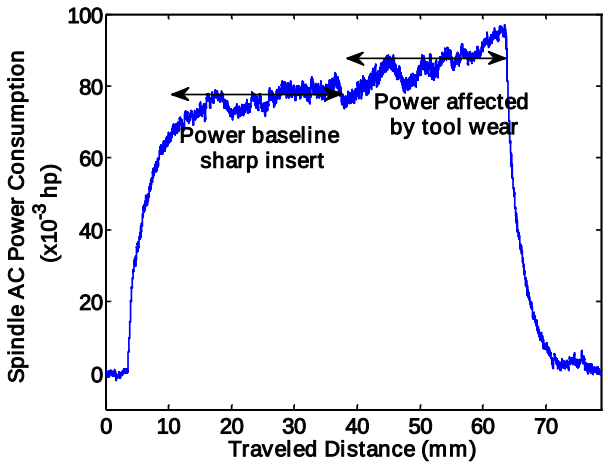

Figure 3-5: Cutting power of test 3, V_c=50 m/min, f=0.1 mm/rev

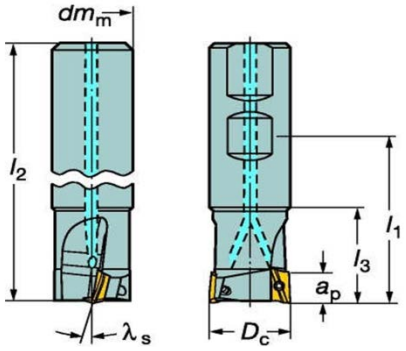

Figure 3-6: Tool holder shape[94]

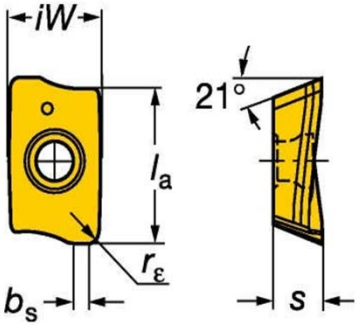

Figure 3-7: Sandvik-1030 insert shape [94]

Table 4 - 1: Dimension of the tool holder in end-milling operation [94]

Parameter	Value
D_C [mm]	15.875
dm_m [mm]	19
l_1 [mm]	56.8
l_2 [mm]	82.6
l_3 [mm]	25.9
a_p [mm]	10
λ_S [°]	13.43

Table 3.2: Dimensions of the insert in end-milling operation [94]

Parameter	Value
l_a [mm]	11
iW [mm]	6.8
s [mm]	3.59
b_S [mm]	1.2
r_ε [mm]	0.8

To shed a light on tool failure mechanisms in end-milling of Rene-108, Scanning Electron Microscopy (SEM) along with x-ray elemental analysis were used to study the flank side of the insert in different cutting conditions. As shown in Figure 3-8(a), the elemental analysis showed an extensive amount of elemental nickel on the flank face of the insert in the mildest feed and cutting speed, which represents adhesion wear in the cutting process. Parallel grooves on the flank face were also observed, which represent abrasion wear. With an increase in feed, initial chipping of coating was observed in Figure 3-8(b). High content of elemental tungsten which is the base material for the insert revealed the coating was damaged during the cutting process. Considering Figure 3-8(c), where only cutting speed is increased showed a larger chipped off area from the flank

face; therefore it can be concluded that cutting speed has more influence on exciting the chipping mechanism in the process. In the most aggressive cutting condition, where both feed and cutting speed increased together, extensive chipping was observed. The SEM image in Figure 3-8(d) demonstrates a completely failed insert in these cutting conditions. The existence of each wear failure mode is summarized graphically in Table 3.4. It is clear that chipping starts in the first pass except for the mildest conditions. Chipping has detrimental effect on the insert health and can be detected from the power signal as a sudden drop in the signal.

Table 3.3: Contribution of tool failure mechanisms to the flank wear

Test [#]	Feed [mm/rev]	Cutting speed [m/min]	Tool wear mechanisms Blue: Abrasion Green: Diffusion Red: Chipping
1	0.1	25	
2	0.2	25	
3	0.1	50	
4	0.2	50	

Bayesian Inference on Model Parameters

The objective of this section is to identify unknown parameters K_1, K_2 and K_3 and measurement error variance σ^2 when limited number of experiments exist. Due to the nonlinearity of Equation 3-28, finding the full conditional distribution of the unknown parameters is not possible but the full conditional of measurement error variance (σ^2) is available as in Equation 3-12. It is possible to use a Hybrid Gibbs-Metropolis algorithm to characterize the posterior distribution of the unknowns. In such case, the Metropolis

algorithm is used to generate samples from the unknown distribution of parameters K_1, K_2 and K_3 and the Gibbs sampler is used to characterize the distribution of the measurement error variance σ^2. In Figure 3-9, the flow chart of the combined algorithm is shown. Since the full conditional of σ^2 is available, all the samples drawn with using the Gibbs method were accepted automatically, but a rejection-acceptance method should be implemented for the samples generated by the Metropolis algorithm.

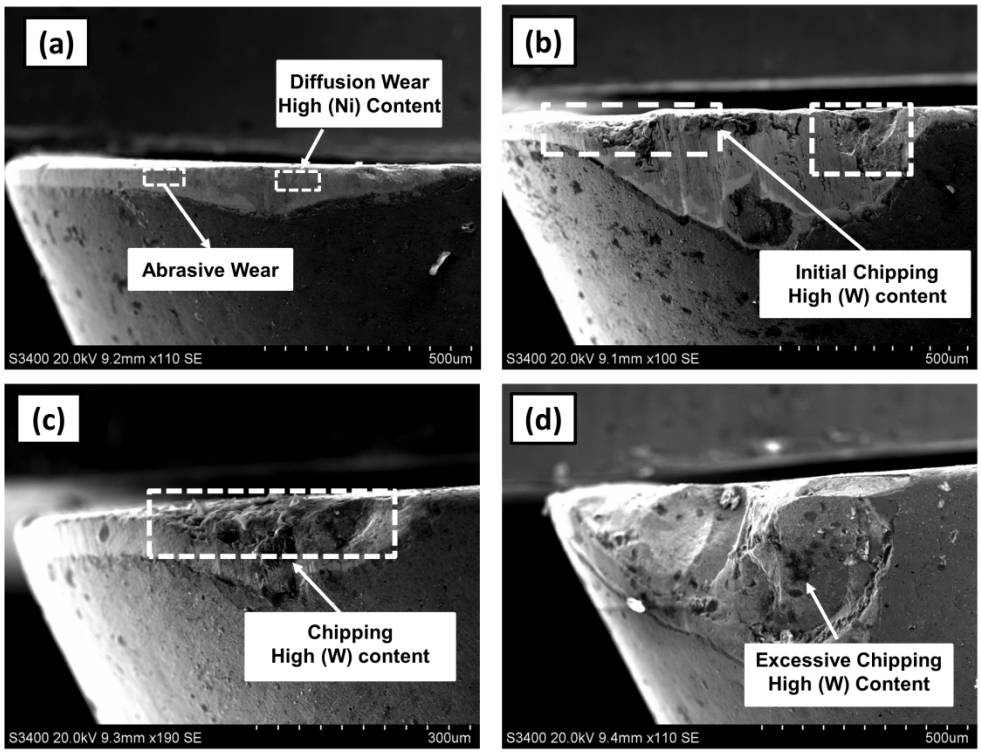

Figure 3-8: SEM image for (a) feed of 0.1 mm/rev and cutting speed of 25 mm/min, (b) feed of 0.2 mm/rev and cutting speed of 25 mm/min, (c) feed of 0.1 mm/rev and cutting speed of 50 mm/min and (d) feed of 0.2 mm/rev and cutting speed of 50 mm/min

The prior belief for unknown parameters is chosen as normal distribution with the mean of 1 and a large variance (Equation 3-29). The prior belief for measurement covariance is chosen as inverse gamma function with v_0=1 and σ_0^2=100 (Equation 3-30).

$$\begin{bmatrix} K_1 \\ K_2 \\ K_3 \end{bmatrix} \sim \left(\begin{bmatrix} 1 \\ 1 \\ 1 \end{bmatrix}, \begin{bmatrix} 1 & 0 & 0 \\ 0 & 1 & 0 \\ 0 & 0 & 1 \end{bmatrix} \right) \quad \text{3-29}$$

$$\sigma^2 \sim IG\left(\frac{1}{2}, \frac{2}{100^2}\right) \quad \text{3-30}$$

To avoid singularity of the covariance matrix, spindle power consumption is multiplied by 1000 so that K_1 and K_3 are in the same range as K_2. The rest of this study is based on the normalized value for K_1 and K_3. The optimal value of unknown parameters (Equation 3-31) was calculated from the data in Table 3.1 using unconstrained derivative free optimization method. This method uses simplex search algorithm described by [95]. At each iteration, new points are generated around the simplex, and the points with the lowest output function are rejected. The process is repeated until the optimal points that minimize the output function are found. Since this searching algorithm relies on minimizing the squared error of the measurement and the model output (*i.e.* maximizing the likelihood of the model output given the measurements), it is classified as a regression based method in classical Frequentist view.

$$K_i : \arg\max\left[K_1 N f^{K_2} + K_3 NVB \right] \rightarrow \left[K_1 \quad K_2 \quad K_3 \right]^T_{\text{Freq.}} = \left[0.94 \quad 1.21 \quad 0.15 \right]^T \quad \text{3-31}$$

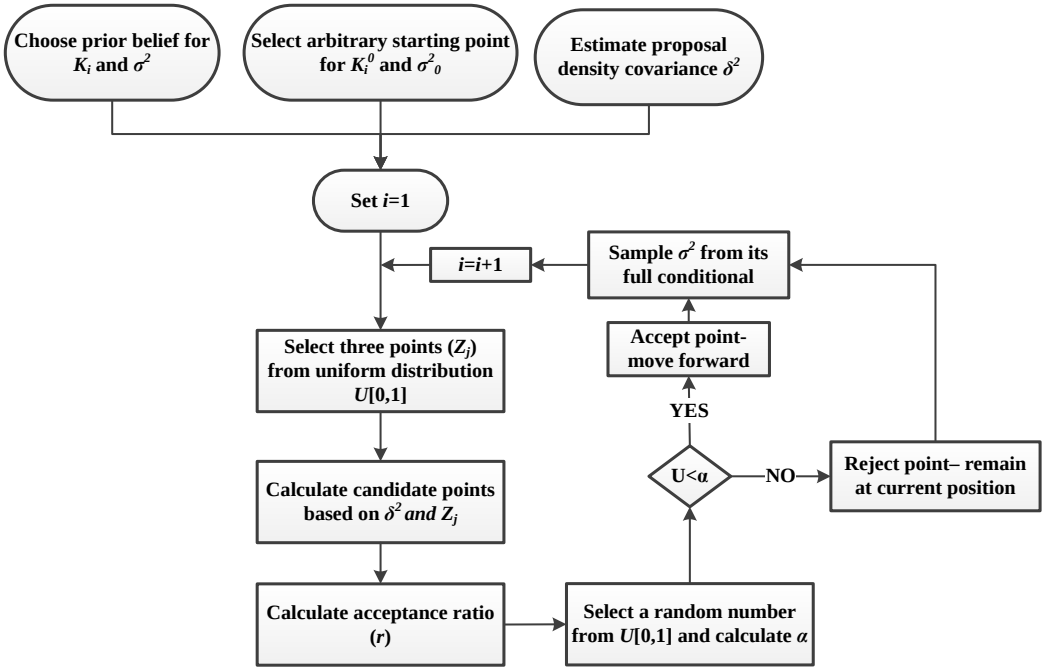

Figure 3-9: Flowchart of hybrid Metropolis-Gibbs algorithm

The Jacobian matrix shown in Equation 3-32 was calculated using K^{opt} from simplex search (Equation 3-31) for each test the Solonen formula [82] was used for finding the proposal density covariance matrix which is shown in Equation 3-33. The optimal points K^{opt} were used for initializing the Markov-chain. The total number of points in the chain was selected as N=2000.

$$J = \begin{bmatrix} N_1 f_1^{K_2^{opt}} & K_1 N_1 f_1^{K_2^{opt}} \log(K_2^{opt}) & N_1 V B_1 \\ \dots & \dots & \dots \\ N_8 f_8^{K_2^{opt}} & K_1 N_8 f_8^{K_2^{opt}} \log(K_2^{opt}) & N_8 V B_8 \end{bmatrix}_{8\times 3} \quad 3\text{-}32$$

$$\delta^2 = \begin{bmatrix} 0.87 & 0.78 & 0.51 \\ 0.78 & 0.74 & 0.52 \\ 0.51 & 0.52 & 0.41 \end{bmatrix} \quad 3\text{-}33$$

Results and Discussion

MCMC trace plot for the parameters K_1, K_2 and K_3 following the procedure described in previous section with N=2000 points is shown in Figure 3-10(a). The first set of iterations are usually discarded (burn-in period) to reduce the effect of initial errors at the start of the chain [75]. In this work, the first 20% of the iterations (400 points) were discarded as the burn-in period. After removing the first 400 points, the acceptance ratio was calculated as 19%. To assess the convergence of the Markov-chain, autocorrelation plot of samples shown in Figure 3-10(b) should be taken into consideration. In a converged chain, samples become uncorrelated to each other after some time. However, as it is shown in Figure 3-10(b) samples are heavily correlated which indicates that the Markov-chain was not able to converge to the posterior density. According to Hoff to improve the performance of Markov-chain, the posterior variance of samples can be an efficient choice of proposal variance [75]. Therefore, to improve the current run (named as "Pilot run" from now), the information from the generated samples was used as the initial belief of parameters for a next MCMC run (named as "Main Run"). The mean and covariance matrices of the Pilot Run were extracted from the chain and implemented as a prior belief. The covariance matrix of parameters was also used as the proposal density covariance ($=\delta^2$), and the final point of the chain was used as the initial point of the new chain. For the Main Run, number of generated samples was selected as N=10,000.

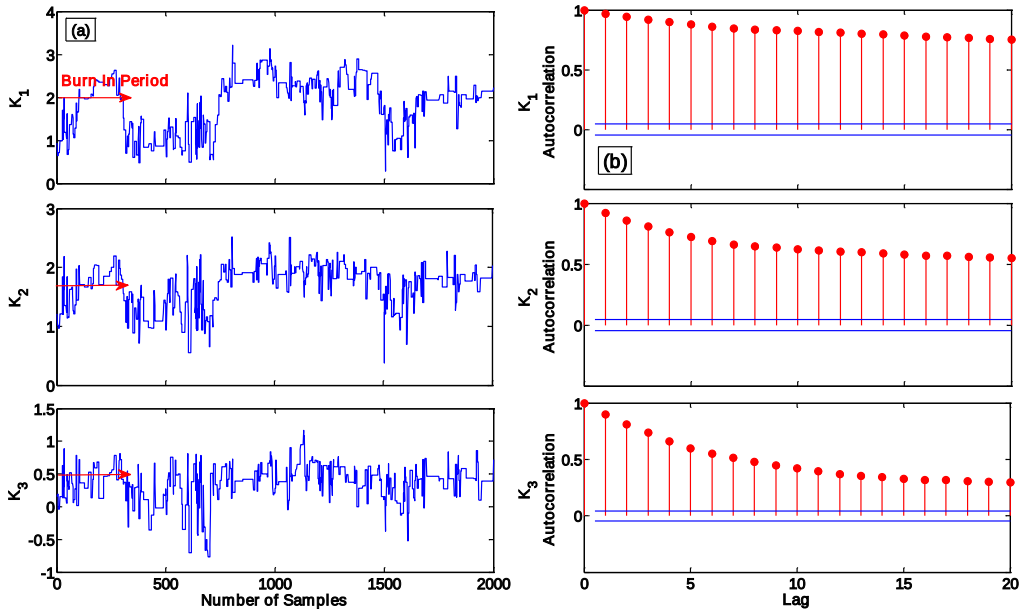

Figure 3-10: Pilot run samples (a) Trace plot (b) Samples Autocorrelation (Diverged Chain)

The trace plot and the autocorrelation plot of samples are shown in Figure 3-11. After modifying the proposal density variance and the initial prior the chain has converged and parameters are mixing well. After removing the first 20% of the samples (2,000 points) as the burn-in period, a comparison of each pair of parameters distribution is shown in Figure 3-12, where contour (a) is the initial belief (prior distribution) from the Pilot Run, and contour (b) to (d) is the posterior belief of parameters. The multivariate posterior distribution of identified parameters is shown in Equation 3-33. Figure 3-13 also demonstrates the improvement in the degree of uncertainties after each MCMC run. Analysis starts with an initial degree of uncertainties which is collected from previous available data or a rational guess. The initial belief as shown in Figure 3-13 covers a wide range of possible values for unknown parameters (*i.e.* large variance, shown as dashed red curve), however by running the MCMC method and bringing new information, the

range of possible values for unknown parameters shrinks and at the same time its probability distribution moves toward the true values of actual parameters (shown as solid blue and dashed black curves).

$$\begin{bmatrix} K_1 \\ K_2 \\ K_3 \end{bmatrix} \sim N\left(\begin{bmatrix} 1.94 \\ 1.79 \\ 0.43 \end{bmatrix}, \begin{bmatrix} 0.20 & 0.07 & 0.01 \\ 0.07 & 0.04 & 0.02 \\ 0.01 & 0.02 & 0.02 \end{bmatrix} \right) \qquad 3\text{-}34$$

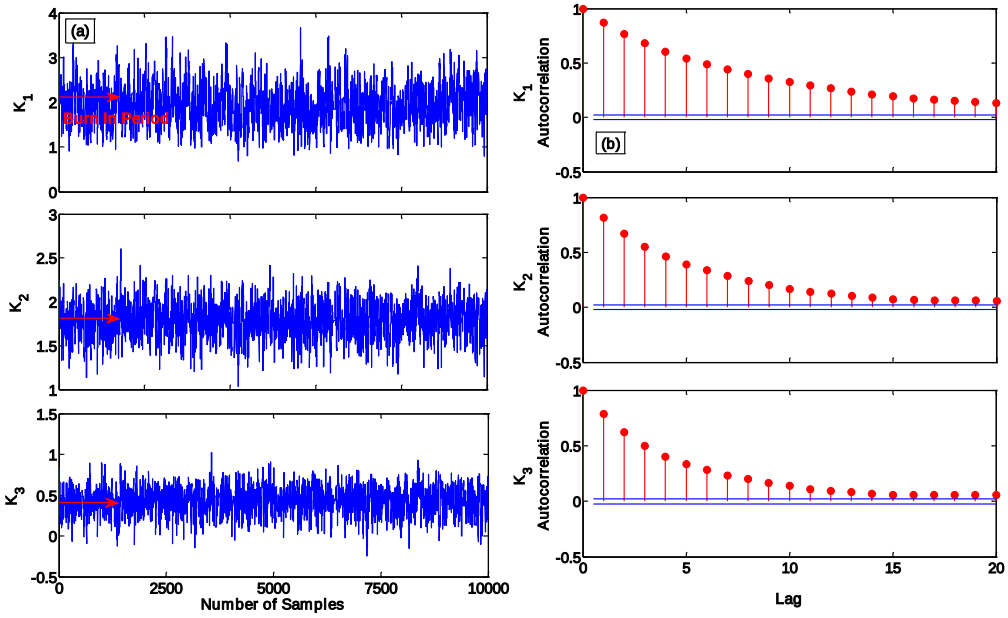

Figure 3-11: Main run samples (a) Trace plot (b) Samples Autocorrelation (Converged Chain)

Furthermore, gamma distribution of the inverse of measurement error variance ($1/\sigma^2$) generated from the Gibbs sampler is shown in Figure 3-14. The mode is chosen as the posterior value of the measurement error variance σ_N^2=51. Now that the unknown parameters distribution are identified, the performance of the Bayesian inference can be evaluated using the validation tests. Table 3.4 shows the cutting parameters, spindle power consumption, and tool flank wear for each of the 4 new tests. It is fairly

straightforward to find the posterior distribution of observations (posterior predictive distribution) as shown in Figure 3-15.

The expectation is that the measured power be within the 95% confidence interval for each of the 4 tests. As shown in Figure 3-16, the model is able to predict the measured power with good accuracy. Percent error between the measurement and the prediction mean for each test is compared in Table 3.5. Maximum 18% error indicates that the algorithm is capable to predict spindle power consumptions with good degree of accuracy, which implies validity of identified parameters. As demonstrated in Figure 3-16, at test 4 some of samples of the posterior predictive distribution are generated in the negative area which is physically impossible. The nature of a large variance in power prediction in test 4 is due to the limited number of available experiments for establishing the model. Limited experiments cause a significantly large measurement error variance which produces a large variation in the output of the model. However, considering the mean of output prediction in comparison to the measured power, the error is in acceptable range (only 5% in test 4).

The performance of Bayesian and Frequentist (deterministic) views in terms of percentage error in estimating spindle power are compared in Figure 3-17. While there is no significant difference observed in the identification sets, the Bayesian inference showed a better performance in the validation tests (more than 50% reduction of error in validation tests 2 and 4). The performance of the model based on these two views and the advantageous of Bayesian inference will be further investigated in Chapter 44.

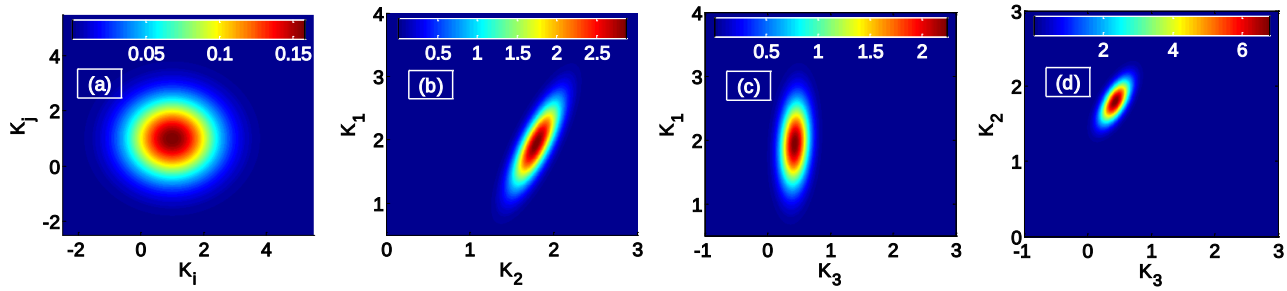

Figure 3-12: Prior and posterior distributions after main run, (a) prior probability of K_i and K_j, (b) posterior probability of K_1 and K_2, (c) posterior probability of K_3 and K_1 and (d) posterior probability of K_3 and K_2

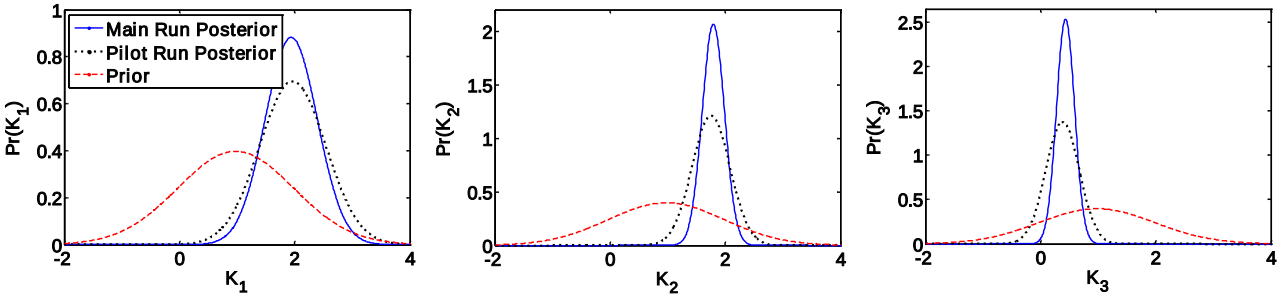

Figure 3-13: Distribution of parameters for prior belief, pilot run, and main run (the y-axis is not normalized)

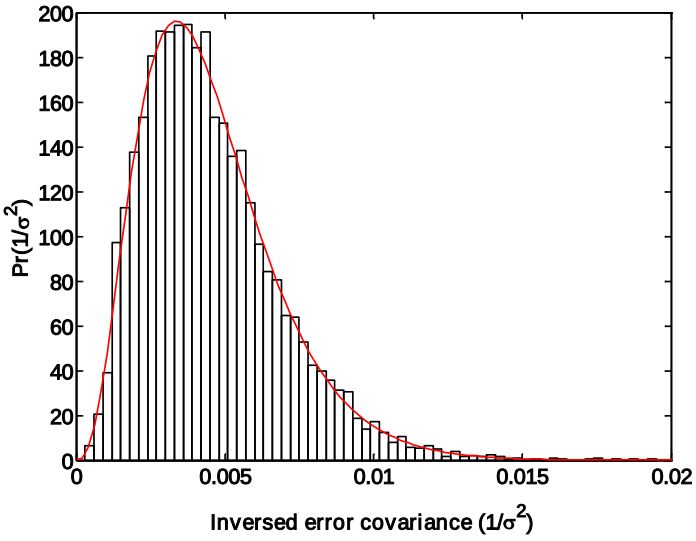

Figure 3-14: Gamma distribution of the inverse of measurement error variance

- (1) FOR k=1:N
  - Sample K_i^k from posterior distribution
  - Sample σ_k^2 from its posterior distribution
  - Sample ε_k as measurement error

$$\varepsilon_k \sim N(0, \sigma_k^2)$$

- (2) Calculate the power output

$$P_k = K_1^k N f^{K_2^k} + K_3^k NVB + \varepsilon_k$$

- (3) END FOR

Figure 3-15: Posterior predictive distribution algorithm

Table 3.4: Validation Tests cutting conditions, measured power and tool flank wear

Test [#]	V_c **[m/min]**	f **[mm/rev]**	P **[×10^{-3} hp]**	VB **[µm]**
1	30	0.18	64	84
2	35	0.15	65	73
3	40	0.12	56	92
4	45	0.05	41	80

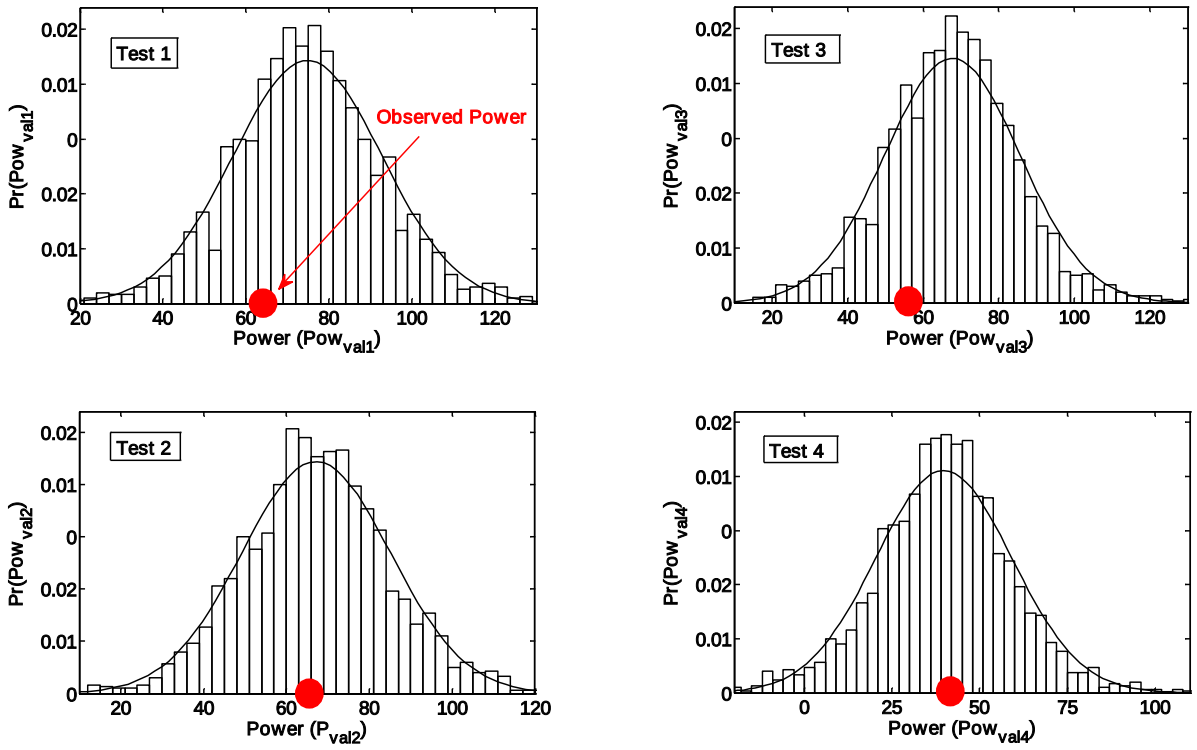

Figure 3-16: Posterior predictive distribution with 95% confidence interval (black bars) and spindle power – Validation test 1-4

Table 3.5: Percentage Error of prediction and measurement

Test [#]	$P_{measurment}$ **[×10^{-3} hp]**	$P_{predicted}$ **[×10^{-3} hp]**	**Error [%]**
1	64	76	18
2	65	68	4
3	56	67	19
4	41	39	5

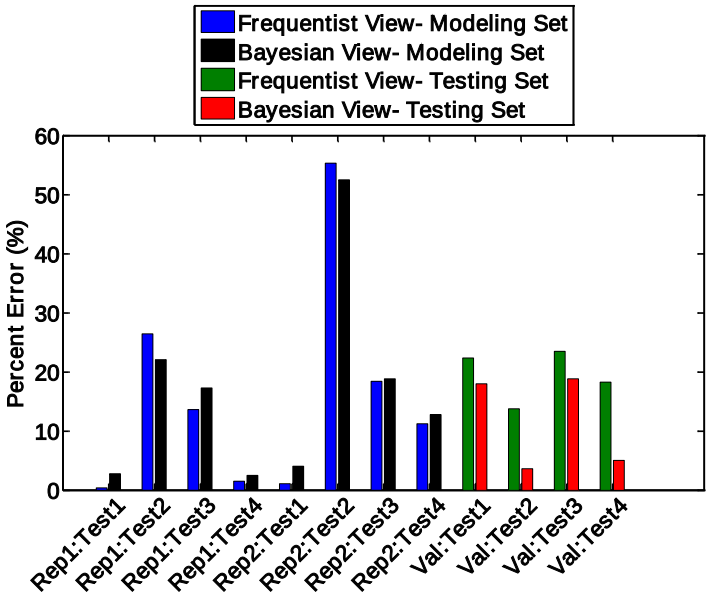

Figure 3-17: Percentage error of tests used for model establishment and validation tests – comparison of Bayesian and Frequentist views

Concluding Remarks

This work deals with the Bayesian parameter identification of a mechanistic model of the tool wear. The focus of this section was on hard-to-machine Ni-based material Rene-108 which has been shown to have a poor machinability due to several reasons such as low thermal conductivity and high strength. High tool wear rate while machining this material is a major challenge in industrial application since it limits the productivity rate. In addition, excessive tool wear can damage surface quality and causes undesired residual stress beneath the machined surface. The aforementioned challenge also limits the available number of experiments for establishing accurate models since the cutting tool worn-out quickly. To have the accurate estimation of the unknown model parameters, Bayesian parameter identification method, *i.e.* a hybrid technique of Markov-Chain Monte-Carlo was deployed. This technique can be used for when limited experiments are

available, a feature that is beneficial and cost-effective in studying Ni-based alloys. The main conclusions are summarized as below:

- The Hybrid Gibbs-Metropolis algorithm was formulated for prediction of the unknown parameters in the nonlinear mechanistic cutting power model in milling of Rene-108. The Metropolis algorithm with a symmetric proposal density was used for predicting the model parameters, while the Gibbs sampler used for updating measurement error variance.
- A design of experiment with mild and aggressive cutting condition was used along with high frequency DAQ to capture wide range of tool wear and spindle power consumption. The performance of algorithm improved significantly after using a data from the first run of MCMC as prior belief for the second run. Predicted parameters were successful in estimating the spindle power consumption with a maximum 18% error and average error of 8.5%.
- Performance of the Bayesian inference was compared to deterministic approach and it was shown that the Bayesian inference outperforms the deterministic method by reducing the prediction error by more than 50%.

CHAPTER FOUR

4. PROBABLISTIC TOOL WEAR ESTIMATION IN MILLING

Monitoring tool wear in machining processes is one of the critical factors for maximizing profitability and productivity by redu rcing machine downtime. However, tool wear estimation is still considered a challenge in modern manufacturing processes due to machining, workpiece material composition and measurement uncertainties. A previously developed model from the Chapter 3 will be used in this chapter for tracking the progressive tool wear in terms of its mean and variance (uncertainty) in the Kalman filter framework. Furthermore, to increase the performance of the filter, a laser measurement system is deployed in collaboration with a low cost sensing technology of measuring spindle power consumption.

Kalman Filter Framework

Using the Bayes rule, Rudolf Kálmán introduced a method of estimation where a Gaussian model is assumed for the states of stochastic events. For state estimation, the Kalman filter uses a discrete linear state space Equation 4-1, where k is the time step, A is a matrix that relates the states at the previous time step (k-1) to the current time step (k), B is a matrix that relates inputs u at the previous time step to the current states, and w_k is the noise (uncertainty) for states. This noise is assumed to have a normal distribution with zero mean and variance Q (Equation 4-2). The measurement equation is described as a discrete stochastic model that relates current state to the measured signals (Equation 4-3), where z_k is the measured signal, H is a matrix that relates current states of the system to

the most recent measurements and v_k is the measurement noise which is assumed to have a normal distribution with zero mean and variance R (Equation 4-4).

$$x_k = Ax_{k-1} + Bu_{k-1} + w_{k-1} \quad \text{4-1}$$

$$w_k \sim N(0, Q) \quad \text{4-2}$$

$$z_k = Hx_k + v_k \quad \text{4-3}$$

$$v_k \sim N(0, R) \quad \text{4-4}$$

Assuming observability of states, the Kalman filter is an optimal observer that minimizes the expected value of sum of squared errors of x_k given the previous observations. Using the closed-loop observer formulation for state estimation (Equation 4-5 with K as the observer gain), Kalman filter starts with *a priori* information at time k, which is updated based on the previous knowledge at time k-1. As soon as the measurements become available, *a priori* will be updated to find *a posteriori* of states.

$$\hat{x}_k = A\hat{x}_{k-1} + Bu_{k-1} + K(z_k - H\hat{x}_k) \quad \text{4-5}$$

The first update in the algorithm to find *a priori* is called the time update and the second update to find *a posteriori* is called the measurement update. Time and measurement updates are described as Equations 4-6 to 4-10.

1. Time update

$$\hat{x}_k^- = A_{k-1}\hat{x}_{k-1} + Bu_{k-1} \quad \text{4-6}$$

$$P_k^- = A_{k-1}P_{k-1}A_{k-1}^T + Q_{k-1} \quad \text{4-7}$$

2. Measurement update

$$K_k = P_{k-1}^{-} H_k^T (H_k P_{k-1}^{-} H_k^T + R_k)^{-1} \quad \text{4-8}$$

$$\hat{x}_k = \hat{x}_k^{-} + K_k (z_k - H_k \hat{x}_k^{-}) \quad \text{4-9}$$

$$P_k = (I - K_k H_k) P_k^{-} \quad \text{4-10}$$

Here, P_k^{-} is the *a priori* error variance of states, P_k is the *a posteriori* error variance of states, $\hat{x}_k^{-}$ is the *a priori* estimation of states, $\hat{x}_k$ is the *a posteriori* estimation of states, K_k is the Kalman gain, and R_k is the measurement error variance [96]. Note that when a measurement is not available, only the time update of the Kalman filter will be used. In that case, the current knowledge of states makes future predictions possible. Measurement covariance (R_k) can be calculated by evaluating multiple measurements of the signal z when the system is in static mode. On the other hand, calculating the state noise is not that simple. A suggested solution is where the states can be measured offline; in that case the maximum covariance of multiple offline measurement of states can be considered as the state error covariance Q_k. However, tuning the state covariance matrix by trial and error is also suggested to get the best estimation. The Kalman filter algorithm and its schematic is shown in Figure 4-1 and Figure 4-2.

- (0) Initialize states
  - Choose x_0
  - Choose P_0
- (1) Start with k=1
- (2) Time Update
  - Calculate $\hat{x}_k^- = A_{k-1}\hat{x}_{k-1} + Bu_{k-1}$
  - Calculate $P_k^- = A_{k-1}P_{k-1}A_{k-1}^T + Q_{k-1}$
- (3) Kalman gain
  - Calculate $K_k = P_{k-1}^- H_k^T (H_k P_{k-1}^- H_k^T + R_k)^{-1}$
- (4) Measurement update
  - Calculate $\hat{x}_k = \hat{x}_k^- + K_k(z_k - H_k\hat{x}_k^-)$
  - Calculate $P_k = (I - K_k H_k)P_k^-$
- GO to line (1)

Figure 4-1: The Kalman filter algorithm

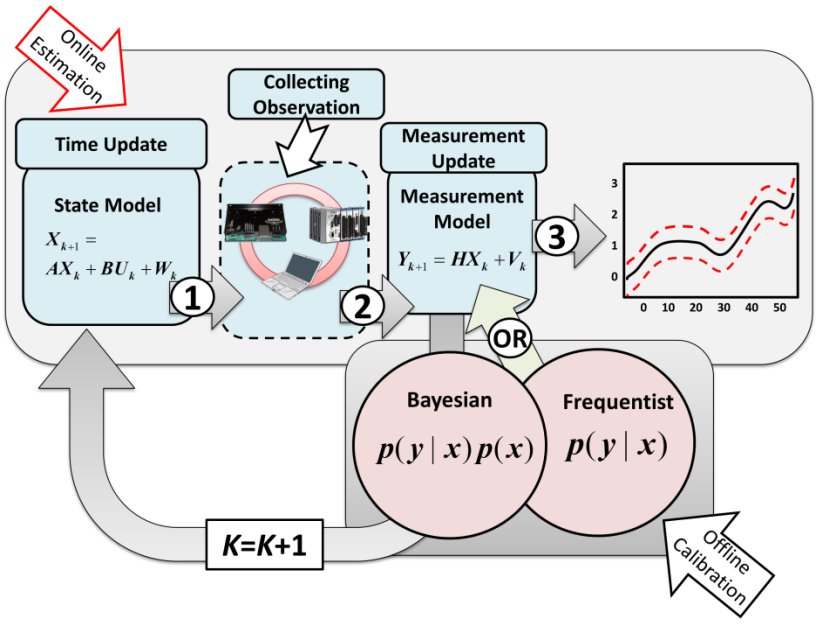

Figure 4-2: The Kalman filter diagram where the Bayesian-based or Frequentist-based models can be fed into as the measurement model

Experimental Setup for Continuous Cutting in Milling

The same experimental setup as Chapter 3 was used in this chapter. However, a total of 8 experiments (see Figure 4-3) with 3 replications were conducted to study the tool

flank wear when machining the R-108 Ni-based superalloy. At the chosen width of cut, 24 tests were conducted on the block: 8 tests with 3 replications. According to the Table 3.3, chipping has a significant contribution to the tool life. Therefore to avoid or delay chipping it was decided to keep the cutting condition at the least aggressive condition and constant throughout the whole experiments. Hence depth of cut, cutting velocity and feed for each pass were chosen at 0.5 mm, 25 m/min and 0.1 mm/rev respectively. Each replication started with a sharp insert and continued with the same insert until extensive chipping was observed. After only eight consecutive cuts, the insert reached a failure region as shown in Figure 4-4, where chipped off coating can be seen in Figure 4-4(b).

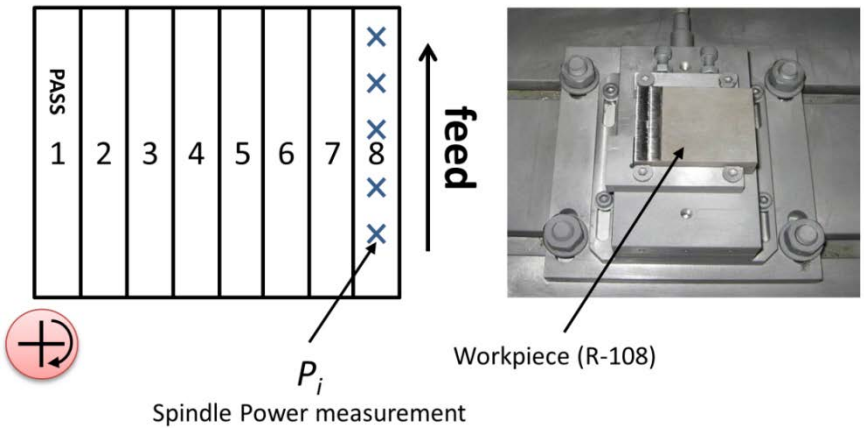

Figure 4-3: Schematic of continuous milling experiments

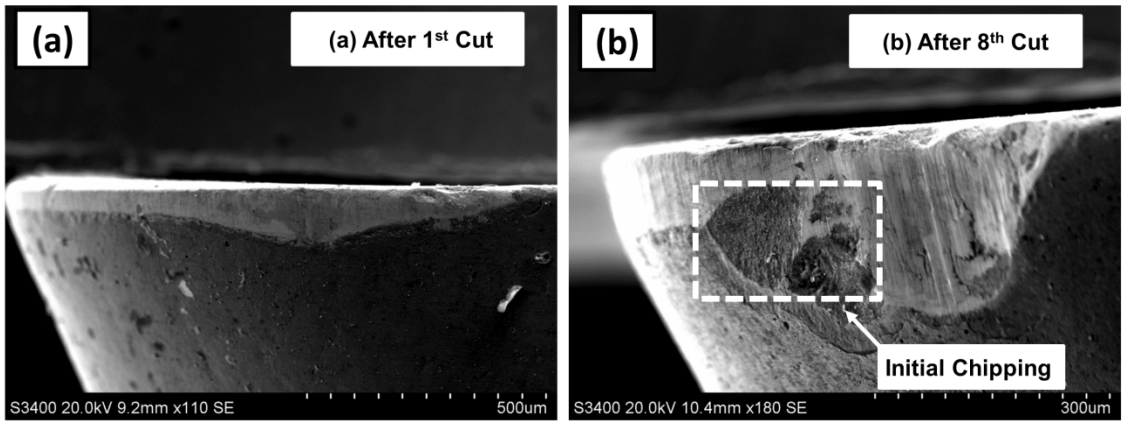

Figure 4-4: Progress of the tool flank wear from the (a) 1st cut to (b) 8th cut

Same insert and tool holder as in Chapter 3 were used in these series of tests. However, the difference is that the fresh unworn inserts were used at the beginning of each test, and operation was continued with the same insert until reaching a catastrophic failure (8 passes in total). Spindle power consumption was measured in 5 cutting distances (shown with "×" mark in Figure 4-3), each around 10, 20, 30, 40 and 50 mm. In Figure 4-5, an exemplified description of the smoothed spindle cutting power is shown for test 1.3. Measured power and the tool flank wear of all the 3 replications are shown in Table 4.1. Note that only the power at the 5th location of workpiece, *i.e.* P_5 is shown in Table 4.1.

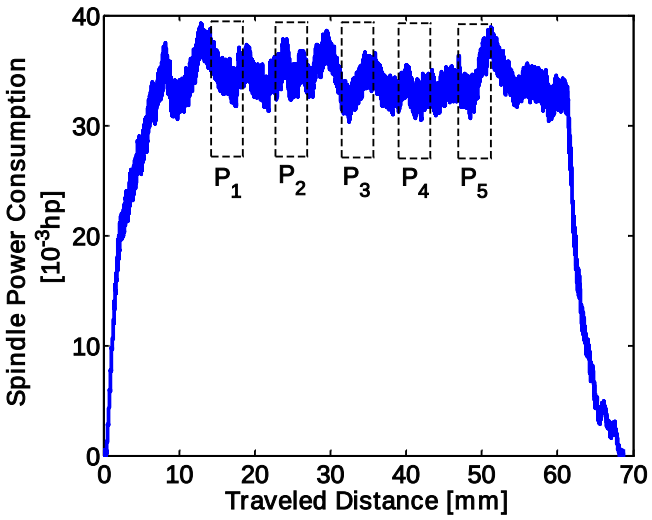

Figure 4-5: Smoothed cutting power for test 1.3

Table 4.1: Spindle power and flank wear measurement for replication sets

Replication 1			**Replication 2**			**Replication 3**		
Test	P_5	*VB*	Test	P_5	*VB*	Test	P_5	*VB*
[#]	[$\times 10^{-3}$ hp]	[μm]	[#]	[$\times 10^{-3}$ hp]	[μm]	[#]	[$\times 10^{-3}$ hp]	[μm]
1.1	29	84	2.1	32	83	3.1	32	81
1.2	32	89	2.2	36	87	3.2	33	87
1.3	24	100	2.3	38	103	3.3	35	99
1.4	33	108	2.4	37	107	3.4	34	103
1.5	36	111	2.5	44	109	3.5	39	109
1.6	41	116	2.6	30	116	3.6	38	115
1.7	37	119	2.7	41	125	3.7	36	116
1.8	36	125	2.8	44	127	3.8	42	120

Stochastic Model of Tool Flank Wear

The dynamic behavior of tool wear is nonlinear at the initial stages, linear at intermediate stages, and nonlinear at the final stages before catastrophic failure [41]. Due to the high strength and hardness of R-108, the progress of the tool wear was very fast, and the first stages of the tool wear were not captured while testing. Hence, tool wear

progress was considered as a linear function of volume of material removed (*MR*) while machining.

Considering the linear region for tool wear and assuming the flank wear *VB* and slope of the tool wear growth rate VB' as the states of the system, the discretized state space equation can be written as Equation 4-11, where Δt is the time-step size. Assuming r_e as radial immersion, Δt can be written equivalent to the volume of removed material (*MR*) as Equation 4-12. Because the cutting conditions were kept constant, the rate of tool wear (VB') is constant and therefore can be written as Equation 4-13.

$$\frac{VB(k)-VB(k-1)}{\Delta t} = VB'(k) = VB(k-1) + VB'(k)\Delta t \tag{4-11}$$

$$\Delta t = \frac{120\pi D \times MR}{fVa_p r_e} \tag{4-12}$$

$$VB'(k) = VB'(k-1) \tag{4-13}$$

The state error should be included into the state equations as normally distributed noise. The error variances for tool wear and tool wear rate are assumed to be independent of one another as well. The stochastic state space equation is described in matrix format in Equations 4-14 and 4-15.

$$\begin{bmatrix} VB(k) \\ VB'(k) \end{bmatrix} = \begin{bmatrix} 1 & MR \\ 0 & 1 \end{bmatrix} \begin{bmatrix} VB(k-1) \\ VB'(k-1) \end{bmatrix} + \begin{bmatrix} w_1(k) & 0 \\ 0 & w_2(k) \end{bmatrix} \tag{4-14}$$

$$\begin{bmatrix} w_1(k) \\ w_2(k) \end{bmatrix} \sim N\left(\begin{bmatrix} 0 \\ 0 \end{bmatrix}, \begin{bmatrix} Q_1 & 0 \\ 0 & Q_2 \end{bmatrix} \right) \tag{4-15}$$

The variance Q_1=1.36×10^2 μm^2 was calculated based on the maximum variance in tool flank wear measurements between replications and the variance Q_2 = 1.6×10^{-6}

$\mu m^2/mm^6$ was calculated as the variance between slopes of linear progressive tool wear. In all the experiments, cutting conditions were kept constant, so Equation 3-28 can be simplified as a linear Equation 4-16 between spindle power consumption and tool wear. The parameters K_{p1} and K_{p2} were determined from the results of Bayesian and Frequentist methods described in Chapter 3. These parameters are shown in Table 4.2.

$$P = K_{p1} + K_{p2}VB \tag{4-16}$$

Measurement error variance for spindle power was calculated from the experimental results the same way as Q_1 as 11.3×10^{-3} hp^2 and Equation 4-16 was re-written in discrete matrix format to run the Kalman filter as given in Equations 4-17 and 4-18 where the measurement error $v(k)$ was defined as a normal distribution with zero mean and covariance matrix R. Note that, it is possible to tune the measurement errors and states error covariance based on the performance of the filter. By decreasing R, the effect of *a priori* will be strengthened on the estimations.

Table 4.2: Comparison of Bayesian and linear regression estimation

Parameter	**Linear regression analysis**	**Bayesian parameter inference**
Model	$P = K_1 N f^{K_2} + K_3 NVB \xrightarrow{\text{cte. cutting condition}} P = K_{p_1} + K_{p_2} VB$	
K_{p1}	29	15.8
K_{p2}	75.1	215.4

$$\Delta P(k) = \begin{bmatrix} K_{p2} & 0 \end{bmatrix} \begin{bmatrix} VB(k) \\ VB'(k) \end{bmatrix} + v(k) \tag{4-17}$$

$$v(k) \sim N(0, R) \tag{4-18}$$

To run the Kalman filter, an initial point and an initial covariance for the states are required. The initial point (x_0) was calculated simply as the mean of predicted flank wear from test 1.1, 2.1, and 3.1. To find the initial error of the flank wear, the error between the mean of measured flank wear for first tests of each replication which appears as expected value of $VB_{i,1}$ in Equation 4-19 and estimated flank wear based on measured power which appears as expected value of $\Delta P_{i,1}/K_{p2}$, was calculated. The error of the flank wear rate was calculated as the difference between the slope of measured the flank wear (first term in Equation 4-20) and predicted flank wear using the test sets (1.1, 1.2 and 1.3) and (2.1, 2.2 and 2.3) for each replication (second term in Equation 4-20). Combining these two errors together, the initial error covariance of tool wear and tool wear rate were 4.8μm and 7.7$\mu m^2/mm^3$ respectively.

$$e_0 = E\left(VB_{i,1}\right) - E\left(\frac{\Delta P_{i,1}}{K_{p1}}\right) \quad i \in \{1,2,3\} \tag{4-19}$$

$$e_0' = E\left(\frac{VB_{i,1} - VB_{i,2}}{MR}\right) - E\left(\frac{P_{i,1} - P_{i,2}}{K_{p2} MR}\right) \quad i \in \{1,2,3\} \tag{4-20}$$

$$P_0 = \begin{bmatrix} e_0 & e_0' \end{bmatrix} \begin{bmatrix} e_0 \\ e_0' \end{bmatrix} = \begin{bmatrix} e_0^2 & e_0 e_0' \\ e_0 e_0' & e_0'^2 \end{bmatrix} \tag{4-21}$$

Before proceeding to the next section, it is worth considering only the deterministic measurement model (Equation 4-16) with linear regression analysis and studying its performance for the tool flank wear estimation. The linear curve fit and corresponding $R^2_{adjusted}$ as goodness of fit is shown in Figure 4-6. According to this figure, 0.51, 0.58 and 0.75 values of $R^2_{adjusted}$ shows a weak linear relation between the measurements and

the tool flank wear which is due to the low signal to noise level (SNL) of the collected power and incompleteness of measurement model. This can be compensated by adding the state model (Equation 4-14) to the measurement model (Equation 4-17) and use filtering method to reduce the effect of noise.

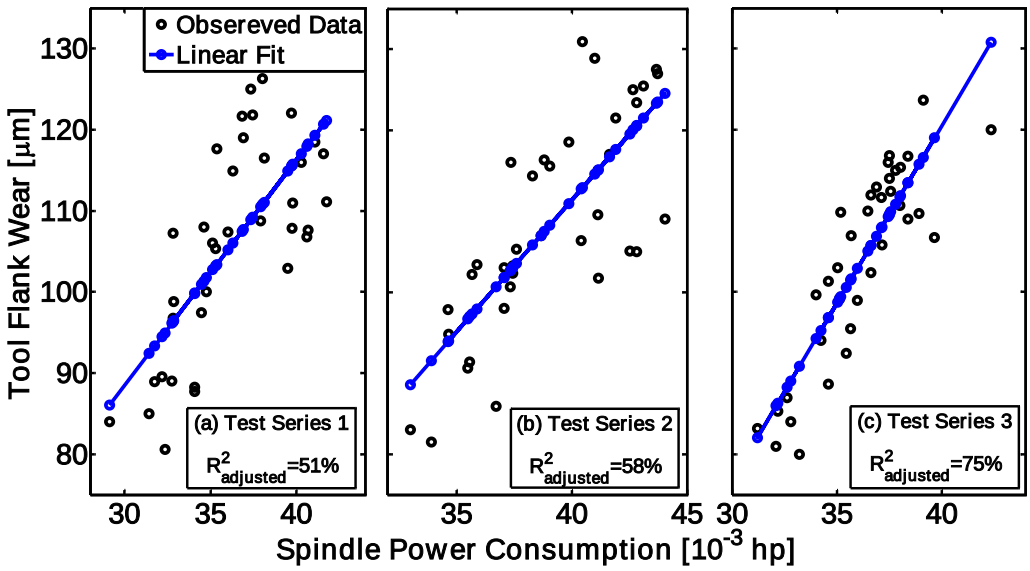

Figure 4-6: Deterministic linear regression for the tool flank wear estimation using spindle power measurement

Results Using the Kalman filter

To run the Kalman filter the coefficients K_{p1} and K_{p2} of the measurement model can be chosen from the maximum likelihood parameter estimation (Frequentist view) or Bayesian parameter inference (Bayesian view). According to Table 4.2 (columns 2-3), these values have drastic differences. Therefore, each method offers different measurement model.

Bayesian and Frequentist models were fed as the measurement model in the Kalman filter. The Kalman filter outputs using these two approaches are shown in Figure 4-7 and

Figure 4-8. A significant error reduction in the output of the Kalman filter was observed when a Bayesian-based model was used as the measurement model. However, unlike the measured tool wear, the estimated wear does not exhibit a linear monotonically increasing function specifically for first and second replications in Figure 4-8. This behavior is attributed to insert chipping. When small pieces of the insert coating chips off the flank face during the operation, a sudden drop follows by a rise in the measurement can be detected. Since the chipped particle at the tool tip reduces the contact area between flank face and the workpiece, the power magnitude cannot reach the same magnitude when the rubbing surfaces had full contact. This effect shown in Figure 4-9 appeared as a reduction in the power signal, which eventually affects the estimated flank wear causing an unrealistic drop in the estimated wear. Note that the Kalman filter estimates the mean and covariance of the states, therefore uncertainty in Figure 4-7 and Figure 4-8 represents the variance of estimated tool wear probability density; the evolution of the tool wear represented by the Gaussian function is shown in Figure 4-10.

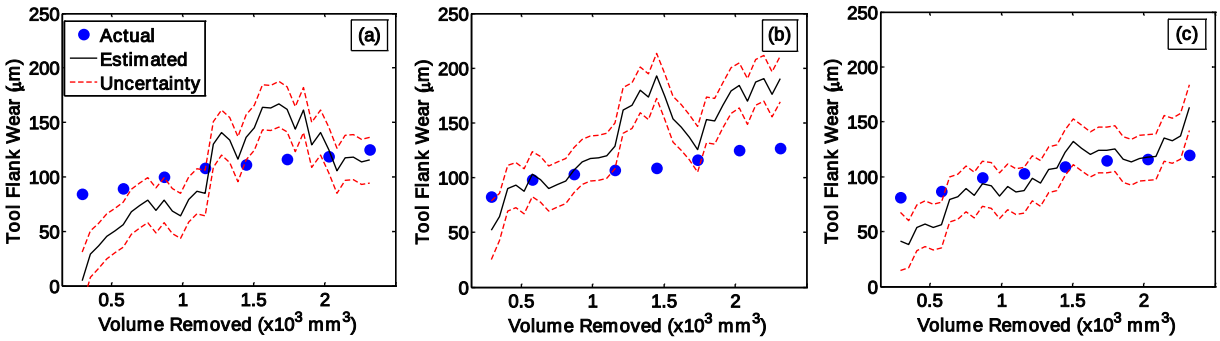

Figure 4-7: Estimated tool flank wear and its corresponding uncertainty when Frequentist-based power model is used, (a) first replication, (b) second replication and (c) third replication

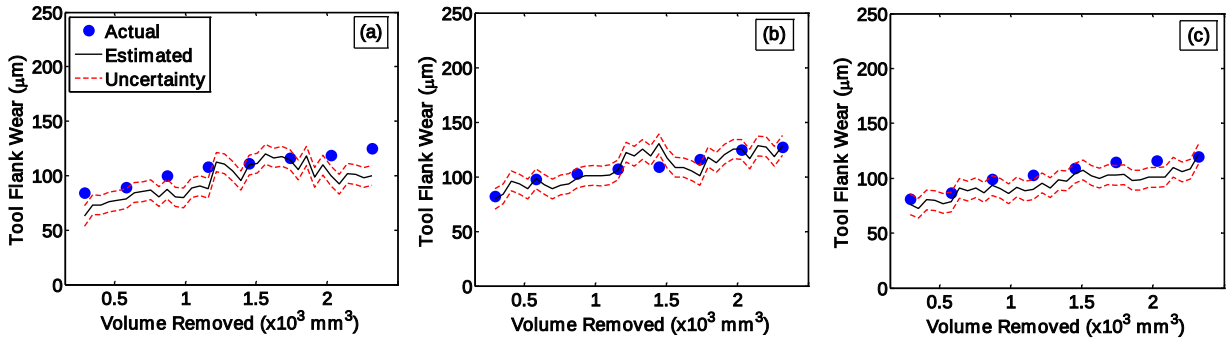

Figure 4-8: Estimated tool flank wear and its corresponding uncertainty when Bayesian-based power model is used, (a) first replication, (b) second replication and (c) third replication

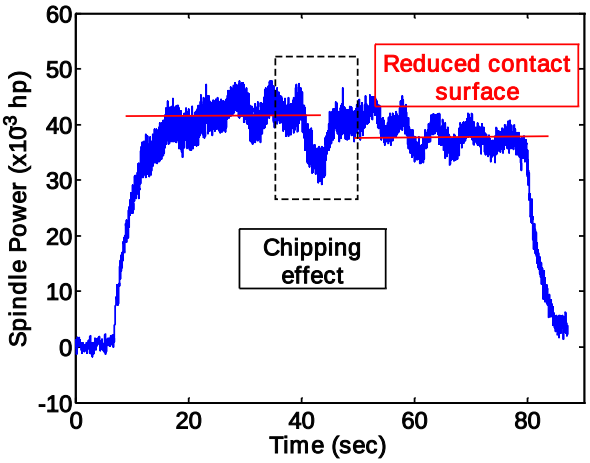

Figure 4-9: Chipping effect as drop and rise in power signal for test 1.7

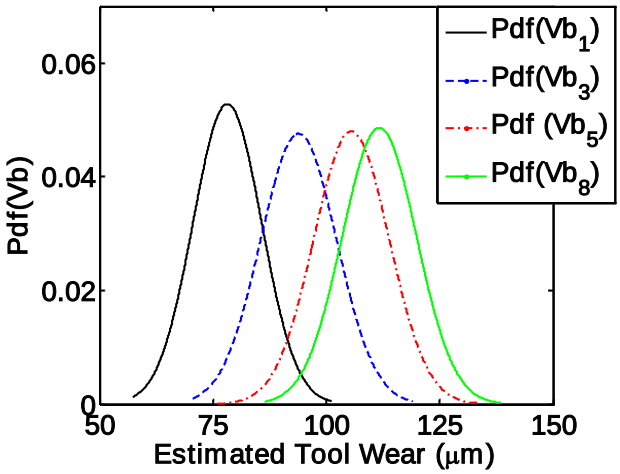

Figure 4-10: Evolution of tool wear distribution over time for the 1st replication (with Bayesian-based measurement model), subscript *i* represents the estimated tool wear at the actual measurement point

Feasibility of Fusing Direct and Indirect Measurements for TCM

As discussed above, excessive chipping while milling Rene-108 and low SNL of the spindle power (which appears as a measurement noise) produced a non-increasing function of the estimated tool wear. One simple compensating solution is the visual inspection of the tool wear after certain number of cuts and updating the Kalman filter gain (K). However, this leads to the interruption of automated machining operation and adds human error into the estimated results. The other alternative is using a pre-installed non-contact probe in the machine to read the tool wear length after each pass and relate its change to the tool wear. A BLUM laser measuring system was utilized for this purpose. Before and after each pass, the tool length was measured 3 times, by the laser measuring system and the change in the tool length was saved in the machine. This way a direct measurement method can be fused with indirect measuring technique to improve

the estimation accuracy. The BLUM measuring device when measuring the tool length is shown in Figure 4-11.

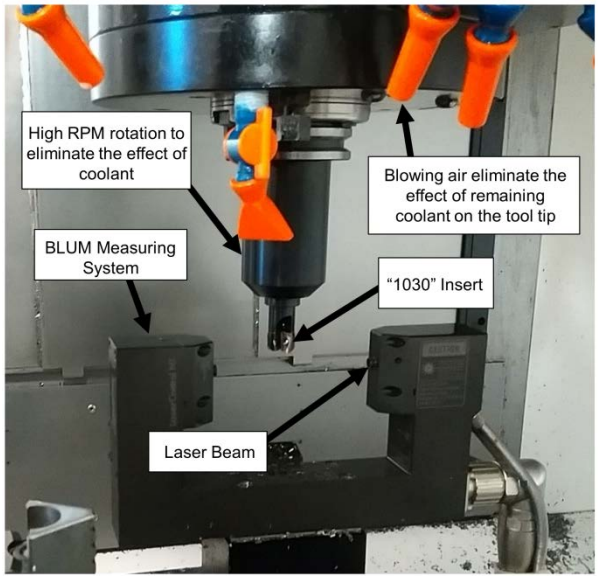

Figure 4-11: BLUM laser measuring system conventionally used for measuring tool offset

Tool Length Change Model

As the tool wears out during the process, the length of the insert gradually decreases until catastrophic failure occurs. Mechanical Touch probes have already been used to measure tool length change [11]. However, the process is time consuming because it involves multiple repetitions to eliminate the measurement error. The application of laser in assisting the cutting process and reducing tool wear rate by thermal softening of metal has been shown previously in machining operations [97-100]. However, a laser measurement system can also be used as an alternative method that can be implemented for precise and accurate measurement of tool length change and detecting tool breakage. Accuracy, fast multiple measurement, and ability to measure length of the rotating and non-rotating tools are some of the advantages of the laser measurement systems over

mechanical touch probes. Due to the direct contact of the tool to the touch probes, they are prone to mechanical damage, but laser-based systems make non-contact measurement possible and eliminate mechanical damage to the tool or the measurement device. However, accuracy of the machine axis and the laser measurement systems is in the same order, which can induce error into the final results [11]. High cost of implementation is another drawback of such systems.

Considering Figure 4-12, the model relating the change of the tool length to the tool flank wear was derived using the geometry of the insert as shown as in Equation 4-22. Where ψ and λ_s are geometrical properties of the insert which are constants, ΔL is the change in tool length after the cutting process, and K'' is the constant coefficient that is found based on fitting a linear curve on the data. Note that only axial change of the tool length was considered in this work and radial change was neglected. The measurement results with the change in the tool length after each pass is shown in Table 4.3.

$$VB = \Delta L\left(\frac{1}{\tan(\psi)}) - \tan(\lambda_s)\right) \rightarrow VB = K''\Delta L \qquad 4\text{-}22$$

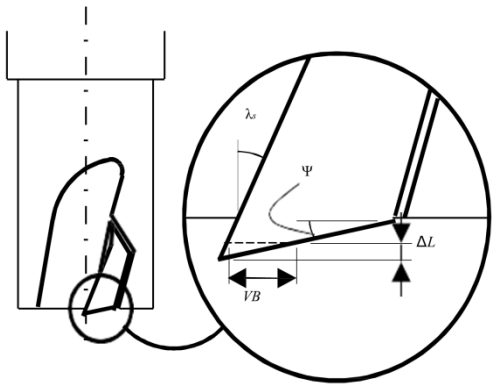

Figure 4-12: Change in the tool length after each pass [11]

Table 4.3: Change in the tool length after each pass

Replication 1		**Replication 2**		**Replication 3**	
Test	ΔL	Test	ΔL	Test	ΔL
[#]	[μm]	[#]	[mm]	[#]	[mm]
1.1	5	2.1	2	3.1	4
1.2	10	2.2	5	3.2	8
1.3	16	2.3	7	3.3	13
1.4	21	2.4	25	3.4	21
1.5	21	2.5	28	3.5	30
1.6	25	2.6	33	3.6	37
1.7	30	2.7	33	3.7	48
1.8	35	2.8	36	3.8	56

Assuming that the spindle power measurement and the tool length change measurement were independent of one another, the measurement model can be written as Equations 4-23 and 4-24, where R_2 is calculated as 1.4×10^{-4} mm^2. This way a direct and indirect measurement of tool wear were fused together in the Kalman filter framework.

The results of estimation are shown in Figure 4-13, where significant improvement was observed. Furthermore, the chipping effect was significantly compensated. To evaluate the improvement of fusing direct method into the indirect method (using only power signal), three errors were selected: the root mean square error (RMSE), mean absolute error (MAE) and maximum error; they are compared in Table 4.4. Moreover, the percentage error between the estimated wear and the actual wear for all the replications are compared in Table 4.5.

$$\begin{bmatrix} \Delta P(k) \\ \Delta TL \end{bmatrix} = \begin{bmatrix} C_2 & 0 \\ K'' & 0 \end{bmatrix} \begin{bmatrix} VB(k) \\ VB'(k) \end{bmatrix} + \begin{bmatrix} v_1(k) \\ v_2(k) \end{bmatrix} \quad \text{4-23}$$

$$\begin{bmatrix} v_1(k) \\ v_2(k) \end{bmatrix} \sim N\left(\begin{bmatrix} 0 \\ 0 \end{bmatrix}, \begin{bmatrix} R_1 & 0 \\ 0 & R_2 \end{bmatrix} \right) \qquad 4\text{-}24$$

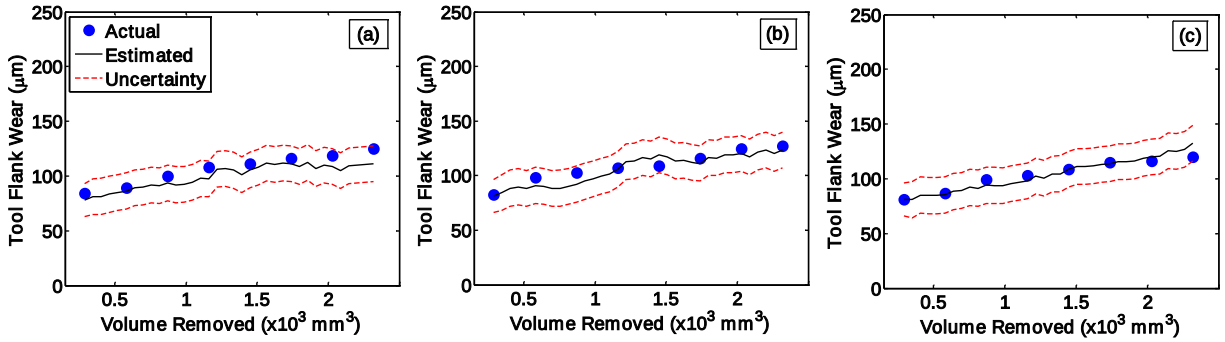

Figure 4-13: Estimated tool flank wear and its corresponding uncertainty when direct and indirect method fused together, (a) first replication, (b) second replication and (c) third replication

Table 4.4: Error comparison for each replication

Method	Replication 1			Replication 2			Replication 3		
	RMSE	MAE	Max. Error	RMSE	MAE	Max. Error	RMSE	MAE	Max. Error
Frequentist-based model	11.1	30.4	79.6	27.1	34.7	83.8	3.1	19.8	43.2
Bayes.-based model	13.8	13.8	25.0	0.06	5.7	21.2	7.9	8.3	15.1
Fusion with direct measurement	7.5	7.4	13.6	5.4	5.4	10.7	3.7	3.7	12.5

Table 4.5: Error between estimated and actual tool wear

Using Indirect Bayesian-based measurement model `											
Replication 1				Replication 2				Replication 3			
Test [#]	$VB_{measured}$ [µm]	$VB_{estimate}$ [µm]	*Error* [%]	Test [#]	$VB_{measured}$ [µm]	$VB_{estimate}$ [µm]	*Error* [%]	Test [#]	$VB_{measured}$ [µm]	$VB_{estimate}$ [µm]	*Error* [%]
1.1	84	63	25	2.1	83	80	4	3.1	81	76	6
1.2	89	79	11	2.2	87	98	13	3.2	87	79	9

1.3	100	87	13	2.3	103	99	4	3.3	99	93	6
1.4	108	88	19	2.4	107	106	1	3.4	103	90	13
1.5	111	110	1	2.5	109	130	19	3.5	109	104	5
1.6	116	115	1	2.6	116	101	13	3.6	115	103	10
1.7	119	100	16	2.7	125	125	0	3.7	116	101	13
1.8	125	100	20	2.8	127	129	2	3.8	120	122	2

Fusing Direct Method with Indirect Bayesian-based measurement model

Test	$VB_{measured}$	$VB_{estimate}$	***Error***	**Test**	$VB_{measured}$	$VB_{estimate}$	***Error***	**Test**	$VB_{measured}$	$VB_{estimate}$	***Error***
[#]	**[µm]**	**[µm]**	**[%]**	**[#]**	**[µm]**	**[µm]**	**[%]**	**[#]**	**[µm]**	**[µm]**	**[%]**
1.1	84	78	7	2.1	83	2	1.5	3.1	81	81	0
1.2	89	86	3	2.2	87	5	7.1	3.2	87	85	2
1.3	100	94	6	2.3	103	11	10.4	3.3	99	94	5
1.4	108	98	9	2.4	107	1	0.8	3.4	103	98	5
1.5	111	106	5	2.5	109	9	9.2	3.5	109	109	0
1.6	116	111	4	2.6	116	4	4.2	3.6	115	114	1
1.7	119	108	9	2.7	125	4	3.7	3.7	116	120	3
1.8	125	111	11	2.8	127	3	2.8	3.8	120	133	11

Concluding Remarks

In this section, a linear optimal estimation method (*i.e.* Kalman filter) was used for the tool flank wear estimation in end-milling of Ni-based superalloy Rene-108. Spindle power consumption was used as the observed signal due to the low cost and easy implementation of Eddy current sensors in CNC machines used in real-life applications as well as the laser measuring system as a direct measuring method. The main conclusions of this section are given as below:

- A discrete linear model of mechanistic tool wear was formulated to be used with the Kalman filter. A design of experiment with relatively mild cutting conditions

was used along with a high frequency DAQ system to capture spindle power consumption.

- Proper variances of state and measurement error were identified and the Kalman filter was tuned to have the least possible error in estimation. It was shown that the Kalman filter can estimate tool flank wear with a maximum error of 25% when spindle power consumption is used as the measuring signal along with the model based on Bayesian parameter inference.
- The effect of establishing the cutting power model using Bayesian inference and MLE inference on the Kalman filter estimation error was discussed and it was shown that the model based on Bayesian inference reduced the estimation error at least 2 times greater than the model based on MLE.
- In addition to spindle power consumption, BLUM laser measuring system was used as a direct sensing device to measure the change in axial length of the insert. A discrete linear model was developed for relating the tool length change to the tool flank wear and fused into the Kalman filter.
- The performance of the Kalman filter with a direct signal from laser device was investigated and it was shown that with using direct measurement the undesired effects of chipping and low SNL in measured power can be compensated. In this case, a more realistic function of estimated tool wear (nearly monotonically increasing function) was generated.

CHAPTER FIVE

5. FUNCTIONAL STATE OF THE TOOL IN TURNING

In the previous chapter, the focus of the work was on establishing a Bayesian-based model of the tool wear and incorporating the model into the online estimation framework. The selection of selected material, insert and machining operation made the insert fails after a few experiments. In this chapter, more stable cutting process (*i.e.* turning) is selected and the focus of study will not be solely on stochastic estimation, and the effect of process uncertainties on end-product quality, workpiece dimensional accuracy and residual stresses will be taken into account.

Extended Kalman Filter

For state estimation, the Kalman filter uses a closed-form discrete state space equation for linear systems and an approximation solution for nonlinear systems known as Extended Kalman filter (EKF). In the EKF, the nonlinear state or measurement model is linearized first and then the Kalman filter is applied for updating the mean and variance of the states. Depending on the system's degree of nonlinearity, the EKF might not be accurate. In this case, deterministic sampling methods such as Unscented Kalman Filters (UKF) [101] or random sampling methods such as Particle Filters (PF) [102] are proposed and are utilized in the manufacturing domain with a continuous resampling strategy for joint state and time-varying parameter estimation by Wang and Gao in predicting tool wear growth and engine performance tracking, and was further validated with experimental results [103-104].

Assuming a discrete nonlinear state and measurement functions as *f* and *g*, the state space representation of the system can be written as Equations 5-1 and 5-2; where *k* is the time step, *x* is the state vector, *w* is the state noise, *v* is the measurement noise and *y* is a measurement. In the context of machining, *x* will be the tool wear; *y* will be the sensor measurement.

$$x_k = f\left(x_{k-1}\right) + w_{k-1} \tag{5-1}$$

$$y_k = g\left(x_k\right) + v_k \tag{5-2}$$

The states and measurements models *f* and *g* can be approximated by the 1st order Taylor expansion into Equations 5-3 and 5-4, where $\hat{x}$ is *a posterior* estimate of the state *x*, and *J* and *G* are Jacobians of functions *f* and *g* with respect to state *x*. These Jacobians are shown in Equation 5-5.

$$x_k \approx f\left(\hat{x}_{k-1}\right) + J\big|_{\hat{x}_{k-1}}\left(x_{k-1} - \hat{x}_{k-1}\right) + w_{k-1} \tag{5-3}$$

$$y_k \approx g\left(\hat{x}_k\right) + G\big|_{\hat{x}_k}\left(x_k - \hat{x}_k\right) + v_k \tag{5-4}$$

$$J_{ij}\big|_{\hat{x}_{k-1}} = \frac{\partial f_i}{\partial x_j}(\hat{x}_{k-1}) \quad G_{ij}\big|_{\hat{x}_k} = \frac{\partial g_i}{\partial x_j}(\hat{x}_k) \tag{5-5}$$

Using the linear Equations 5-3 and 5-4, Kalman filter can be applied as described by time update (Equations 5-6 and 5-7) and measurement update (Equations 5-8 and 5-10).

Time Update:

$$\hat{x}_k^- = f\left(\hat{x}_{k-1}\right) \tag{5-6}$$

$$P_k^- = J\big|_{\hat{x}_{k-1}} P_{k-1} J^T\big|_{\hat{x}_{k-1}} + Q_{k-1} \tag{5-7}$$

Measurement Update:

$$K_k = P_k^- G^T\Big|_{\hat{x}^-} \left(G\Big|_{\hat{x}^-} P_k^- G^T\Big|_{\hat{x}^-} + R_k \right)^{-1} \quad 5\text{-}8$$

$$\hat{x}_k = \hat{x}_k^- + K_k \left(y_k - g\left(\hat{x}_k^- \right) \right) \quad 5\text{-}9$$

$$P_k = \left(I - K_k G^T\Big|_{\hat{x}^-} \right) P_k^- \quad 5\text{-}10$$

Experimental Setup in Turning

The experiments were conducted on an OKUMA CNC lathe machine with Sandvik Coromant CNGG 12 04 04 SGF with TiAlN coating. The workpiece material is annealed IN718 Ni-based alloys which contains 53.8% Ni, 18.44% Cr, 17.33% Fe, 5.31% Nb+Ta, 0.97% Ti, 0.58 Al and less than 0.1% of other elements with 94±2 HRB hardness. The test procedure is as follows: In the preparation step, the IN718 bar was turned three times with a sharp insert with feed 0.05 mm/rev, depth of cut 0.1 mm and cutting speed of 80 m/min. This process was chosen to eliminate any remaining residual stress underneath the cutting surface during the previous operations or manufacturing process. In the next step (testing) the old insert was replaced with a new sharp one to turn 50 mm of IN718 cantilever bar as shown in Figure 5-1. The cutting continues until the measured tool wear width reaches 900μm.

Due to rapid work-hardening and high strength of the IN718, the use of coolant for elongating the tool life was necessary. Therefore, flood coolant lubrication technique with 6% oil concentration was selected in both preparation and testing steps. The coolant pressure, oil concentration and nozzle directions were continuously checked to minimize the coolant effect on the surface integrity parameters and tool life. Moreover, to avoid

chatter and excessive vibrational effects, it was decided to replace the workpiece when the diameter reaches below 20 mm. To study the effect of wear on surface integrity parameters of IN718 in different cutting conditions, the feed was changed from the lowest of 0.05 mm/rev to the highest of 0.15 mm/rev. However, cutting speed and depth of cut were kept constant as 80 mm/min and 0.1 mm/rev as recommended by insert manufacturer. Five replications in feeds 0.05, 0.1 and 0.15 mm/rev were conducted, where the direct measurement of tool flank wear is available for only 4 replications and surface integrity parameters are available in 2 replications. To test the proposed method, two additional replications in feeds 0.063, 0.088, 0.113 and 0.138 mm/rev were conducted, where flank wear data was only available for one replication. This information is summarized in Table 5.1. The spindle power was measured with 100 Hz sampling frequency using Hall effect sensor and NI-cRIO acquisition system shown in Figure 5-1. Then the mean value of the signal between 85%-95% of the cutting length was calculated as measurement signal (y) in 5-9.

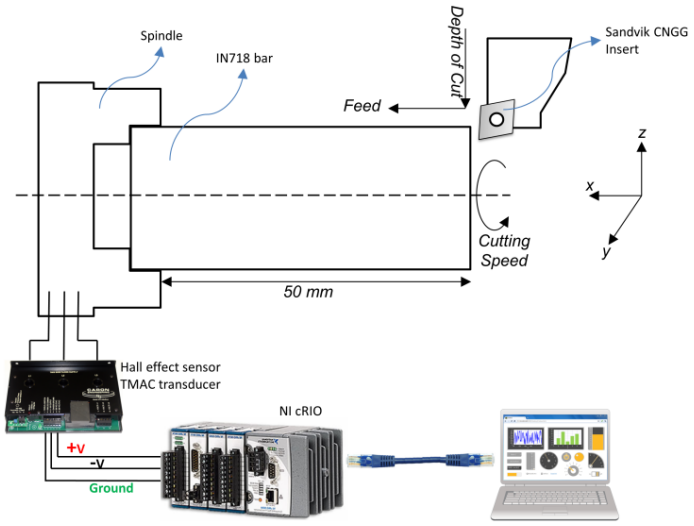

Figure 5-1: Experiment setup with data acquisition system for measuring spindle power

Table 5.1: Design of Experiment (DoE) table for turning IN718

Cutting Speed [m/min]	Feed [mm/rev]	Depth of cut [mm]	Replications with *VB* available [#]	Replications with surface parameters available [#]	Total replications [#]
80	0.050	0.1	4	2	5
80	0.100	0.1	4	2	5
80	0.150	0.1	4	2	5
80	0.063	0.1	1	2	2
80	0.088	0.1	1	2	2
80	0.113	0.1	1	2	2
80	0.138	0.1	1	2	2

The results of the tool wear width and spindle power measurement for all the 4 replications of the feeds 0.05, 0.1 and 0.15 mm/rev is shown in Figure 5-2 to Figure 5-4. The lowest variation in the tool flank wear belongs to the lowest feed (0.05 mm/rev) and the largest variation belongs to the mid-feed (0.1 mm/rev) where significant departure observed after the reaching approximately 200µm of tool wear width).

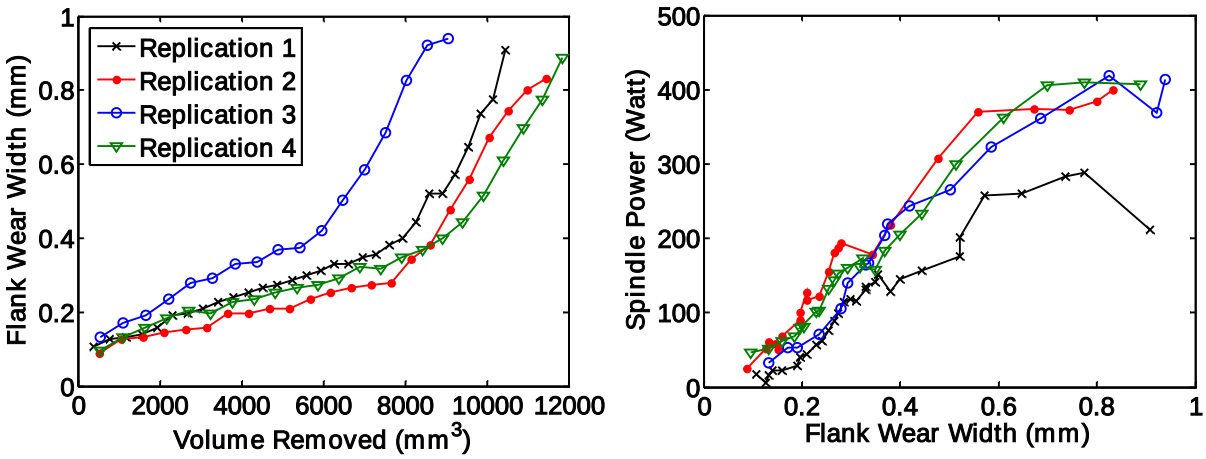

Figure 5-2: Tool wear width (left) and Spindle power (right) for feed of 0.05 mm/rev

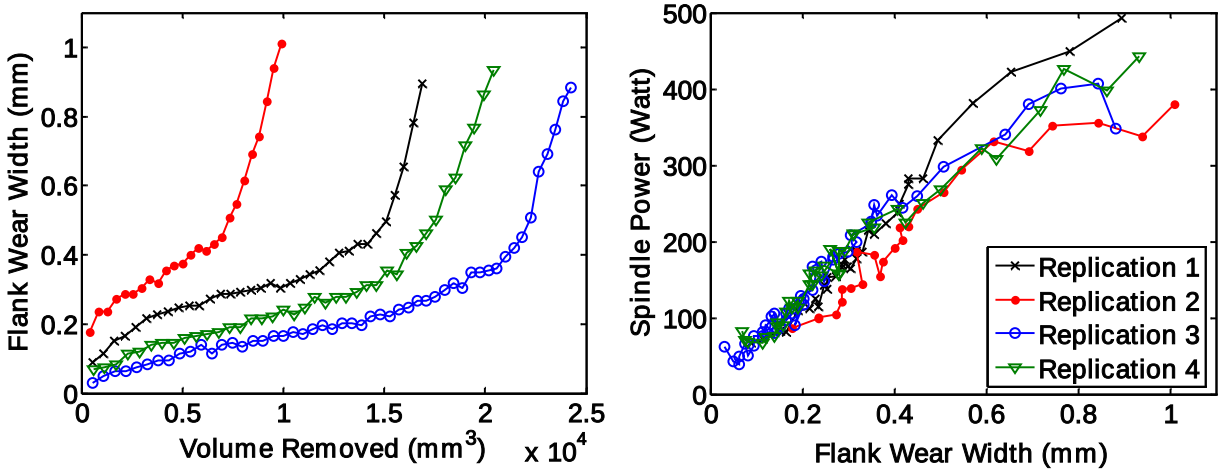

Figure 5-3: Tool wear width (left) and Spindle power (right) for feed of 0.1 mm/rev

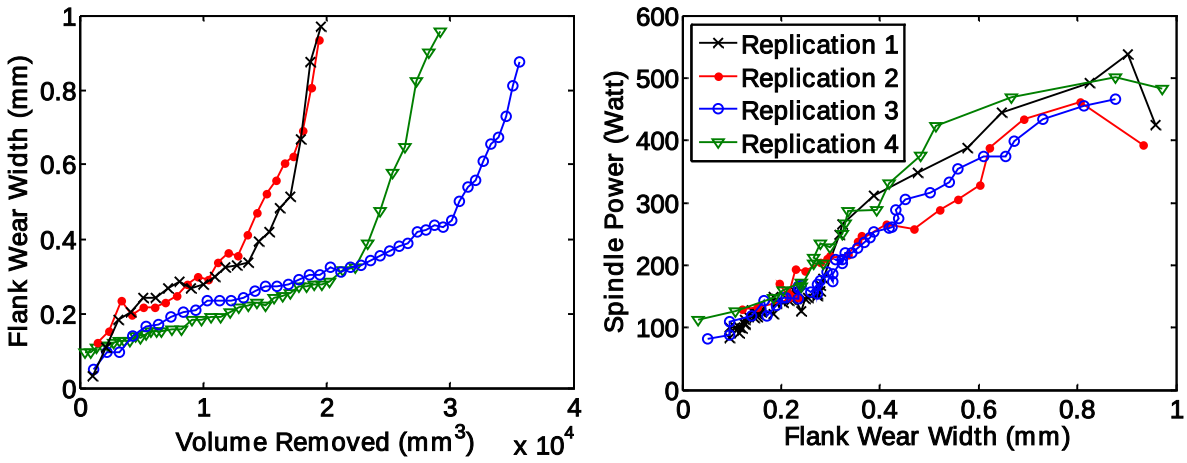

Figure 5-4: Tool wear width (left) and Spindle power (right) for feed of 0.15 mm/rev

Identification of Tool flank Wear Mechanisms in Turning IN718

To better capture mechanisms of wear on the flank face of the tool, a Scanning Electron Microscope (SEM) was used along with x-ray elemental analysis. The evolution of wear from initial cut to 300, 600 and 900 µm is shown in Figure 5-5. A closer look to the elemental analysis results of worn tool (300 and 900 µm) shown in Figure 5-6 and Figure 5-7, reveals the high content of elements nickel and chromium on the flank face

which shows the existence of temperature-driven adhesion mechanism. Also, high content of Tungsten on the flank face shown in Figure 5-7(d), demonstrates the additional damage to the coating of the insert due to high load and temperature where peeled off coating is observable in Figure 5-7(b). In summary, abrasion as an imminent result of friction between tool and workpiece in addition to adhesion, and chipping at the tip of the tool contribute most to the tool failure in turning IN718. As mentioned by Zhu *et al.* existence of cobalt content on the carbide tools represents the diffusion wear [14]. Since low content of cobalt was observed on the flank face, it was concluded that diffusion mechanism has no contribution to the wear evolution.

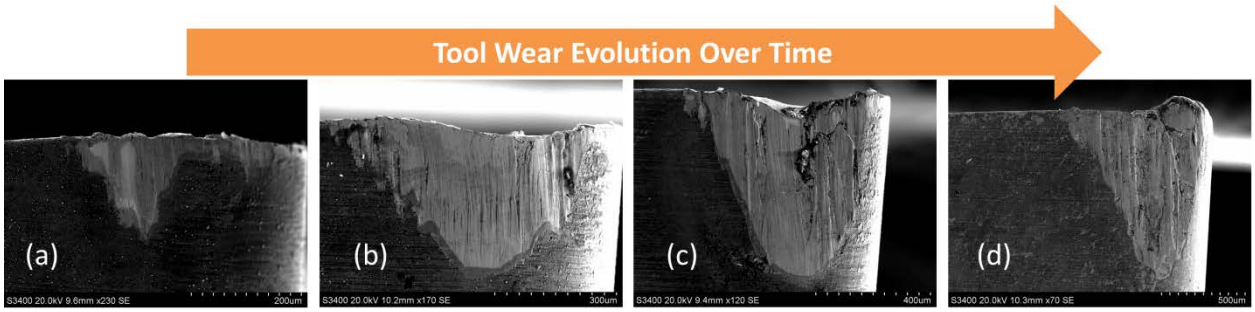

Figure 5-5: Evolution of tool flank wear for cutting feed of 0.05 mm/rev, cutting speed 80 m/min and depth of cut 0.1 mm, (a) initial wear, (b) 300µm of flank wear, (c) 600µm of flank wear, and (d) 900µm of flank wear

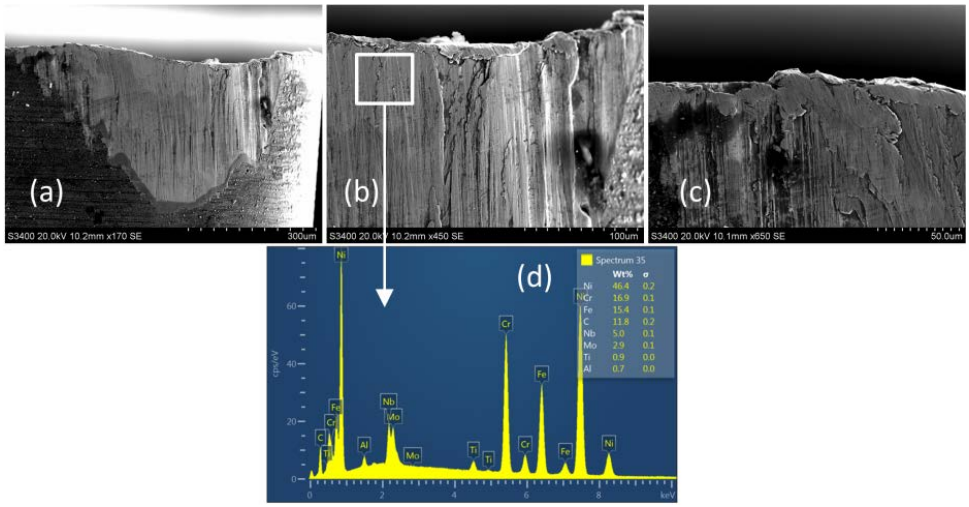

Figure 5-6: Detailed view of the for (a) 300µm flank wear width (b) 3x magnification at the tool tip, (c) 60x magnification at the tool tip and (d) X-ray elemental analysis and high content of nickel demonstrates existence of adhesion mechanism

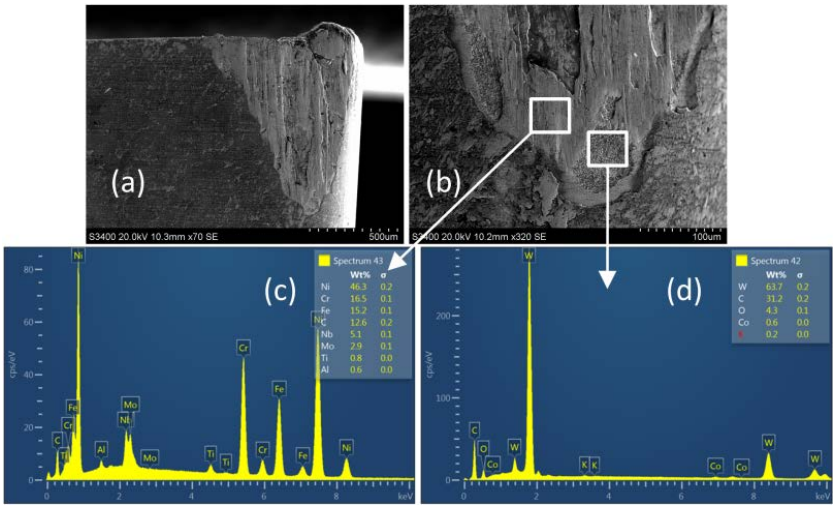

Figure 5-7: Detailed view of the for (a) 900µm flank wear width (b) 5x magnification at the bottom end of wear land, (c) X-ray elemental analysis with high content of nickel as a sign of adhesion (d) X-ray elemental analysis and high content of tungsten as a sign of damaged coating

Stochastic State and Measurement Models

The tool wear width in the Figure 5-2 to Figure 5-4 can be represented by an empirical 3rd order polynomial function with more than 95% R^2_{adj} as goodness of fit shown in Equation 5-11, where *MR* denotes material removed, *a*, *b* and *c* are the feed-dependent polynomial coefficients and *VB* is the flank wear width. By taking derivate of this function the *VB* rate can be found as 2nd order polynomial shown in Equation 5-12. However, to write the state space model, the trajectory of the state *VB* is required, *i.e.* the parameter *MR* should be eliminated from the Equations 5-11 and 5-12 and the *VB* rate should be written as function of *VB*.

$$VB = aMR^3 + bMR^2 + cMR \tag{5-11}$$

$$VB' = 3aMR^2 + 2bMR + c \tag{5-12}$$

In the 16th century, Gelarmo Cardano found a solution for explicitly obtaining roots from cubic functions. Using the Cardano's formula, a closed-form solution for Equation 5-11 was found and substituted into the Equation 5-12. After some simplifications Equations 5-13 to 5-15 can be derived representing continuous function of *VB* rate and *VB*. In these equations, *w* represents the added normally distributed noise.

$$VB' = 3a\left(\alpha^{\frac{2}{3}} + \beta^{\frac{2}{3}}\right) - 2aA + c - \frac{b^2}{3a} + w \tag{5-13}$$

$$\alpha = -\frac{B}{2} + \sqrt{\frac{B^2}{4} + \frac{A^3}{27}} \;,\; \beta = \frac{B}{2} + \sqrt{\frac{B^2}{4} + \frac{A^3}{27}} \tag{5-14}$$

$$A = \frac{c}{a} - \frac{b^3}{3a^2} \;,\; B = \frac{-VB}{a} + \frac{2b^3}{27a^3} - \frac{bc}{3a^2} \tag{5-15}$$

Writing the *VB* rate in Equation 5-13 as $\frac{VB_k - VB_{k-1}}{\Delta MR}$, the discretized nonlinear state function can be written as Equations 5-16. The last step is linearizing this equation by taking the Jacobian of the nonlinear function *f*. This is shown in Equations 5-17 and 5-18.

$$\begin{aligned} VB_k &= \Delta MR_k \left(3a\left(\alpha_{k-1}^{\frac{2}{3}} + \beta_{k-1}^{\frac{2}{3}} \right) - 2aA + c - \frac{b^2}{3a} \right) + VB_{k-1} + \Delta MR_k w_k \\ &= f\left(VB_{k-1}\right) + \Delta MR_k w_k \end{aligned} \tag{5-16}$$

$$J_k = \frac{\partial f}{\partial VB_{k-1}} = 2a \cdot \Delta MR_{k-1}\left(\alpha_{k-1}^{-\frac{1}{3}} \alpha'_{k-1} + \beta_{k-1}^{-\frac{1}{3}} \beta'_{k-1} \right) + 1 \tag{5-17}$$

$$\alpha'_k = \frac{1}{2a}\left(1 - \frac{B_k}{2}\left(\frac{B_k^2}{4} + \frac{A^3}{27} \right)^{-\frac{1}{2}} \right) \;,\; \beta'_k = \frac{1}{2a}\left(-1 - \frac{B_k}{2}\left(\frac{B_k^2}{4} + \frac{A^3}{27} \right)^{-\frac{1}{2}} \right) \tag{5-18}$$

Unlike *VB* that exhibits a nonlinear progressive curve, average tool wear length (*L*) can be modeled as linear progressive curve. The rate of change for average tool wear length (*L*) was derived from experimental results and is feed-dependent. The discretized state space model of tool wear length is shown in Equations 5-19 and 5-20, where *G* is feed dependent tool length rate, and ψ the zero mean Gaussian noise with variance of 7.5×10^{-11} mm^2.

$$\begin{aligned} L = G \times MR &\xrightarrow{\text{Adding Noise}} L' = G + \psi \\ &\xrightarrow{\text{DISCRETIZATION}} L_{k+1} = L_k + \Delta MRG + \Delta MR\psi_k \end{aligned} \tag{5-19}$$

$$G = -4\times10^{-5} f + 9.7\times10^{-5} \tag{5-20}$$

The next step is developing the relationship of the tool wear and the spindle power. As described in Chapter 3 an analytical solution suggested by Rubenstein based on shape and properties of adhered asperities on the flank face of the tool was used in [92]. As

discussed in Rubenstein work, the cutting force can be written as Equation 5-21, where $F_{c'}$ is a constant for a given tool, geometry and cutting parameters, μ is friction coefficient assumed equal to 0.1 in wet cutting, H_m is the hardness of the tool, L is wear length, VB is wear width and c_1 is a constant. Both parameter L and VB are unknown with their function described in Equations 5-16 and 5-19. They need to be estimated simultaneously. The cutting power is simply the product of cutting force (F_c) and cutting speed (V_m) which is kept constant in all of the experiments of this work.

$$F_c = F_{c'} + c_1 \mu H_m w VB \;\rightarrow\; P = F_{c'} V_c + c_1 V_c \mu H_m L \times VB \qquad 5\text{-}21$$

The product of parameters c_1, V_c, μ and H_m are constants and can be found as the average slope of spindle power versus tool wear width curves. The parameter $F_{c'}$ of Equation 5-21 was considered to be feed dependent. Therefore the product of this parameter to cutting speed represents the amount of power required to cut the material when using a sharp insert. To find the relationship, 4 replications of tests with sharp inserts in 5 different feeds were conducted and a linear model with 93% R^2 was fitted to the data accordingly. The measured results are shown in Figure 5-8 and Table 5.2 and the measurement model is described in Equation 5-22 where f_e represents feed.

Table 5.2: Effect of different feeds on spindle power when sharp tool is used

Power [Watt] $=F_{c'} \times V_c$	**Feed - f_e [mm/rev]**				
	0.05	**0.075**	**0.1**	**0.125**	**0.15**
P_1	33.6	38.6	59.2	48.0	113.8
P_2	24.5	55.6	74.4	71.7	91.7
P_3	39.2	41.1	59.1	83.1	122.9

P_4	40.9	71.7	84.1	81.4	83.1
Average	34.56	51.73	69.22	71.07	102.87
Standard Deviation	7.39	15.29	12.26	16.16	18.59

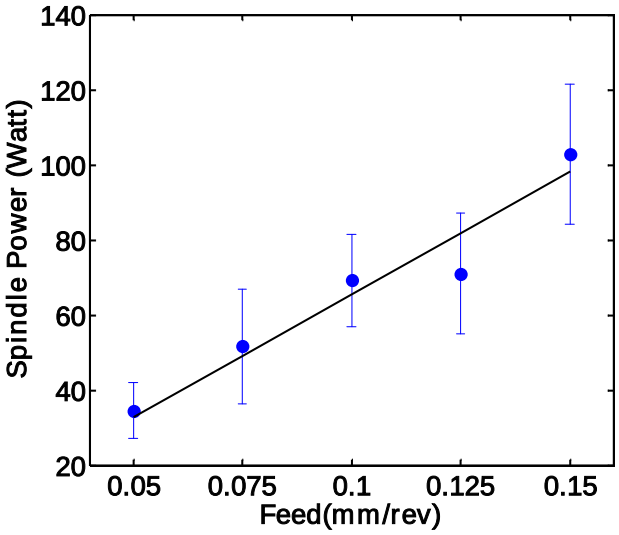

Figure 5-8: Spindle power change with feed when sharp insert is used

$$P = 644LVB + 504 f_e V_c \xrightarrow{DISCRETIZATION} P_k = 645 L_k VB_k + 655 f_e V_c + v_k \qquad 5\text{-}22$$

Uncertainty Quantification for the State and Measurement Models

Since the variation in the spindle power is relatively constant throughout the whole process (see Figure 5-2 to Figure 5-4), the maximum standard deviation of the measured power of the 4 replications of each feed was calculated equal to 20 Watts. On the other hand, a different strategy should be taken to find the uncertainty for the parameters of *VB*. Considering Figure 5-9(a) which shows the standard deviation in different feeds, an interesting fact was emerged. The uncertainties in the tool wear decreases at the beginning of the process and reaches a relatively constant value around *VB* =200-400μm. Then it starts to increase with an increase in the tool wear which explains the large

variation and departure of the tool wear curves after 400µm. The uncertainties behavior which represents the bathtub failure probability curve can be modeled with a closed form function shown in Equation 5-23. Considering this equation and after normalizing the tool wear to be within 0 to 1, an unconstrained optimization method based on simplex search algorithm was chosen to find the unknown coefficients (see Table 5.3). The state model uncertainty was then calculated based on the bathtub curve model and is shown in Figure 5-9(b).

$$q_k = c_1 + c_2\left(\frac{Vb_a(k)}{0.65}\right)^{c_3} + c_4\left(1-\frac{Vb_a(k)}{0.65}\right)^{c_5} \qquad 5\text{-}23$$

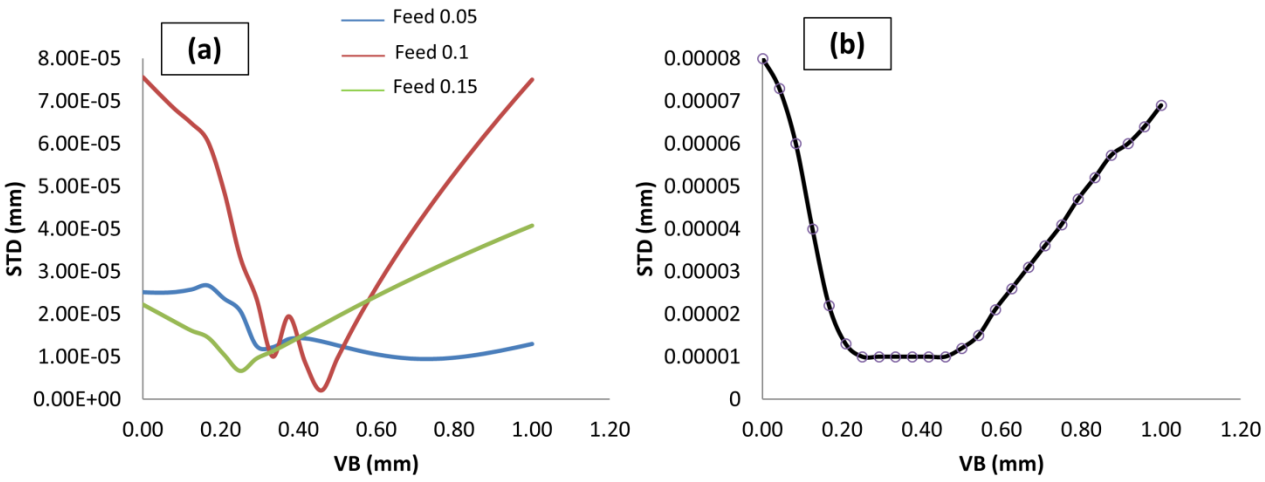

Figure 5-9: Uncertainties propagation (a) different feeds and (b) Modeled bathtub curve for state uncertainty function

Table 5.3: Identified coefficients of bathtub function based on simplex search algorithm

Model	$q_k = c_1 + c_2\left(\frac{Vb_a(k)}{0.65}\right)^{c_3} + c_4\left(1-\frac{Vb_a(k)}{0.65}\right)^{c_5}$				
C_i	C_1	C_2	C_3	C_4	C_5
Value	-1.1E-05	1.8E-05	0.59	1.9E-05	5.00

The state space representation of the system is summarized as Equations 5-24 to 5-27. Note than in Equation 5-24, VB_{k-1} is embedded in α and β parameters as well.

$$\text{State Models} \rightarrow \begin{bmatrix} VB_k \\ L_k \end{bmatrix} = \begin{bmatrix} \Delta MR_k \left(3a\left(\alpha_{k-1}^{\frac{2}{3}} + \beta_{k-1}^{\frac{2}{3}} \right) - 2aA + c - \dfrac{b^2}{3a} \right) + VB_{k-1} \\ \Delta MR_k G + L_k \end{bmatrix} + \begin{bmatrix} \Delta MR_k & 0 \\ 0 & \Delta MR_k \end{bmatrix} \begin{bmatrix} w_{k-1} \\ \psi_{k-1} \end{bmatrix} \quad 5\text{-}24$$

$$w_k \sim N(0, q_k^2) \text{ where } q_k = \left(-2.1 + 5.9\left(\frac{Vb_a(k)}{0.65} \right)^{1.028} + 6.3\left(1 - \frac{Vb_a(k)}{0.65} \right)^{7.43} \right) \times 10^{-5} \quad 5\text{-}25$$

$$\psi_k \sim N(0, \Phi_k^2) \text{ where } \Phi_k = 8.6 \times 10^{-6}$$

$$\text{Measurment Model} \rightarrow P_k = 644 L_k VB_k + 504 f_e V_c + v_k \quad 5\text{-}26$$

$$v_k \sim N(0, r_k^2) \text{ where } r_k = 20 \quad 5\text{-}27$$

EKF Estimation Results and Discussion

To test the performance of the EKF in estimating the tool flank wear width, first its performance was tested on all the 4 replications for feeds 0.05, 0.1 and 0.15 mm/rev. The initial value of VB_0 and L_0 were chosen as 50µm and 380µm with the initial variances of 0.0025 mm^2 and 0.002 mm^2 respectively in all the estimations. The resulting estimated tool flank wear width using EKF and deterministic estimation using only Equation 5-21 is shown in Figure 5-10 to Figure 5-12.

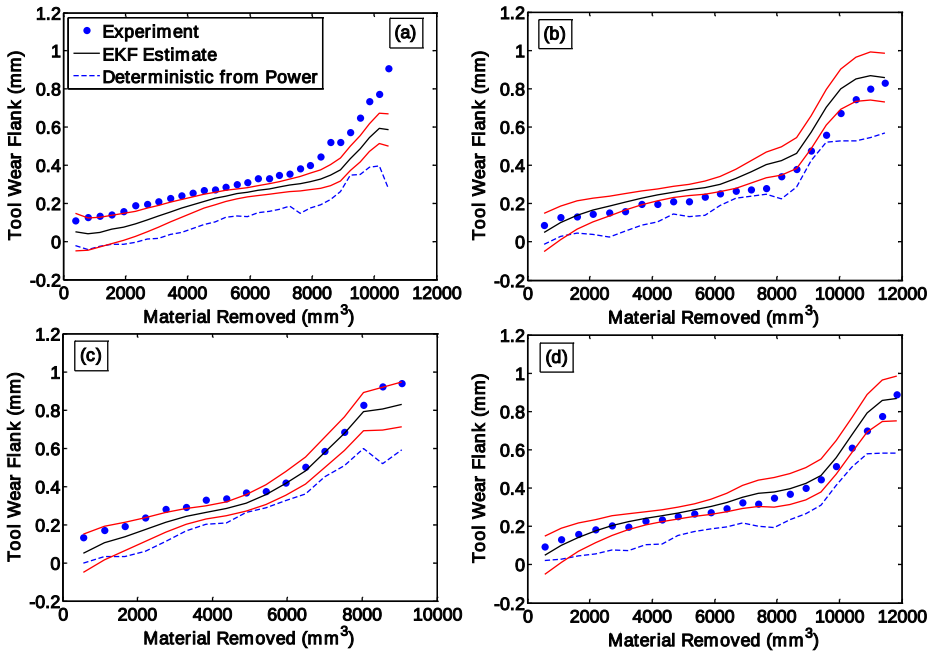

Figure 5-10: Estimated tool wear width for feed 0.05 mm/rev, (a) Replication 1, (b) Replication 2, (c) Replication 3 and (d) Replication 4

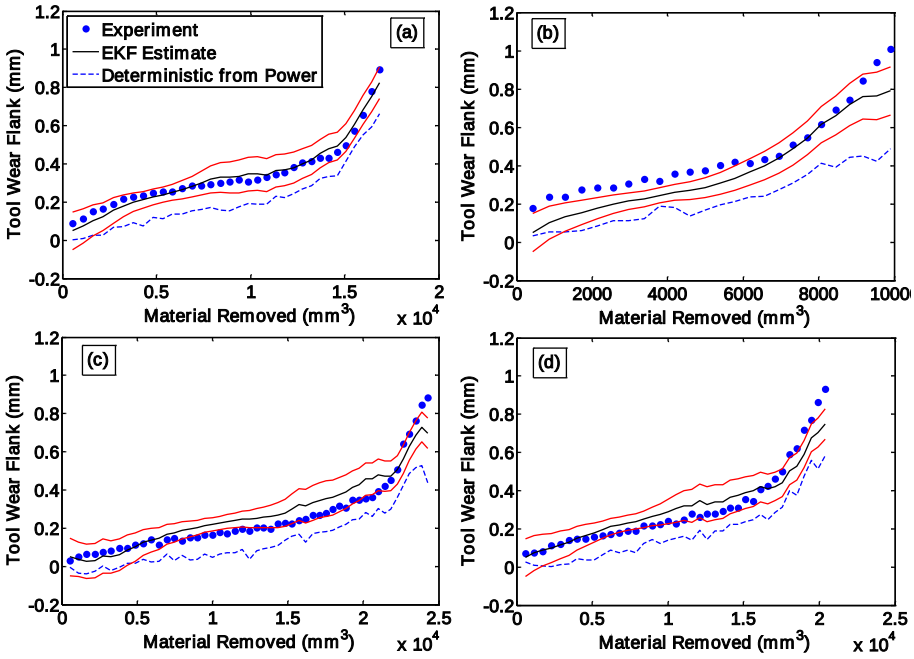

Figure 5-11: Estimated tool wear width for feed 0.10 mm/rev, (a) Replication 1, (b) Replication 2, (c) Replication 3 and (d) Replication 4

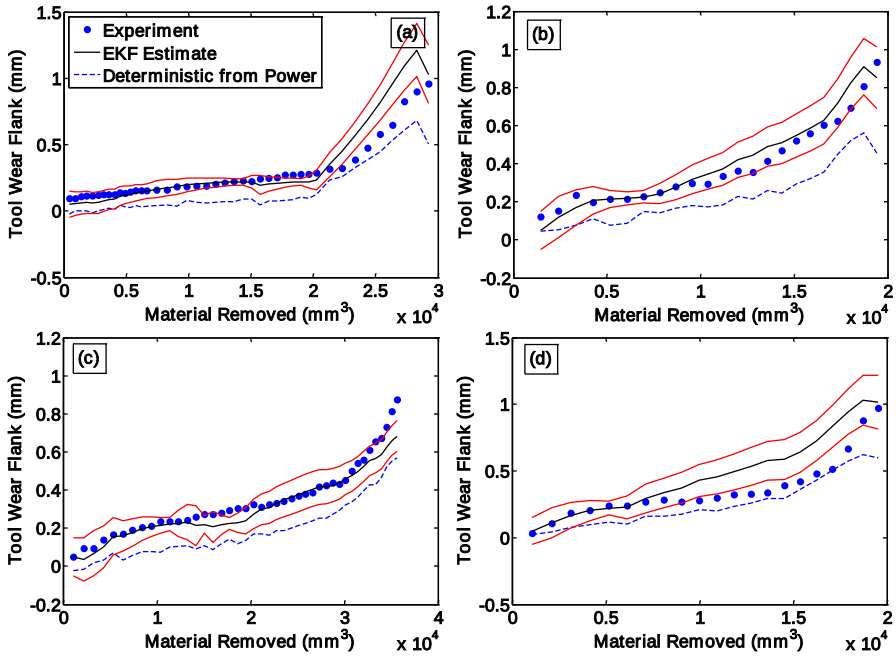

Figure 5-12: Estimated tool wear width for feed 0.15 mm/rev, (a) Replication 1, (b) Replication 2, (c) Replication 3 and (d) Replication 4

According to the Figure 5-10, in the 1st replication, the EKF was able to estimate the tool wear width only up to 300 µm, and had poor estimation after that. This is due to the effect of measured power, which reduced abruptly as shown in Figure 5-2. For the feed 0.1 and 0.15mm/rev, the EKF performed well except for the 4th replication of feed 0.15mm/rev. This is due to the large variations that exist in experimental replications which make the state model less accurate. In the other replications almost all of the experimental measurement fell in the 95% prediction interval of the filter.

To better assess the performance of the EKF, validation sets were used for estimating the progressive tool flank wear width. Figure 5-13 through Figure 5-16 show the results of the estimation. To have a closer look at the performance of the EKF in predicting tool wear and tool wear rate, the trajectory function (*i.e.* tool wear rate versus tool wear) and

the progressive tool wear function are shown side by side. As can be seen in these figures, the EKF is able to have an accurate estimation for the tool wear width with less than 0.07 mm^2 RMSE, however there is still inaccuracy in estimating of the tool wear rate specifically after reaching 0.6 mm. To emphasis on significance of stochastic filter in improving estimation accuracy the RMSE and Mean Absolute Error (MAE) of the estimated tool wear are compared in Figure 5-17 for all the 4 tests with a deterministic estimation which only uses the power-tool wear width relation shown in Equation 5-21 (without additive noise v_k). It can be seen from this figure that the EKF estimation outperformed the deterministic method in by 65%, 73%, 65% and 68% improvements in RMSE values which are significant in estimation results.

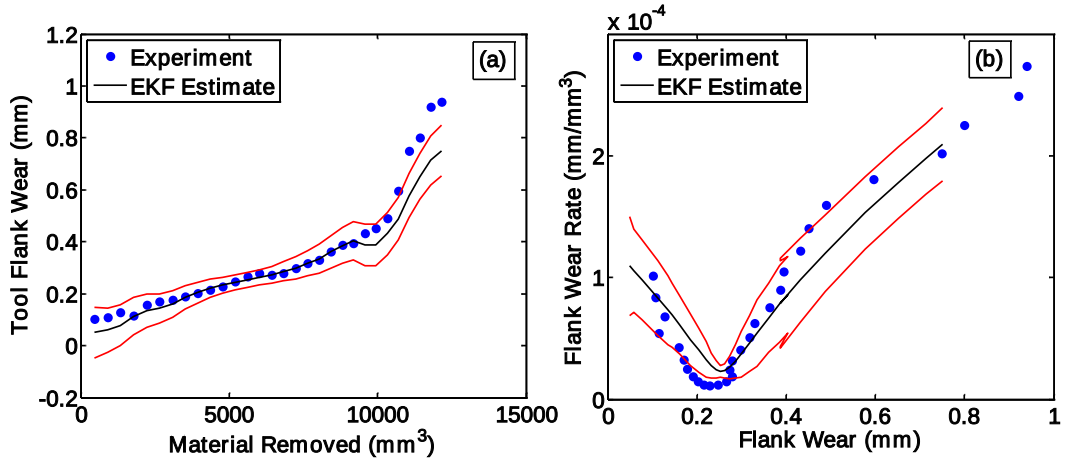

Figure 5-13: Estimated tool wear and tool wear rate for feed 0.0625 mm/rev, (a) estimated tool wear and (b) trajectory estimation

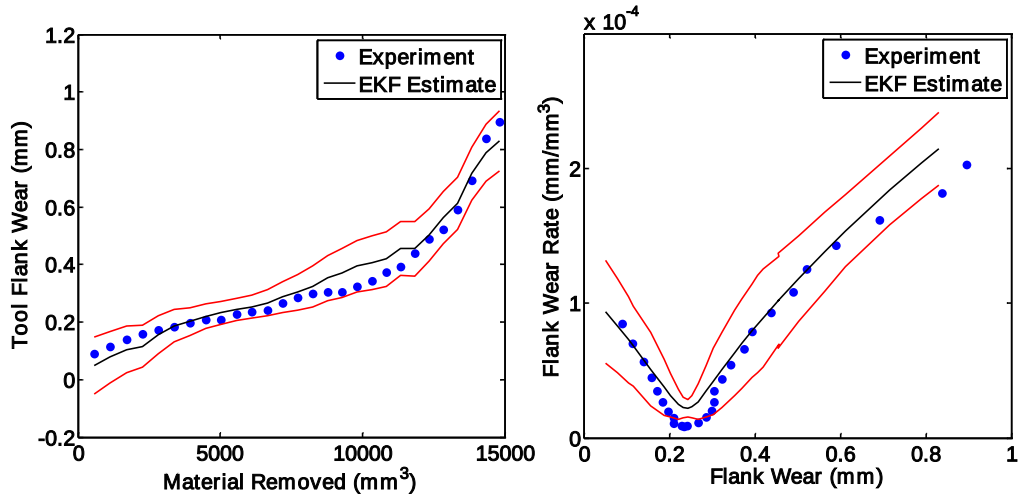

Figure 5-14: Estimated tool wear and tool wear rate for feed 0.0875 mm/rev, (a) estimated tool wear and (b) trajectory estimation

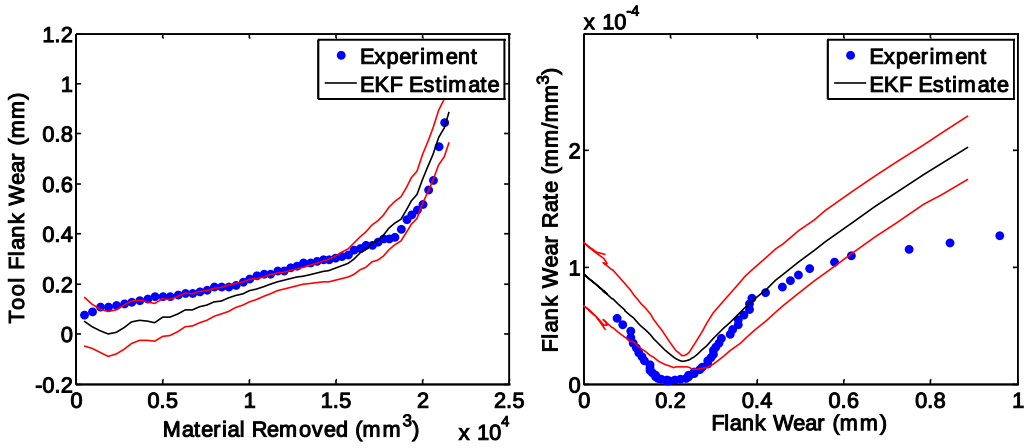

Figure 5-15: Estimated tool wear and tool wear rate for feed 0.1125 mm/rev, (a) estimated tool wear and (b) trajectory estimation

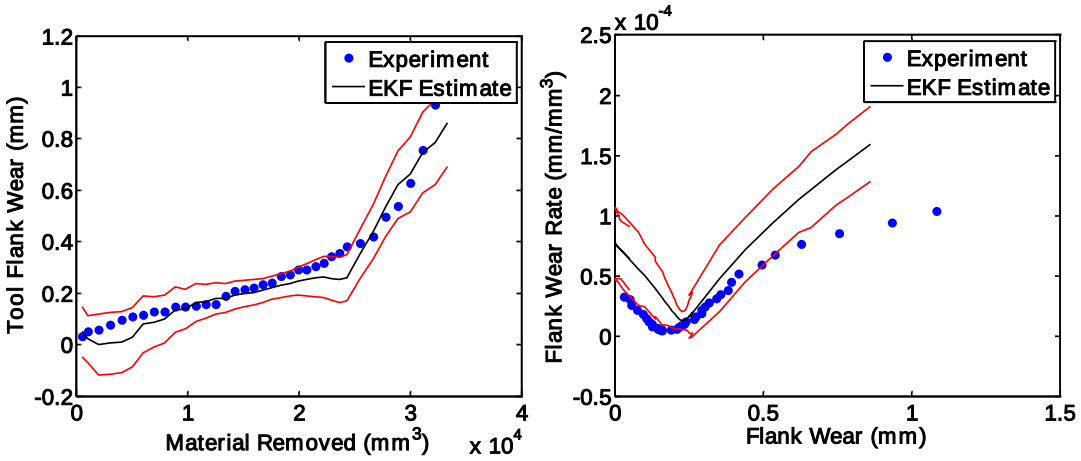

Figure 5-16: Estimated tool wear and tool wear rate for feed 0.1375 mm/rev, (a) estimated tool wear and (b) trajectory estimation

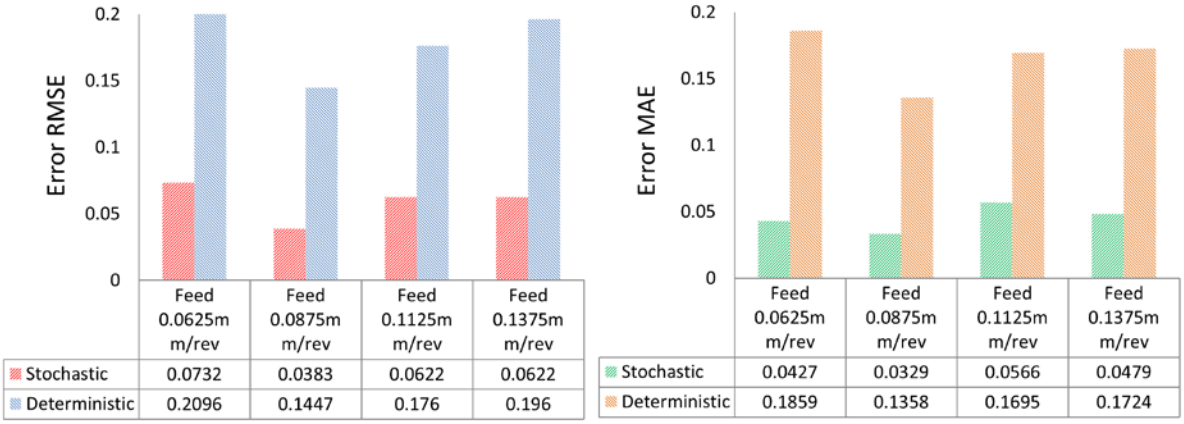

	Feed 0.0625m m/rev	Feed 0.0875m m/rev	Feed 0.1125m m/rev	Feed 0.1375m m/rev
Stochastic	0.0732	0.0383	0.0622	0.0622
Deterministic	0.2096	0.1447	0.176	0.196

	Feed 0.0625m m/rev	Feed 0.0875m m/rev	Feed 0.1125m m/rev	Feed 0.1375m m/rev
Stochastic	0.0427	0.0329	0.0566	0.0479
Deterministic	0.1859	0.1358	0.1695	0.1724

Figure 5-17: Comparison of error between stochastic and deterministic methods in the estimated tool wear

Effects of Tool Wear on Surface Integrity (Workpiece Health) of IN718

As explained in Chapter 1, it was assumed that the quality of the workpiece can be represented by three parameters: dimensional integrity, surface quality, and surface/subsurface damage. In this work, dimensional integrity of the workpiece is represented by diameter deviation from the target diameter. Therefore, the diameter of the

IN718 bar was measured three times after each pass, using a Mititoyo caliper with ±0.025mm accuracy. The arithmetic average of the workpiece surface roughness (R_a) was selected to represent quality of the surface. A Mahr surface profilometer was used to measure roughness (with a sweeping range of 5.6mm) at three different workpiece locations. Lastly, the surface/subsurface damage to the workpiece was represented by residual stress. The residual stress was measured only in the cutting direction (*i.e.*, hoop stress) for six different cutting conditions. A first series of measurements was made with a sharp insert in three different feeds; 0.05, 0.1 and 0.15 mm/rev. The second series of measurements was made with a worn tool; 300, 600 and 900µm of flank wear width only in the feed of 0.1 mm/rev. As mentioned before, all the experiments were carried out in wet-cutting with flood lubrication condition.

Effects of Wear and Wear Rate on Dimensional Integrity of the Workpiece

Evolution of flank wear during the process causes gradual changes in the geometry of the tool. With an increase in the flank wear width, the height of the tool will be reduced and consequently dimensional deviation in the workpiece from the target dimension occurs. Considering the schematic of a simple cutting tool shown in Figure 5-18(a), it is possible to estimate the dimensional deviation with an accurate estimation of the flank wear width and using the exact tool geometry shown in Figure 5-18(b). The geometrical relationship was derived based on the configuration setup of the insert with -6^o rake angle and $+6^o$ clearance angle and 0.4mm of Tool Nose Radius (TNR). The large TNR produces a curve at the tip of the tool which was linearized with three regions according to Figure 5-18(b). The first region correlates dimensional deviation to maximum of

200µm of the flank wear, the second region correlates dimensional deviation to maximum of 500µm of the flank wear and the third region correlates dimensional deviation to 900µm of the flank wear. The geometrical relationship for each region is shown in Equation 5-28, where Δd is the dimensional deviation, and VB is the flank wear width. It has been shown in this chapter that by using the stochastic-based Extended Kalman Filter (EKF), an accurate estimation of flank wear probability density becomes possible; therefore diameter deviation can be found using Equation 5-28 and the estimated probability density of the flank wear (VB).

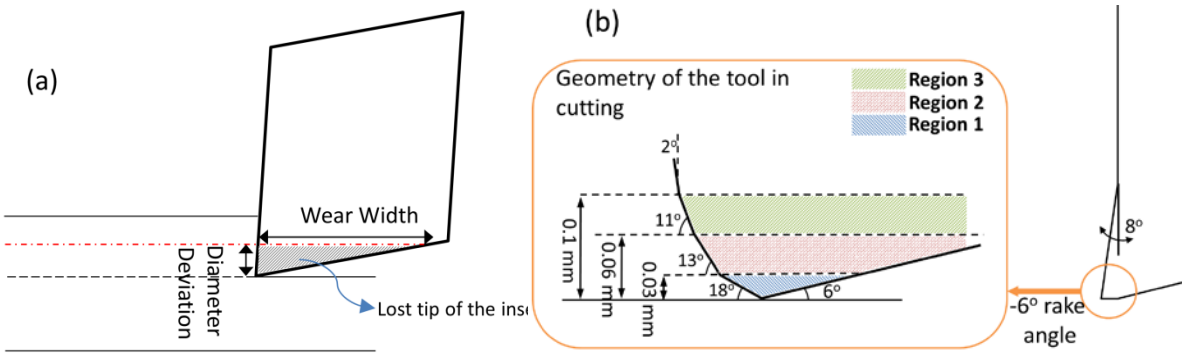

Figure 5-18: Effect of wear on diameter deviation, (a) schematic of simple cutting tool and (b) detailed geometry of Sandvik CNGG insert, three regions represents three different geometrical relation.

$$\Delta d = \begin{cases} \dfrac{2VB}{\tan(18^\circ)+\cot(6^\circ)} & 0 < VB < 0.223 \\ \dfrac{2VB - 0.06\left[\tan(18^\circ)-\tan(13^\circ)\right]}{\tan(13^\circ)+\cot(6^\circ)} & 0.223 < VB < 0.5 \\ \dfrac{2VB - 0.06\left[\tan(13^\circ)+\tan(18^\circ)\right]+0.12\tan(11^\circ)}{\tan(11^\circ)+\cot(6^\circ)} & 0.515 < VB < 0.9 \end{cases} \quad 5\text{-}28$$

Stochastic Tools for Diameter Deviation Classification

Extended Kalman Filter for Classification

The diameter deviation results from the experimental measurement for all the seven feeds are shown in Figure 5-19. As shown in this figure, the diameter deviation has an increasing trend with maximum of 0.2mm when the flank wear reaches 900µm, however large variability in the replications and therefore poor repeatability is observed. Reduction in the diameter of the workpiece and consequently undesired vibration due to stiffness change, in addition to the generation of different wear failure modes such as chipping or build up edge on each replication are the main sources of the poor repeatability of the data.

To emphasize the practical applications of the method, it was decided to categorize the deviation from the target diameter into three distinct classes. The first class represents the deviations below 0.05 mm which is labeled as “acceptable”, the second class represents the deviation between 0.05 to 0.15 mm which indicates that “re-work” is required for the workpiece and the third class represents deviation above 0.15 mm which indicates the requirement for “major rework with inspection”.

The probability density function of the flank wear (which is assumed to be a normal distribution function based on the Kalman filter theory) can be estimated after each pass using the EKF method described before. Since the flank wear distribution is considered as a Gaussian function, its mean and standard deviation can be simply plugged into Equation 5-28 to find the estimated probability distribution of the diameter deviation.

Lastly, the probability of the each class can be calculated and the maximum value represents the classification results. This process is shown in Figure 5-20.

Naïve Bayes for Classification

To be able to compare the classification performance of the EKF-based method, it is worthy to compare it with other techniques. The naïve Bayes method is a simple yet efficient probabilistic-based algorithm based on Bayes theorem for classification purposes. In this method an initial belief of each class is combined with a likelihood function of model features; this determines the decision probability of each class. Equations 5-29 and 5-30 describe the classification strategy based on the naïve Bayes, where C_i represents a class with i={1, 2, 3} and $\boldsymbol{X}$ represent the selected features. Five features were selected as the estimated results of flank wear (VB), and flank wear uncertainties (σ_{VB}), the estimated results of flank wear rate (VB_r) and its corresponding uncertainties (σ_{VBr}) from the EKF method and direct measurement of spindle power (P) from the Hall effect sensor (see Figure 5-1).

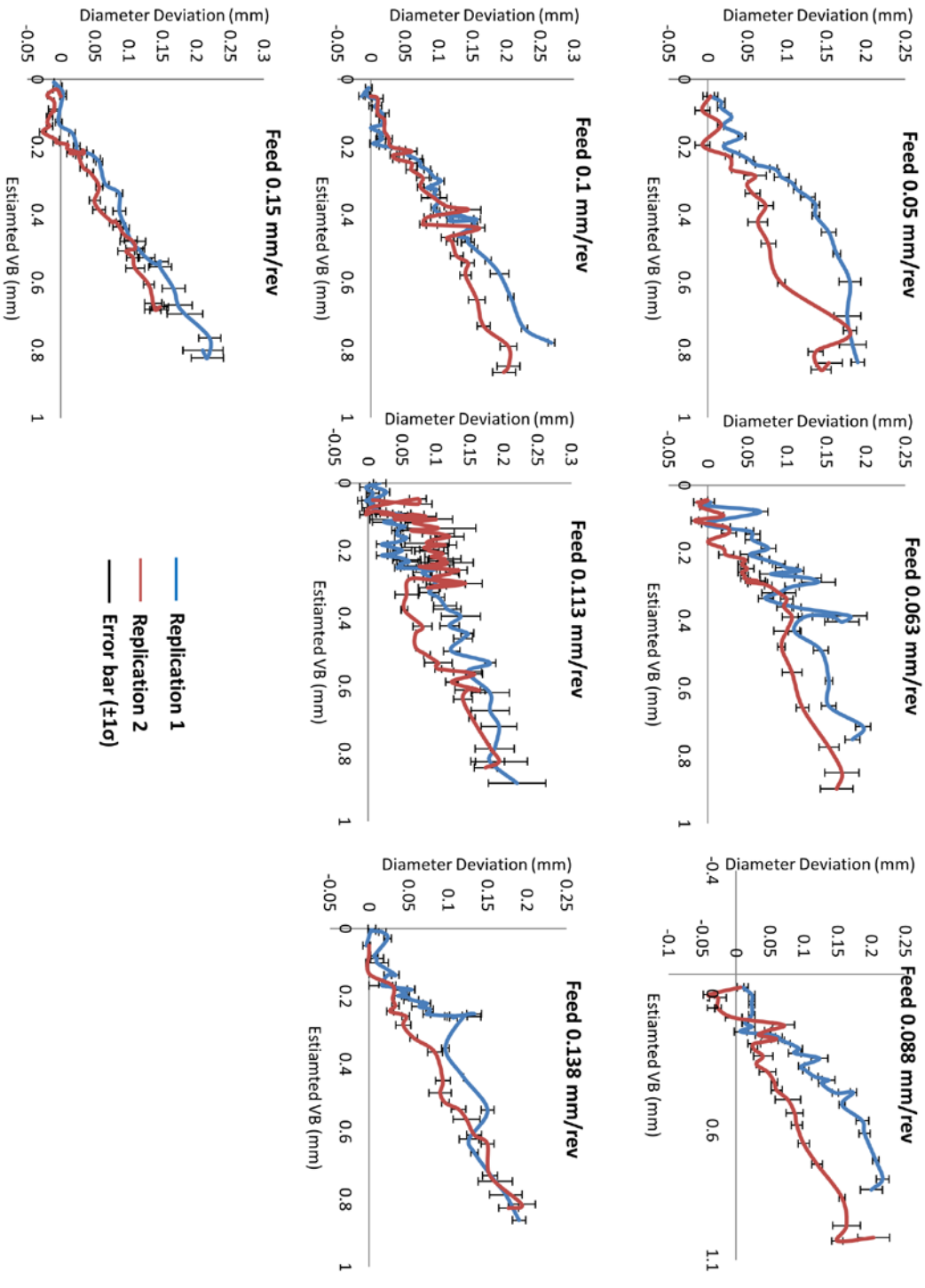

Figure 5-19: Diameter deviation in seven different feeds

To be able to evaluate the performance of the naïve Bayes classifier, out of 14 sets of experiments; 9 sets were selected for training and 5 sets for testing. The likelihood function Pr($\boldsymbol{X}|C_i$) was assumed as Normal distribution function with mean and standard deviation derived from the training sets. An equal initial belief probability Pr(C_i) of 1/3 was assumed for three classes.

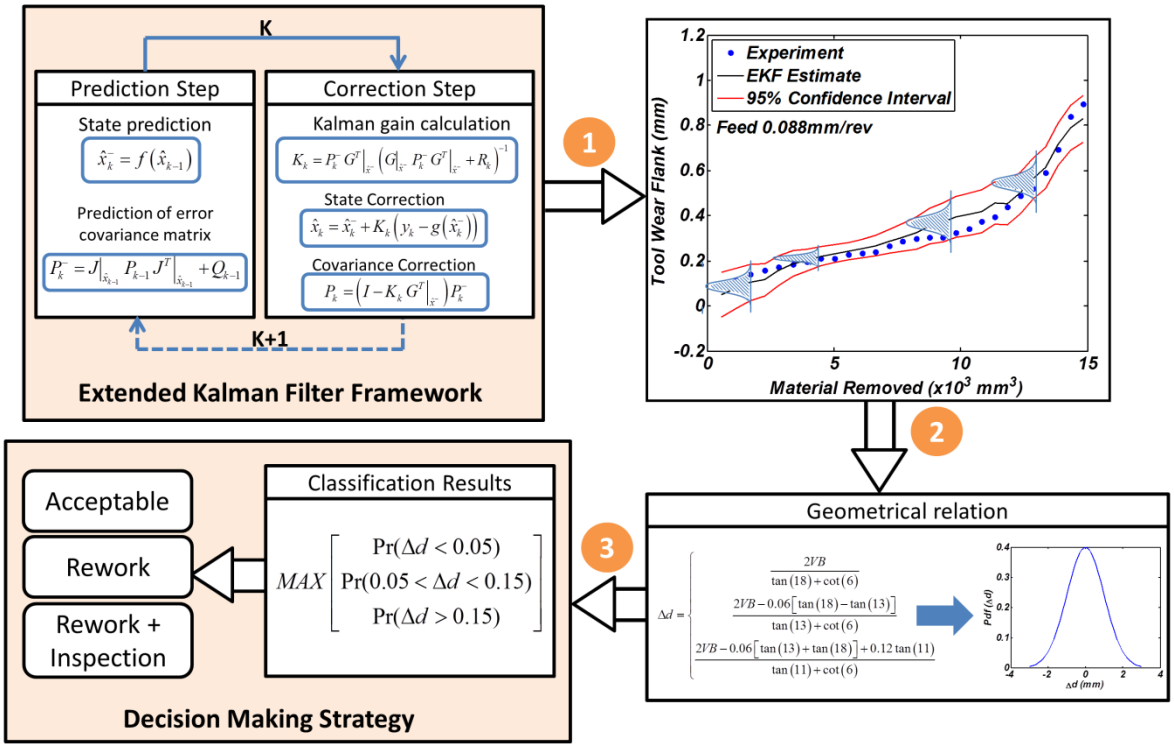

Figure 5-20: Estimation of the flank wear probability density with EKF and the relation to diameter deviation with classification strategy

$$\Pr\left(C_i \mid X\right) \propto \Pr\left(X \mid C_i\right)\Pr\left(C_i\right) \;\rightarrow\; \Pr\left(C_i \mid VB, \sigma_{VB}, VB_r, \sigma_{VB_r}, P\right) \propto \frac{\Pr\left(VB, \sigma_{VB}, VB_r, \sigma_{VB_r}, P \mid C_i\right)}{3} \tag{5-29}$$

$$\text{Selected Class} = \arg\max\left[\Pr\left(C_i \mid X\right)\right] \tag{5-30}$$

Deterministic Tools for Diameter Deviation Classification

Support Vector Machine (SVM)

It has been shown by several researchers that the SVM method performs well in tool wear classification purposes [105-107]. The underlying assumptions in using the SVM is finding the optimal hyperplane using selected feature vectors called support vectors that maximizes the safety margin $2/\|\boldsymbol{w}\|^2$, where $\boldsymbol{w}$ is the normal vector to the hyperplane. The optimal hyperplane with maximum safety margin can be found by solving the quadratic optimization problem as in Equation 5-31, where y_i is +1 if the feature vector x_i belongs to the first class and -1 if the x_i belongs to the second class, b is a constant and m is the number of feature vectors in the training set. To solve this optimization problem, a Lagrangian multiplier with two constraints as shown in Equation 5-32 should be solved. To be able to tackle the nonlinearity of the data, kernel transformation manipulations have been suggested to map the data into the higher dimensional space and make it linearly separable [108]. Both linear and Radial Basis Function (RBF) kernels were used for classification. However, no significant improvement in the classification results obtained in using RBF kernel as compared to the linear one. Therefore the latter was selected. Since the SVM method is generally being used for 2-class problems, a pair by pair comparison was done and the class with the maximum votes was selected as a result. The same five feature vectors namely VB, σ_{VB}, VB_r, σ_{VBr} and P were selected on the same training and testing sets as naïve Bayes.

$$\min \left[\frac{\| w \|^2}{2} \right] \qquad \text{5-31}$$
$$y_i (w^T x_i + b) \geq 1 , \quad i = 1, ..., m$$

$$L(w, b, \alpha) = \frac{1}{2} \| w \|^2 - \sum_{i=1}^{m} \alpha_i \left[y_i (w^T x_i + b) - 1 \right]$$
$$Condition \begin{cases} w = \sum_{i=1}^{m} \alpha_i y_i x_i \\ \sum_{i=1}^{m} \alpha_i y_i = 0 \end{cases} \qquad \text{5-32}$$

Classification Results and Discussion

To be able to compare the performance of each method, the misclassification rate of each set of data for both training (9 sets with total of 283 data points) and testing sets (5 sets with total of 195 points) are compared in Figure 5-21 and Figure 5-22. It can be seen from these figures that The EKF-based method outperforms the naïve Bayes and the SVM in the first and third classes, "acceptable" and "major rework with inspection" respectively. However, the EKF has a very poor performance in the second class ("rework") and was outperformed by the naïve Bayes method. Moreover, large errors were observed in some of the testing/training sets (*e.g.* large misclassification error of naïve Bayes algorithm for third class of testing set 12. This is due to the poor repeatability and high noise contamination of the data, which is clear from the Figure 5-19. Therefore, it is concluded that large variance in the dataset lowers the classification rate. The total misclassification error is compared for all the classes in training and testing sets in Table 5.4. Note that just relying on Table 5.4 for selecting the best method can be misleading since according to this table naïve Bayes has the highest

error (34%) while according to Figure 5-22, it has the best performance (the lowest error) in labeling “rework” class. Hence, Figure 5-22 together with Table 5.4 should be used for selecting the optimal method. In this case, the EKF for classifying 1st and 3rd classes and the naïve Bayes for classifying 2nd class is the best solution.

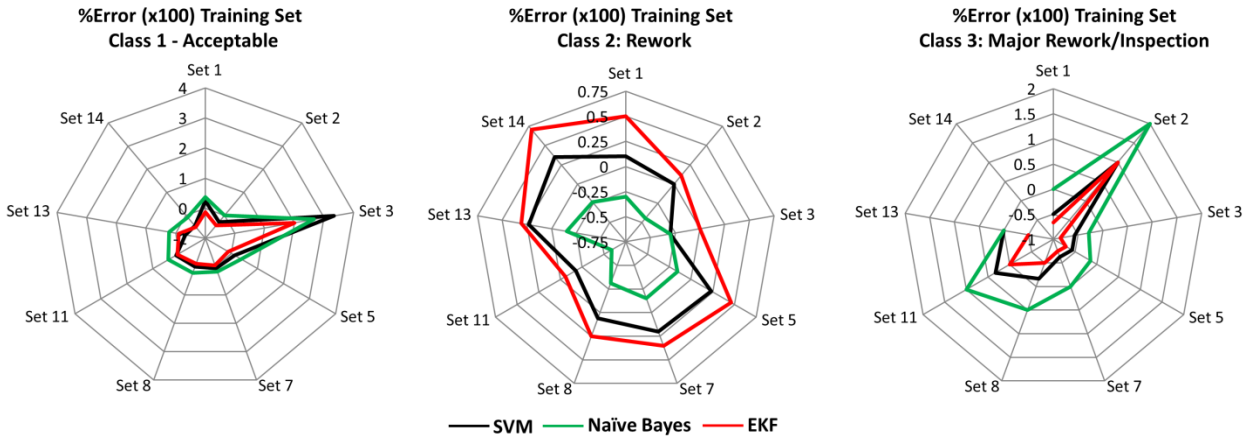

Figure 5-21: Error comparison in training set of the EKF, naïve Bayes and SVM for diameter deviation classification

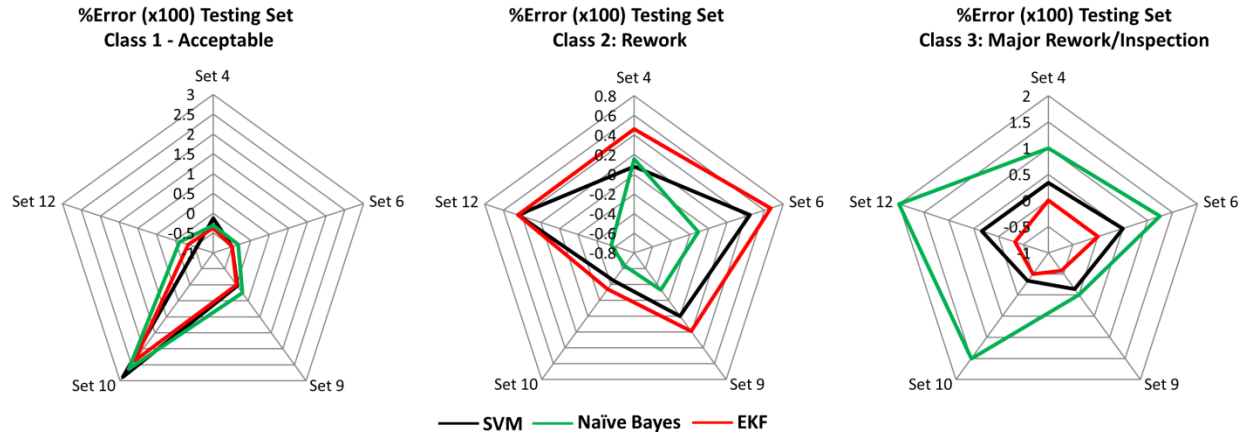

Figure 5-22: Error comparison in testing set of the EKF, naïve Bayes and SVM for diameter deviation classification

The other factor that should be noted is the extra advantage of statistical-based methods (*i.e.*, naïve Bayes and EKF) in providing additional information in the form of

the probability of being in each class which can be later incorporated into a risk function to determine the risk of misclassification as well. The deterministic method (*i.e.*, SVM) is not able to give any information on this probability.

Table 5.4: Misclassification rate of SVM, naïve Bayes and EKF methods

Misclassification Rate [%]	Support Vector Machine	Naïve Bayes	Extended Kalman Filter
Method	Deterministic	Probabilistic	Probabilistic
Training Set	20.8%	20.8%	26.8%
Testing Set	27.7%	34.4%	28.7%

Effects of Wear on Surface Quality

As discussed above, the quality of the machined surface as one of the workpiece health factors can be described by the average surface roughness (R_a). Considering Figure 5-23 which describes the relation between estimated flank wear (*VB*) and measured surface roughness in various feeds reveals an interesting finding that there exists extremely poor, almost nonexistent repeatability between the same tests. To further investigate the effect of wear on the surface roughness, Analysis of Variance (ANOVA) was deployed. The estimated wear values were converted into categorical format by dividing them into four equi-distant regions between 0 to 900µm where each region represents a unique state of wear. The ANOVA test results in Table 5.5 with more than 0.05 *p*-value show that the wear state is not a significant factor on surface quality, which is in agreement with the poor repeatability results of Figure 5-23. This conclusion is extremely important since a general belief in many research articles is on detrimental effect of wear on surface roughness. However, as can be seen from Figure 5-23, on

occasions with more than 600μm of flank wear; surface roughness still remains below 0.8μm.

An unanswered question here is what the underlying cause(s) for such a large variations/uncertainties are in surface roughness. Three factors could cause the poor repeatability in surface roughness data. First is the change in diameter of the IN718 bar from one test to another. Reduction in diameter which changes the stiffness of the workpiece can cause undesired vibration during each cut and therefore affect the surface roughness profile. One way to avoid this is by using several workpieces with the same diameter, which in practice is extremely costly. Second is the formation of continuous chip and entanglement around the workpiece; which can cause abrupt changes in surface roughness due to the rubbing of chip on the surface of the workpiece. This phenomenon has been captured by high speed camera and demonstrated as Figure 5-24. One way to avoid this is increasing the depth of cut in order to break the chip. However, due to the high strength of nickel-based alloys, this could accelerate tool wear rate and cause early tool failure. Third is an internal variation in the combination of workpiece and tool as a dynamic system which causes variation in the output, *e.g.*, surface roughness. Therefore to be able to quantify the effect of wear on surface roughness, a very large number of replications would be required.

Table 5.5: ANOVA table with 0.51 *p*-value (rejecting null hypothesis)

Source of Variation	Sums of Square	Degrees of freedom	Mean Square	*F*-value	*p*-value	$F_{critical}$
Between Groups	0.95	3	0.32	0.76	0.51	2.6
Within Groups	196.4	472	0.42			
Total	197.3	475				

Effect of Wear on Surface and Subsurface Damage

Depth of Machining Affected Zone

The depth of Machining Affected Zone (MAZ) was calculated using the etched samples of IN718 bar under four different wear conditions as shown in Figure 5-25. The results are interesting since the MAZ while cutting with flank wear of 600μm has the highest impact on the microstructure alteration beneath the surface. While smaller depth was observed in larger flank wear width.

Chip Formation Model

The surface and subsurface damage can be quantified with the residual stress remained on/beneath the surface after cutting process. A Finite Element (FE) model with Lagrangian approach developed using ABAQUS/Explicit 6.14 and the results of the FE model were compared with experimental results measured with X-ray diffraction in the cutting direction. To be able to accurately predict residual stress due to mechanical and thermal loads, a coupled thermal-displacement simulation using C3D8RT elements with total simulation time of 1 millisecond was used. The exact geometry of the tip of the cutting insert and workpiece was modeled in 3-D space as shown in Figure 5-26(a). The minimum length of elements at the cutting zone was chosen to be 10μm and the

maximum length was chosen as 36μm away from the cutting zone for a total of 219,776 elements. To investigate the effect of flank wear on residual stress, the geometry of the tool was updated before the simulation. The geometry of flank wear as shown in Figure 5-26(b) was found by intersecting a XY-plane with the bottom of the tool. It shows a very close relationship with the actual shape of the tool wear from the experimental results as demonstrated as in Figure 5-26(c). However, the chipping effect of the tool edge cannot be accurately modeled with this method. To accelerate the simulation, the tool was considered as a rigid shell with 1,500 triangular elements of R3D3 type with tool edge of 10μm. Also, the wear land clearance angle in the worn tool was considered to be 0^o in contrast to $+6^o$ of clearance angle for the sharp tool as shown in Figure 5-26(c).

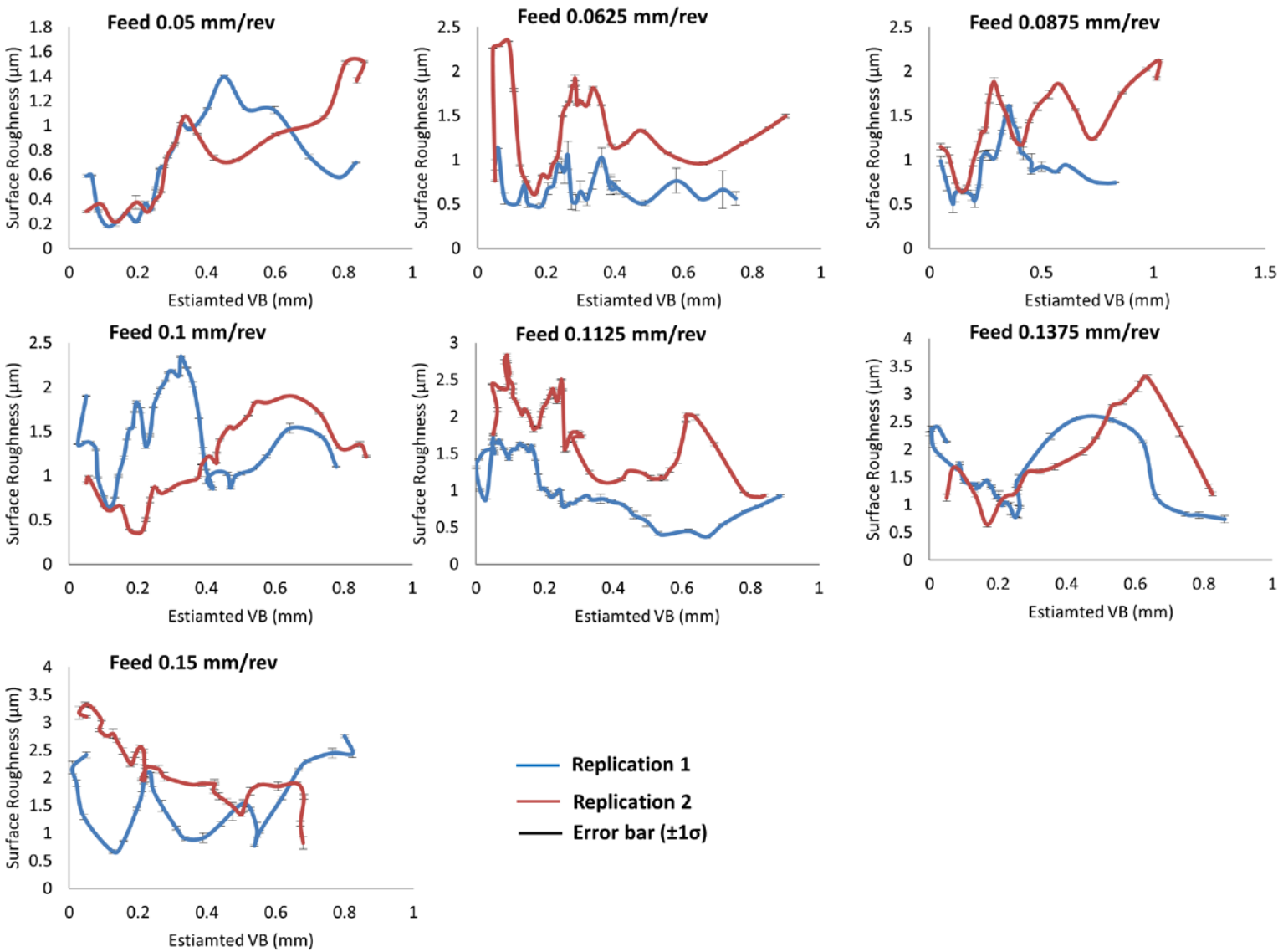
Feed 0.05 mm/rev
Feed 0.0625 mm/rev
Feed 0.0875 mm/rev
Feed 0.1 mm/rev
Feed 0.1125 mm/rev
Feed 0.1375 mm/rev
Feed 0.15 mm/rev
Surface Roughness (µm)
Estiamted VB (mm)
Replication 1
Replication 2
Error bar (±1σ)

Figure 5-23: Surface roughness change with respect to estimated flank wear in different feeds

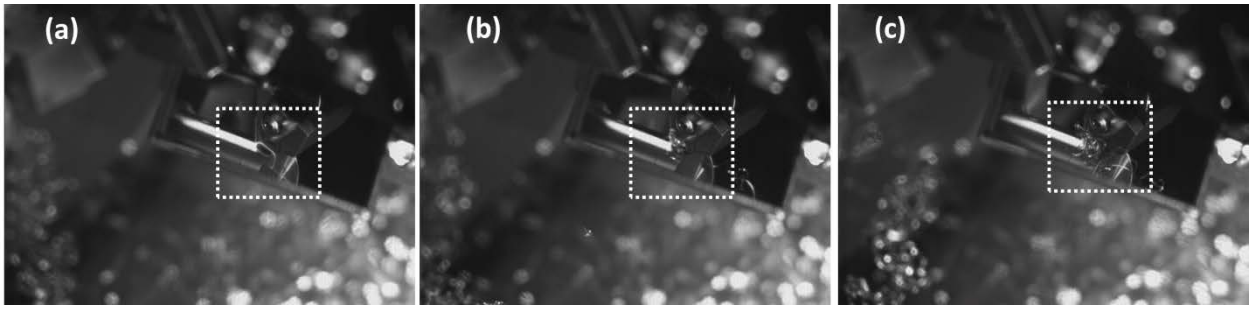

Figure 5-24: Chip entanglement and damage to the surface roughness, (a) chip is exiting with no entanglement, (b) chip start to trap in the clearance zone between tool and workpiece, and (c) full entanglement with workpiece/chip rubbing against each other

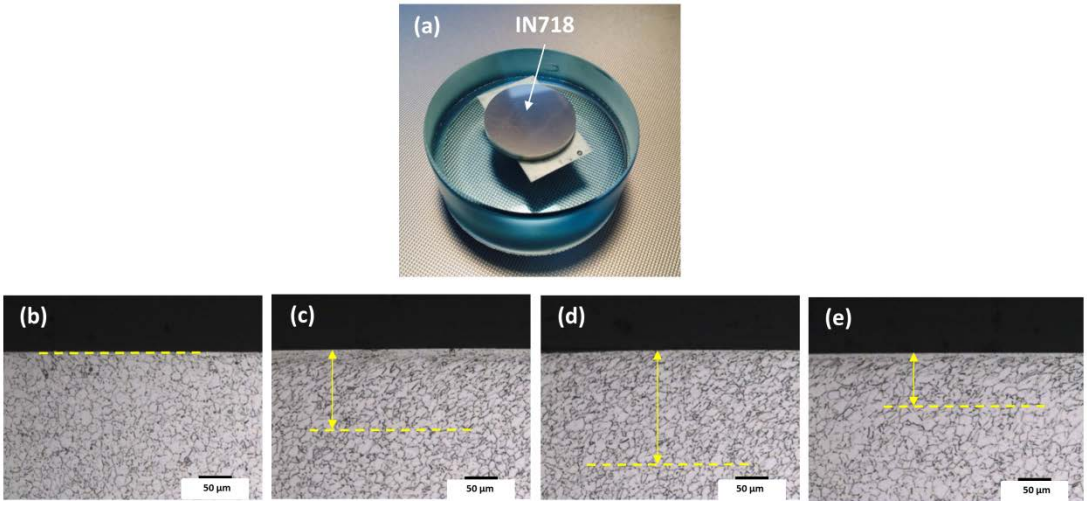

Figure 5-25: Machining affected zone in different wear state and feed 0.1 mm/rev, (a) etched IN718 sample, (b) 0 mm depth of MAZ with Sharp tool, (c) 0.12mm depth of MAZ with 300µm flank wear width, (d) 0.2mm depth of MAZ with 600µm flank wear width and (e) 0.085mm depth of MAZ with 900µm flank wear width

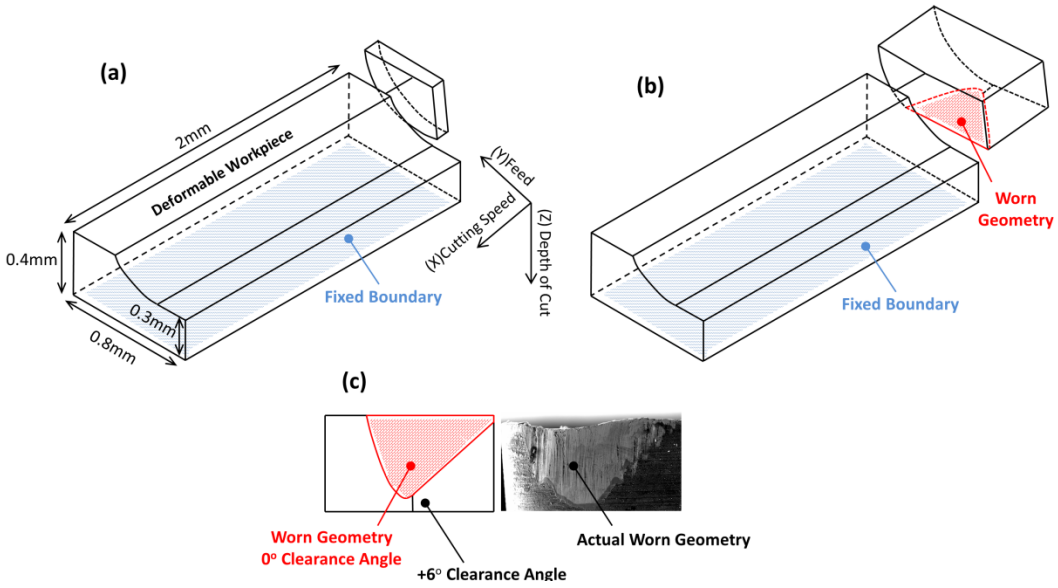

Figure 5-26: 3-D chip formation model, (a) workpiece dimension with sharp tool model, clearance angle +6°, (b) updated geometry of the tool with 0° clearance angle at wear land and (c) comparison of actual wear land and the model of worn tool in XY-plane

Material Plasticity and Damage Model

To model the visco-plastic behavior of IN718, the Johnson-Cook (J-C) constitutive plasticity model as in Equation 5-33 was selected, where $\bar{\sigma}$ is the equivalent plastic stress, $\bar{\varepsilon}$ is the equivalent plastic strain, $\dot{\bar{\varepsilon}}$ is the equivalent plastic strain rate, $\dot{\bar{\varepsilon}}_0$ is the reference plastic strain, T is the temperature, T_m is the melting temperature, T_0 is the room temperature, A is the yield stress, and B, c, n and m are the material-dependent J-C model constants. There are several research articles published on finding the J-C model constants for IN718, however the majority of the reports are given to age-hardened IN718 [109-111]. Byun and Farrell compared the tensile properties of a precipitation-hardened alloy with a solution-annealed one and found the parameter n=0.9 and a range of 500-1100 MPa for the parameter B [112]. Their results were in agreement with the work of

Pereira and Lerch whom found the parameter A=317MPa and C=0.0312 as well [113]. At the time writing this dissertation, the author could not find any published articles on the temperatures softening exponent (m) of annealed IN718 therefore the value of m was considered equal to 1.3 based on the age-hardened IN718 property [111]. The material properties and J-C model parameters are summarized in Table 5.6 and Table 5.7. To be able to model the large deformation and rapid strain rate in chip formation, a damage model using the element deletion method is required. Therefore the damage initiation criteria were selected as shear damage with maximum shear of 2. The deletion process of the elements starts when the shear strain reaches 2, and the element will be deleted completely when the maximum degradation reaches unity.

$$\bar{\sigma} = \left(A + B\bar{\varepsilon}^{n}\right)\left(1 + C\ln\left(\frac{\dot{\bar{\varepsilon}}}{\dot{\bar{\varepsilon}}_0}\right)\right)\left(1 - \left(\frac{T - T_0}{T_m - T_0}\right)^{m}\right) \qquad 5\text{-}33$$

Table 5.6: Material properties parameters for annealed IN718

Material properties	Density [ρ]	Modules of elasticity [E]	Poisson Ratio [ν]	Conductivity [κ]	Specific heat [c]	Expansion Coeff. [α]
Unit	kg/m^3	GPa	-	W/mK	J/kg^{o}C	µm/m^{o}C
Value	8810	200	0.3	11	435	13

Table 5.7: Johnson-Cook model parameters for annealed IN718

J-C constant	$A(=\sigma_y)$	B	T_m	T_0	$\dot{\bar{\varepsilon}}_0$	n	C	m
Unit	MPa	MPa	^{o}C	^{o}C	s^{-1}	-	-	-
Value	317	800	1270	20	1	0.9	0.0312	1.3

Friction Model

It was assumed that the coefficient of friction in wet cutting remains constant (=0.1) in 1 msec of simulation. The sticking condition of the Coulomb friction law was defined based on maximum shear stress between the contacting surfaces equal to 187MPa ($=\sigma_y/\sqrt{3}$). After the shear stress between the contacting surfaces exceeds this value, slipping occurs. Moreover, element-based contact was defined to be able to establish contact condition for the internal surfaces contacting the tool when element deletion occurs. It was assumed that the 100% of heat generation due contact turns into the heat and 50% of this heat distributes into the workpiece.

In wet cutting, a large portion of the generated heat will be taken away from the tool and workpiece by the flow of the coolant. Since modeling the effect of coolant was not in the scope of this work, the thermal dissipation and the behavior of coolant was modeled as a convection heat transfer condition with convection coefficient of coolant as 3000 W/m^2K.

Residual Stress Prediction and Experimental Validation

To validate the FE model for residual stress prediction, first the results for the sharp tool shown in Figure 5-26(a) in three different feeds (0.05, 0.1 and 0.15 mm/rev) were compared to experimental results in the cutting direction, *i.e.*, X-direction in Figure 5-26(a). As shown in Figure 5-27, the prediction of the residual stress has a very good match with the experimental results which shows the validity of the FE model.

In the next step, the FE model with the worn tool was compared with the experimental results in Figure 5-28 for the feed of 0.1 mm/rev and 300, 600 and 900 µm

of flank wear width. It is clear from Figure 5-28 that the FE model can predict the tensile stress at the surface with relatively good accuracy. However, Figure 5-28 shows inaccuracy in predicting the compressive stress that remains below the surface up to 0.3 mm depth.

Several factors can be attributed to this error, such as assuming a constant friction coefficient, simplifying the coolant effect with a convection heat transfer problem and inaccuracy of the worn tool geometry. However, the major limitation in modeling the effect of the worn tool on residual stress is the effect of element deletion. In general, element deletion makes modeling chip formation and excessive distorted elements in high strain simulations such as machining possible. However, the deleted elements cause a sudden reduction in contact area which misleadingly appears as a fluctuation of cutting force. As shown in Figure 5-29, this is not a major issue while cutting with sharp insert, since the deleted elements at the tool rake face and chip (region 1 of Figure 5-29) will be replaced rapidly by new elements (region 2). However, in modeling worn tool with a 0° clearance angle wear land that comes into contact with the workpiece, the deleted elements on the surface of the workpiece as in region 3 of Figure 5-29 cannot be easily replaced by any other elements. Therefore a general loss of contact at region 4 occurs. The main reason behind the consistent compressive stress beneath the surface of the workpiece is the plowing frictional effect between the wear land and cutting surface which is dependent on contact pressure of the two surfaces. Therefore using the element deletion method puts a limitation in modeling the plowing effect, which eventually appears as error in predicting compressive residual stresses. To better compare the

formation of chips in the presence of wear, the FE model results under four conditions are shown in Figure 5-30.

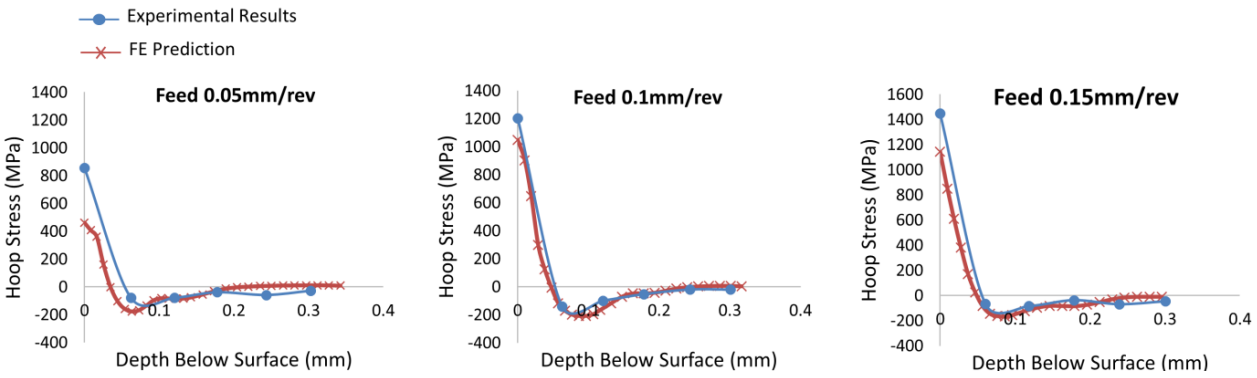

Figure 5-27: Comparison of residual of experiment and FE prediction in 3 different feeds, cutting speed (=80m/min) and depth of cut (=0.1mm) are constants – sharp tool was used

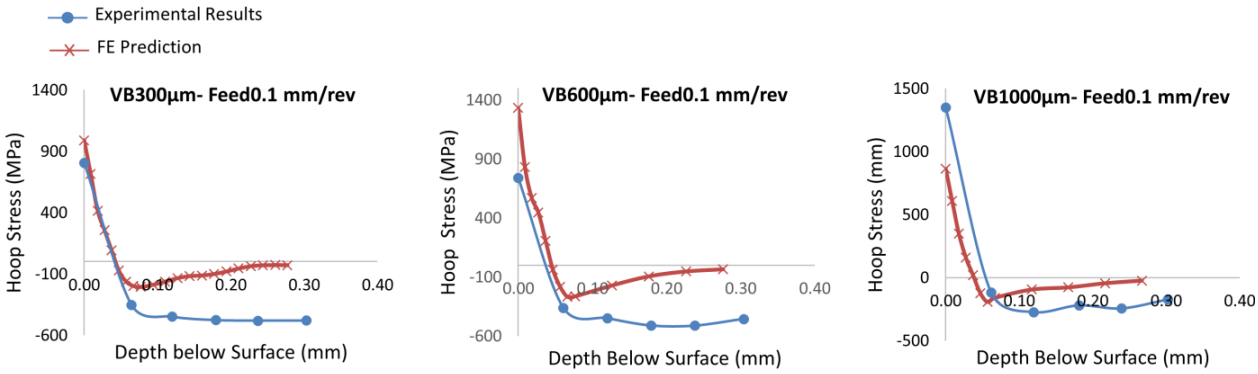

Figure 5-28: Comparison of residual of experiment and FE prediction in 3 different wear conditions, feed (=0.1mm/rev) cutting speed (=80m/min) and depth of cut (=0.1mm) are constants

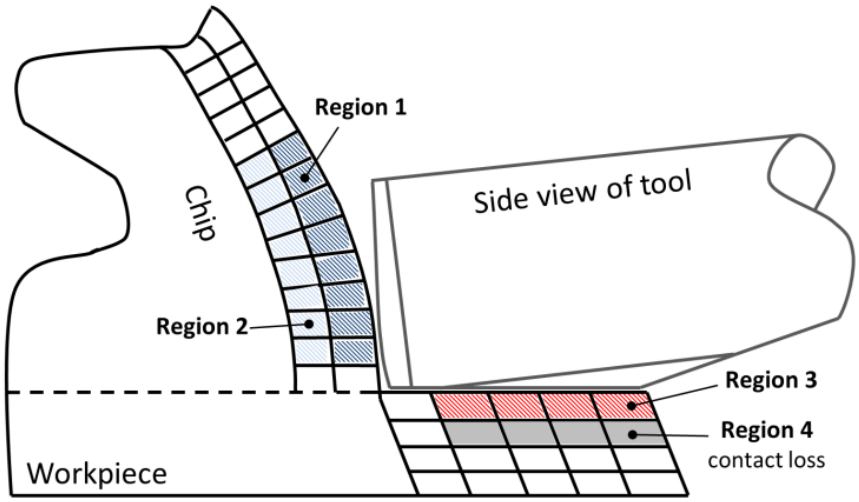

Figure 5-29: Loss of contact between tool and workpiece, the plowing frictional effect cannot be captured since element of region 3 are deleted during simulation and contact loss occurs at region 4

The maximum tensile residual stress at the surface and minimum compressive residual stress beneath the surface for both experiment and prediction are compared in

Table 5.8: Comparison of maximum tensile stress and minimum compressive stress of experiments and FE model

	$\sigma_{tensile}$ [MPa]			$\sigma_{compressive}$ [MPa]		
	Cutting speed 80m/min, depth of cut 0.1mm					
Feed [mm/rev]	0.05	0.1	0.15	0.05	0.1	0.15
Experiment	+854	+1204	+1447	-78	-138	-82
FE Prediction	+461	+1049	+1144	-159	-206	-167
	Cutting speed 80m/min, depth of cut 0.1mm, feed 0.1 mm/rev					
Flank wear width [µm]	300	600	900	300	600	900
Experiment	+807	+741	+1353	-480	-511	-272
FE Prediction	+987	+1333	+863	-207	-268	-192

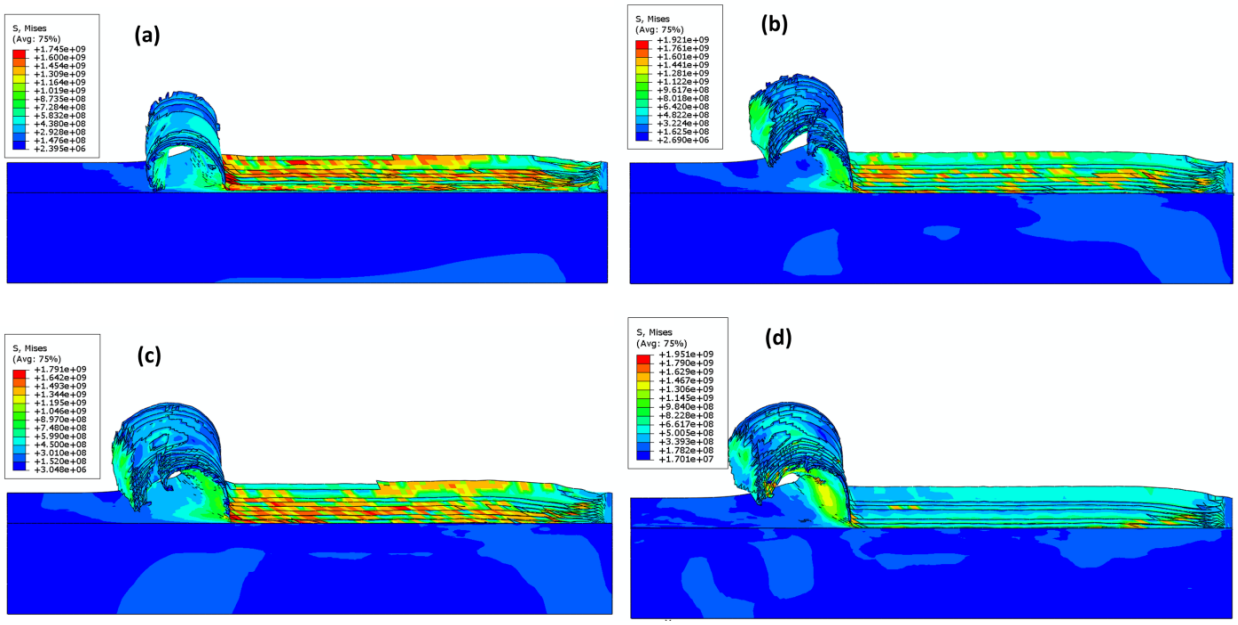

Figure 5-30: Equivalent stress with chip curl in FE model, (a) using sharp tool, (b) worn tool with 300µm wear width, (c) worn tool with 600µm wear width, and (d) worn tool with 900µm wear width

Concluding Remarks

In this chapter a comprehensive study of the tool flank wear and tool flank wear rate estimation was conducted using the Extended Kalman filter (EKF). It was shown that the EKF provides a robust framework for estimating states of the system in the presence of noise. In addition, a comprehensive study on surface integrity parameters for IN718 under the influence of tool flank wear was conducted. Three critical factors that determines the state of health of machining a IN718 bar were selected: surface roughness as a representation of surface quality, diametrical deviation from the target diameter as a representation of dimensional integrity, and residual stress as a representation of surface/subsurface damage. Each of these parameters were studied in the presence of the

tool flank wear as the major factor affecting tool life and productivity rate of the process. The following are the summary and conclusions of this chapter:

- A large number of experiments was conducted to quantify the uncertainty function of the tool wear. The state and measurement models were found based on four replication sets of the feeds 0.05, 0.1 and 0.15mm/rev. An analytical solution was derived for the nonlinear function of the state model in addition to a linear function for the measurement model.
- It was observed that up to the average tool wear width of 200-250μm, the uncertainty decreases followed by an increase beyond this value. The uncertainty in the state model was quantified with a failure probability function, as a bathtub curve. This uncertainty was however considered constant for the measurement model based on the experimental observations.
- The EKF performance was tested in 4 validation tests, and less than 0.06 mm^2 RMSE was observed for the tool wear width estimation. All of the experimental results remained in the 95% prediction interval of the EKF.
- Two probabilistic-based methods (*i.e.*, EKF-based and naïve Bayes), along with a deterministic-based method (SVM) were used for diameter deviation classification and it was shown that the EKF-based method works better for classifying “acceptable” and “major rework with inspection” classes while naïve Bayes works better in classifying “rework” class.

- The effect of wear on surface roughness was studied with an ANOVA test, and it was shown that the tool wear does not have significant effect on surface roughness.
- Residual stress due to sharp and worn tool was modeled in an FE simulation, and the predictions were validated with experimental results. It was shown that the FE model works well in predicting residual stresses when using sharp tool; however it was unable to predict the existence of compressive stresses beneath the cutting surface accurately using the worn tool. It is believed that this is due the element deletion computational artifact and consequent loss of contact at the surface of workpiece and flank face of the tool.

CHAPTER SIX

6. SUMMARY AND CONCLUSIONS

The objective of this research was first to investigate the applicability and advantage of statistical state estimation methods for predicting tool wear in machining nickel-based superalloys over deterministic methods, and second to study the effects of cutting tool wear on one the quality of the part. This work aimed to use a probabilistic methodology for estimating tool wear in machining nickel-based hard-to-machine superalloys. The probabilistic-based method was used in two machining operations: milling and turning. For milling machining, the mechanisms of tool failure were first identified, and based on the rapid catastrophic failure of the tool, a Bayesian inference method (*i.e.*, Markov Chain Monte Carlo, MCMC) was used for tool wear through power model calibration. The Bayesian inference method is a powerful tool as compared to Frequentist deterministic methods where few experimental results are available or when running experiments are highly expensive. Both of these features applied to Ni-based alloys, since their high strength and rapid work-hardening shortens tool life significantly, which limits the availability of data before tool failure. Also, these alloys are expensive materials; it is therefore cost-effective to lower the total number of experiments for model parameter calibration. The model based on Bayesian inference was later used in the state space probabilistic framework of the Kalman filter to estimate tool flank wear.

The possibility of using an on-machine laser measuring system as a direct measuring technique of tool geometry was also studied in this work. The laser system rapidly reads the length of the tool before and after the cutting process. The geometry of the tool makes

it possible to correlate the laser reading (*i.e.*, tool length change) with the width of the flank wear. The information from the laser measuring system was then fused as an additional sensory information source into the Kalman filter measurement model, and significant improvement was obtained using this direct measuring method combined with an indirect method (*i.e.*, spindle power measurements).

The behavior of progressive wear was also investigated in a turning operation. Unlike milling with extremely rapid catastrophic tool failure, no catastrophic failure of the tool was observed in turning. Therefore a larger database of tool behavior information could be created. Due to the nonlinear evolution of wear, an extended Kalman filter was used for tracking progressive wear and the results of this probabilistic-based method in predicting flank wear width were compared with a deterministic method; significant improvement was achieved.

To fulfill the second objective of this research in understanding the underlying effects of wear on surface integrity of the Ni-based alloys, a comprehensive study on surface roughness, dimensional deviation and residual stress was conducted. These three parameters taken together represent the workpiece state of health; the tool wear effect on each was investigated. It was shown that unlike the common belief of detrimental effects of wear on surface roughness, tool flank wear did not have a significant effect on the roughness profile of the workpiece. To study the effect of wear on dimensional integrity, the geometrical relation of the tool length change and flank wear width was derived similar to milling and the estimated results of wear from the extended Kalman filter were utilized for classification of dimensional deviation. The results were compared with

another probabilistic-based (*i.e.*, naïve Bayes) and deterministic-based (*i.e.*, Support Vector Machine) classification algorithms. For studying the wear effect on machining-induced residual stresses, a finite element approach was taken. The results of the finite element model for a sharp tool were first validated with the experimental results, and then the sharp tool geometry was updated to represent a worn tool. It was shown that while the sharp tool model has a very good prediction of residual stress profile, the worn tool model exhibits large errors in predicting compressive stress beneath the machined surface. The potential causes of error were discussed and it was concluded that due to the necessary element deletion algorithm in the finite element model a proper plowing frictional effect could not be simulated.

Contributions

The primary contribution of this research is the improvement in traditional tool wear estimation techniques by using probabilistic-based approaches, which led to 60% increase in tool wear estimation accuracy compared to a deterministic spindle power – wear formulation. The low cost of the spindle power sensor as a measurement signal provides a feasible solution for the proposed methodology to be used in industrial machine shops.

The secondary contribution of this work is filling the gap between the effect of wear on the workpiece quality. This is important in online process monitoring of Ni-based materials, since the tool wear can be detrimental to the quality of expensive workpieces. Since tool wear alone does not necessarily reflect the performance of the machining operation, quantifying its effect on part quality in the form of surface quality,

dimensional integrity and residual stress leads to a better decision-making strategy for continuing or stopping the process. Therefore, this approach better guarantees the end-product quality and increases the productivity rate.

Future Impacts

The immediate use of this estimation methodology is in machine shops for tracking tool state of health in terms of wear and wear rate. Since visual inspection of the tool is costly in practice, the current suboptimal solution is choosing a conservative cutting speed or depth of cut in machining expensive materials to avoid tool breakage or damage during the operation. Using the proposed method makes tracking tool wear possible and therefore lets the operator increase the productivity by increasing cutting speed or depth of cut. Moreover, the FE approach along with a proposed strategy for classifying wear-induced dimensional tolerances of the workpiece can provide additional information about the workpiece integrity and depth of machining affected zone. In a larger scale the uncertainty quantification method implemented in this work can be extended to any application involves large variations/uncertainty, specifically in design of critical parts [114-116] or lack of knowledge due to complexity of problems in manufacturing domains [117-120].

The output of this research produces a general knowledge of the performance of an individual machine in a production line. This information can be collected and analyzed based on the rate of tool change or rate of part scrap, which enables the profitability maximization in the machining operation.

GE Global research recently published an article about five targets that need to be achieved in their 2020 vision [121]:

- **Internet**: hyper connectivity; a living network of the world's machines, data & people
- **Brilliant Machines**: Increasing system intelligence through embedded software, advanced sensors, controls and software applications
- **Big Data**: Democratization of data, high frequency, real-time data
- **Analytics**: Predictive algorithms, physics-based analytics, deep domain expertise on big industrial data
- **People at Work**: Connecting people at work or on the move; Supporting more intelligent design, higher service quality operations, & safety maintenance

GE defines the idea of a brilliant factory as in Figure 6-1. An intelligent system combined with advanced sensors (Brilliant Machines) that have predictive ability (Analytics) to use algorithms in real-time (Big Data) to identify and mitigate faults. The output of this research is beneficial for large manufacturing plants such as GE, where high productivity and at the same time good quality of products is the end-goal.

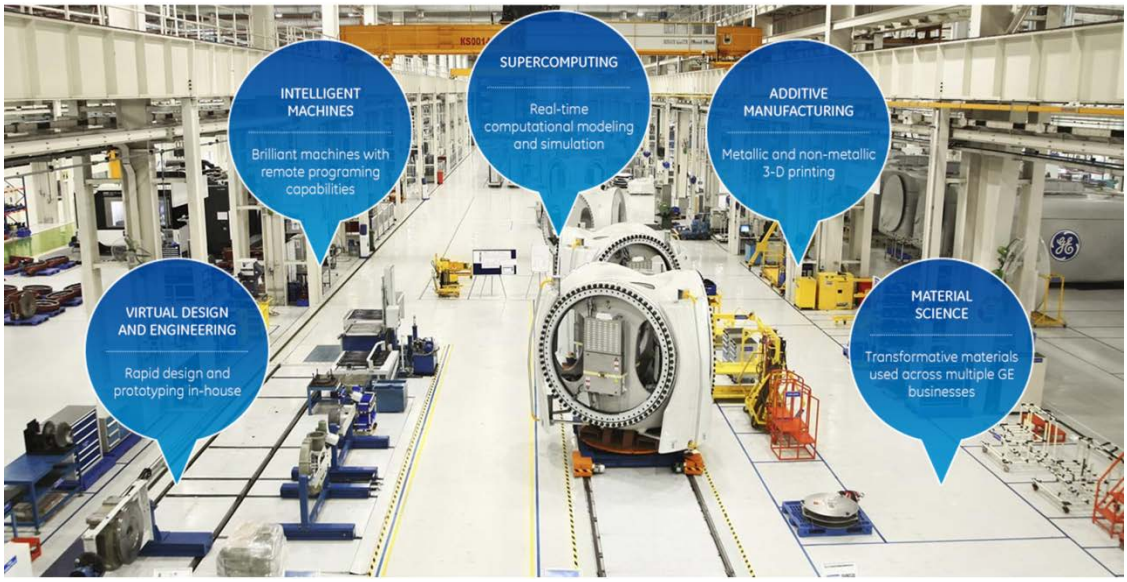

Figure 6-1: GE 2020 brilliant factory [122]

Bounds of Applicability

The power-tool wear model that was used in this research can be easily applied to any machining operation; however the model coefficients are derived based on experimental results and are dependent on many factors such as the tool geometry, coating, material and cutting conditions. Therefore offline testing methods are required for calibrating the measurement model. The same applies to progressive wear models. As shown in Chapters 4 and 5, the progressive wear curves are completely different from milling (a linear curve until catastrophic failure at about 200-250µm of tool wear width) to turning (nonlinear curve with catastrophic failure up to 900µm of flank wear width). Therefore a unique equation for tool wear progress does not exist and should be derived empirically. Moreover, the laser measuring unit that was used in the milling operation is not a common measuring system in CNC machines and therefore its availability for use for estimation framework is limited.

To eliminate the poor repeatability that was observed in surface roughness results, a very large number of experiments and additional investigation into underlying causes of variability for the same condition are required to make a trend between roughness and wear observable. The excruciating and slow measurement process for surface roughness characterization is one aspect that hinders the pace of further investigation. Moreover, additional replication of residual stress testing in different cutting conditions and wear width values can provide a better insight on the validity of FE model. This could not be accomplished since the cost of residual stress testing is extremely high.

Recommendations

The following are some of the recommendations for future work:

- The Bayesian inference from this work can be used for identifying the probability distribution of the power model for a group of Ni-based alloys, ranging from annealed IN718 with mechanical properties close to stainless steel to GTD-111 as one of the hardest-to-machine superalloys. The probability distribution of power model parameters will eventually act as a prior belief function for quick and inexpensive calibration of unknown superalloys. This also can be applied in different alloys such as titanium-based alloys to establish a general library of hard-to-machine materials.
- In addition to variable feed; cutting speed and depth of cut can also be varied to find a more general and more robust form of the progressive wear model.
- The coolant effect in FE model was considered as a simple heat convection problem; however this can be modeled as a CFD simulation coupled with

thermal-displacement chip formation analysis to accurately model the coolant effect on residual stress and forces.

- The effect of temperature as one of the driving factors in rapid wear rate of the Ni-based alloys can be included into the modeling scheme. Validation experiments require embedded micro-sensors such as Figure 6-2 where the thermocouple is embedded on the rake face of the tool to read the contacting temperature in cutting.

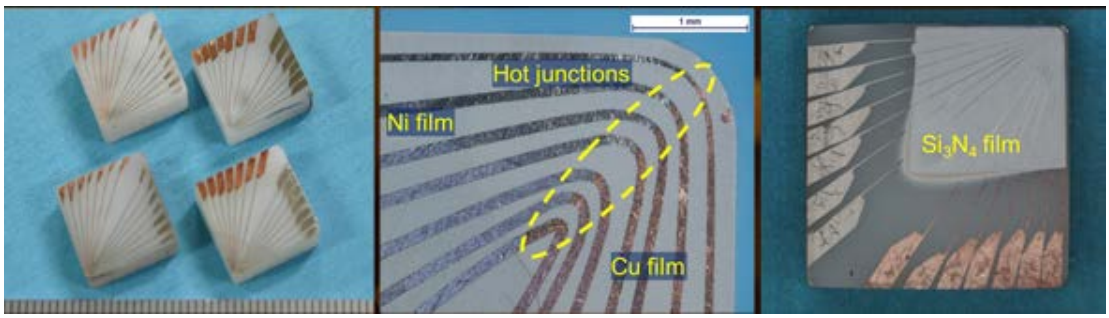

Figure 6-2: Embedded thermocouple on the rake face of the tool (courtesy of Jun Shinozuka, Yokohama National University, Japan)

7. APPENDICES

APPENDIX A: FEM Results

Temperature and stress profile of FE prediction in different wear conditions.

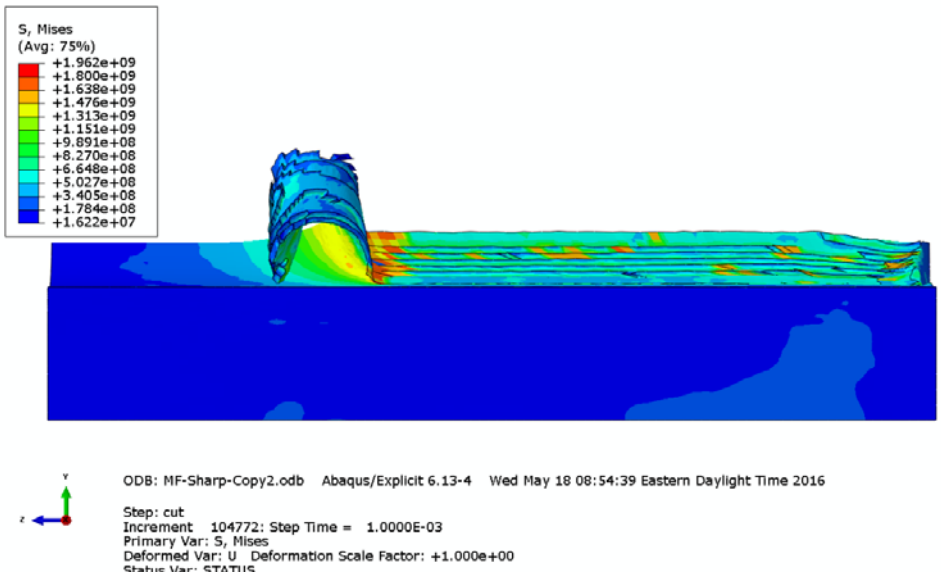

Figure 7-1: Equivalent von-Mises stress prediction for sharp tool – Feed 0.1mm/rev, depth of cut 0.1mm and cutting speed 80m/min

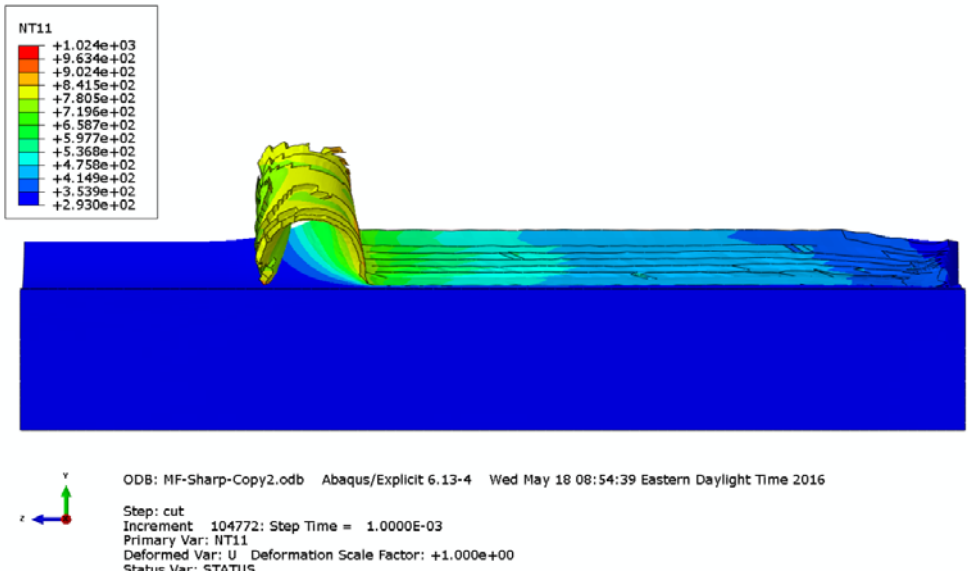

Figure 7-2: Nodal Temperature prediction for sharp tool – Feed 0.1mm/rev, depth of cut 0.1mm and cutting speed 80m/min

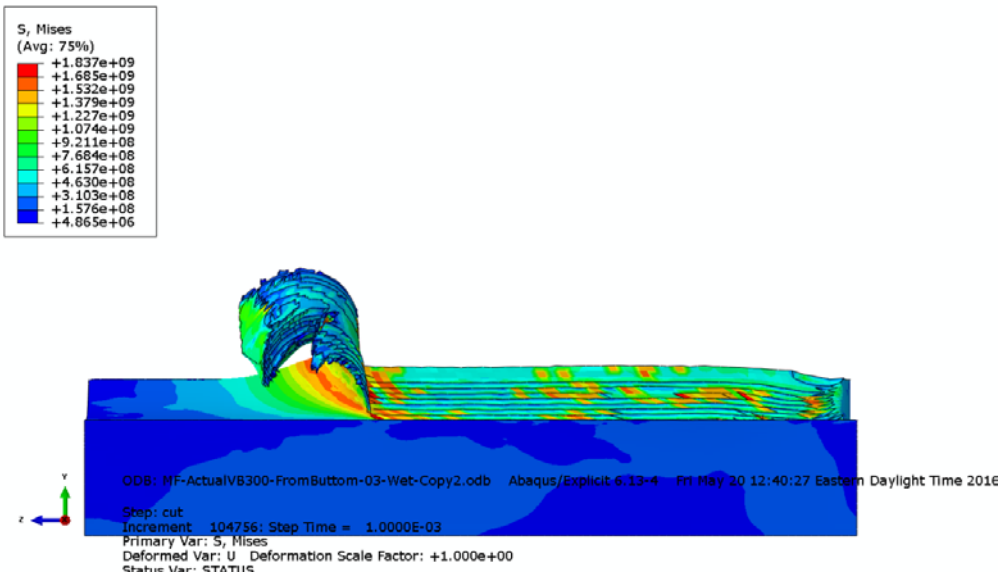

Figure 7-3: Equivalent von-Mises stress prediction for worn tool – Feed 0.1mm/rev, depth of cut 0.1mm, cutting speed 80m/min, and wear width 300µm

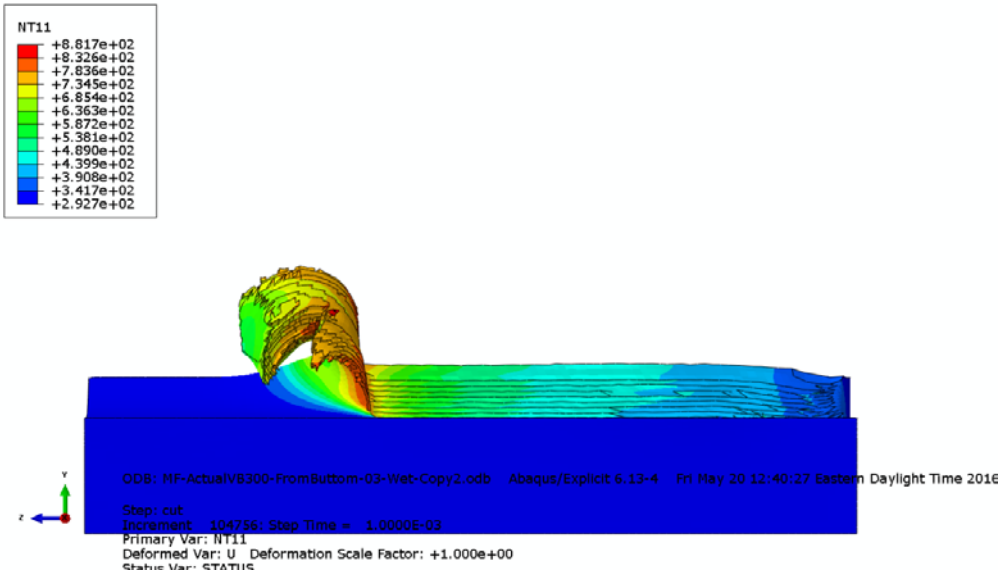

Figure 7-4: Nodal Temperature prediction for worn tool – Feed 0.1mm/rev, depth of cut 0.1mm, cutting speed 80m/min, and wear width 300µm

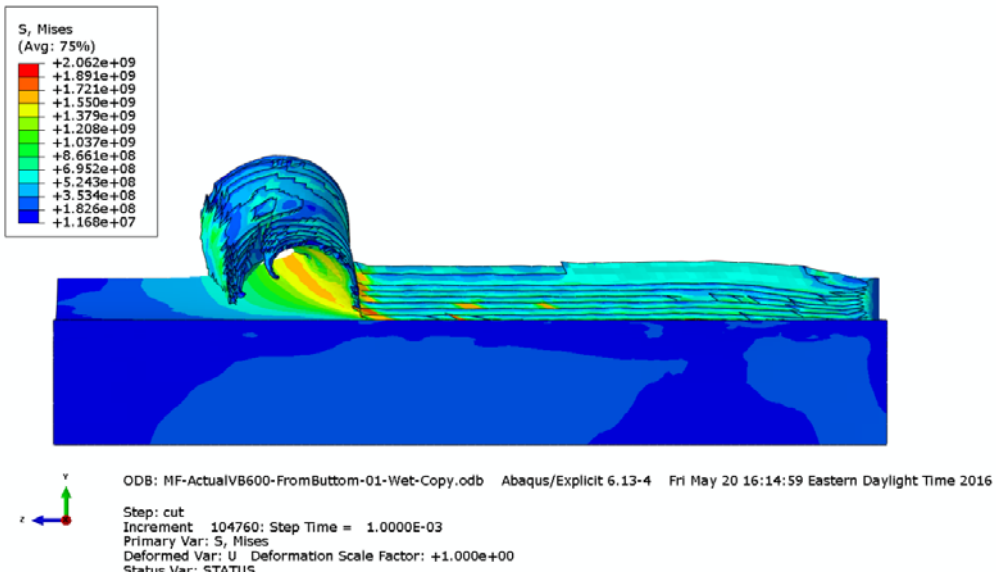

Figure 7-5: Equivalent von-Mises stress prediction for worn tool – Feed 0.1mm/rev, depth of cut 0.1mm, cutting speed 80m/min, and wear width 600µm

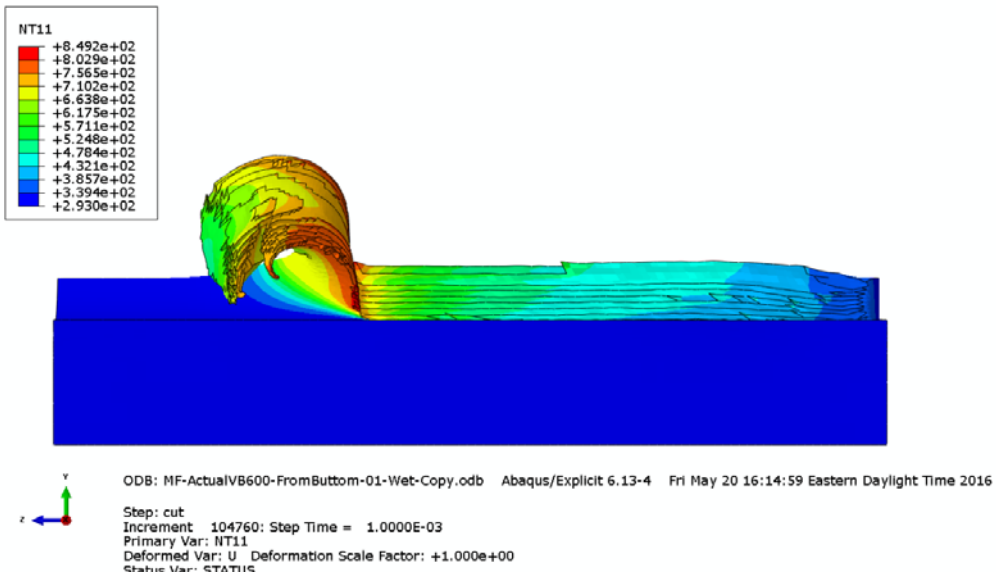

Figure 7-6: Nodal Temperature prediction for worn tool – Feed 0.1mm/rev, depth of cut 0.1mm, cutting speed 80m/min, and wear width 600µm

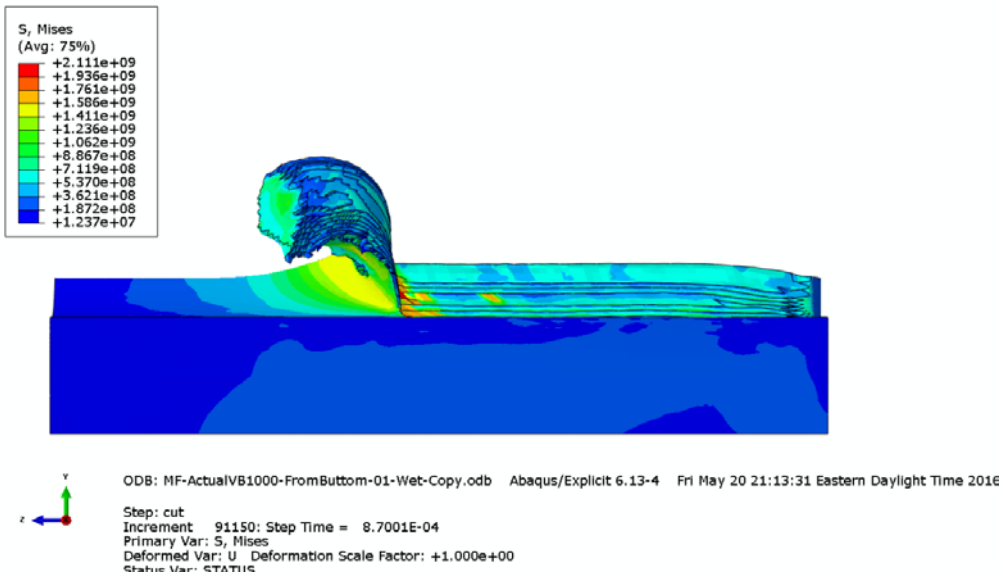

Figure 7-7: Equivalent von-Mises stress prediction for worn tool – Feed 0.1mm/rev, depth of cut 0.1mm, cutting speed 80m/min, and wear width 900µm

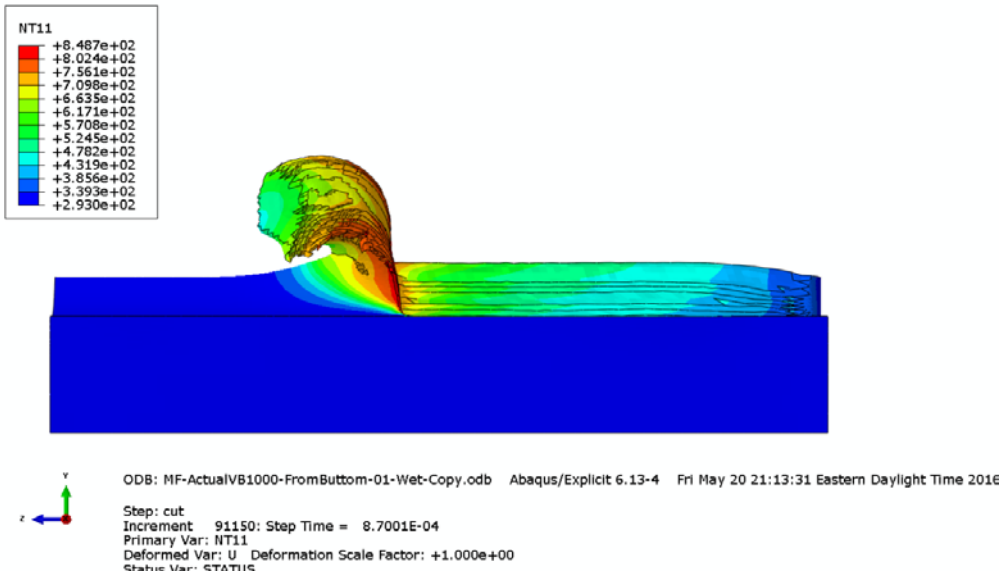

Figure 7-8: Nodal Temperature prediction for worn tool – Feed 0.1mm/rev, depth of cut 0.1mm, cutting speed 80m/min, and wear width 900µm

APPENDIX B: G-code for milling

Below is the main code for slot-milling Rene 108 on OKUMA CNC machine:

```
O0603(MEASURE ON BLUM LASER)
N20 M3 S3000 (ROTATE SPINDLE)
N30 G15 H1 (ACTIVATE WORK OFFSET)
N40 G04 F=2.
CALL O9603 PH=22. PE=0 PD=22. PB=3 PA=3 PR=0.001 PZ=.20 PX=.0000
N60 G15H96
N70 G56H22
N80 M1
(PREPASS)
N90 G95
N100 M3S1003
N110 M8
N130 G0 X-6 Y-20 Z1000
N140 G0 X-6 Y-20 Z3.5
N150 G1 X-6 Y-20 Z15 F0.1 (CHANGE DEPTH OF CUT Z=-0.5)
N160 G1 X-6 Y75 F0.5
N170 G0 X-6 Y75 Z1000
N200 M1
(CHANGE INSERTS)
(TEST M1)
O0603 (MEASURE ON BLUM LASER)
N220 M3 S3000 (ROTATE SPINDLE)
N230 G15 H1 (ACTIVATE WORK OFFSET)
N240 G04 F=2.
CALL O9603 PH=22. PE=0 PD=22. PB=3 PA=3 PR=0.001 PZ=.20 PX=.0000
N260 G15H96
N270 G56H22
N280 M1
N290 G95
N300 M3S602
N310 M08
N320 G0 X3.5 Y-20 Z1000
N330 G0 X3.5 Y-20 Z3.5
N340 G1 X3.5 Y-20 Z-0.5 F0.1
N350 G1 X3.5 Y75 F0.1
```

```
N360 G0 X3.5 Y75 Z1000
M30
```

APPENDIX C: G-code for turning

Below is the main code for face-turning IN718 on OKUMA CNC lathe machine:

```
G140
G95
G18 (XZ PLANE)
G50 M42 S600 T0404
(HIGH GEAR RANGE_ MAX SPINDLE SPEED_ TOOL SELECTION)
G97 S300 M03 (JUST ROTATING)
N05 DIAO=38
N06 DIAI=0 (INNER DIAMETER)
N07 ROT=80 (M/MIN)
N08 FEED=0.05 (MM/REV)
N09 DOC=0.0 (DEPTH OF CUT_ MM)
M09 (COOLANT OFF)
G01 X300 F10
G01 Z300 F10
G01 X300 Z=0.5 F5 (APPROACHING PART FACE)(CHANGE Z IN DIFFERENT
CASES)
M08 (COOLANT ON)
(PREPARE DAQ)(OPTIONAL STOP _ CHECK)
(CUTTING PROCESS)
G01 X=DIAO+10 F5 (FACE )
G96 S=ROT M03 (CONSTABT CUTTING SPEED _ M/MIN)
G01 Z=-DOC F5  (DOC OF FACING)
G01 X=DIAI F=FEED (FACING UP TO INNER DIAMETER)
(G01 X=DIAI+2.0 F=FEED) (GO UP A LITTLE BIT)
G97 S500 M03 (CHANGE TO RPM)
G01 Z100 F10  (TOOL GOES RIGHT)
(G01 X300 F10)  (TOOL GOES UP)
M09
(G01 X-71 Z266 F5) (MEASURE FLANK WEAR)
(M01)
(G01 X151 Z266 F5) (MEASURE CRATER WEAR)
M05 (STOP THE SPINDLE)
M30 (STOP THE PROGRAM)
```

Below is the main code for bar-turning IN718 on OKUMA CNC lathe machine:

```
G140
G95
G18 (XZ PLANE)
G50 M42 S1500 T0404
M3S500 (JUST ROTATING)
N05 DIAM=31.00(CHANGE THIS MARTIN - DIAMETER)
N06 ROT=80 (M/MIN)
N07 FEED=0.1 (MM/REV)
M09 (COOLANT OFF)
G01 X300 Z300 F20
G01 X300 Z20 F5 (APPROACHING PART FACE)(CHANGE Z IN DIFFERENT
CASES)
M09 (COOLANT ON)
(PREPARE DAQ)(OPTIONAL STOP _ CHECK)
M01
(CUTTING PROCESS)
G01 X=DIAM F5 (CHANAGE DEPTH OF CUT)
G96 S=ROT M03 (CONSTABT CUTTING SPEED _ M/MIN)
G01 Z-49 F=FEED  (CUTTING)(BE CAREFUL HERE WITH Z)
G01 X=DIAM+1 F=FEED (GOING UP)
G97 S200 M03 (CHANGE TO RPM)
G01 Z200 F10  (TOOL GOES UP)
(G01 X300 F10)  (TOOL GOES RIGHT)
M05 (STOP THE SPINDLE)
M30 (STOP THE PROGRAM)
```

REFERENCES

[1] Shifler, D. 2009, "Future Research Directions to Understanding Factors Influencing Advanced High Temperature Materials", *2009 DoD Corrosion Conference*, pp. 1-26.

[2] Ulutan, D. & Ozel, T. 2011, "Machining induced surface integrity in titanium and nickel alloys: A review", *International Journal of Machine Tools and Manufacture*, vol. 51, no. 3, pp. 250-280.

[3] Thakur, A. & Gangopadhyay, S. 2016, "State-of-the-art in surface integrity in machining of nickel-based super alloys", *International Journal of Machine Tools and Manufacture*, vol. 100, pp. 25-54.

[4] Vallejo Jr, A.G., Nolazco-Flores, J.A., Morales-Menéndez, R., Sucar, L.E. & Rodríguez, C.A. 2005, "Tool-wear monitoring based on continuous hidden Markov models" in *Progress in Pattern Recognition, Image Analysis and Applications* Springer, , pp. 880-890.

[5] Guo, Y., Li, W. & Jawahir, I. 2009, "Surface integrity characterization and prediction in machining of hardened and difficult-to-machine alloys: a state-of-art research review and analysis", *Machining Science and Technology*, vol. 13, no. 4, pp. 437-470.

[6] Pollock, T.M. & Tin, S. 2006, "Nickel-based superalloys for advanced turbine engines: chemistry, microstructure and properties", *Journal of Propulsion and Power*, vol. 22, no. 2, pp. 361-374.

[7] Banerjee, R. 2011, *Mechanism Of Ordered Gamma Prime Precipitation in Nickel Based Superalloys*, University of North Texas.

[8] Bowman, R. 2000, , *Superalloys: A Primer and History* [Homepage of The Minerals, Metals & Materials Society], [Online]. Available: http://www.tms.org/meetings/specialty/superalloys2000/superalloyshistory.html [2016, January/4].

[9] Doi, M., Miki, D., Moritani, T. & Kozakai, T. 2004, "Gamma/Gamma-Prime Microstructure Formed by Phase Separation of Gamma-Prime Precipitates in a Ni-Al-Ti Alloy", *Superalloys 2004,* , pp. 109-114.

[10] Ulutan, D., Pleta, A., Bardis, V., Akhavan Niaki F. & Mears, L. 2014, *Machining Process Monitoring on Nickel-Based Superalloys, Phase VIII Final Report* , CUICAR/GE.

[11] Henderson, A. 2012, *Updated Force Model for Milling Nickel-based Superalloys*, Clemson University.

[12] Childs, T., Maekawa, K. & Maulik, P. 1988, "Effects of coolant on temperature distribution in metal machining", *Materials Science and Technology,* vol. 4, no. 11, pp. 1006-1019.

[13] ISO-8688, 1. 1989, *ISO 8688-1:1989 - Tool life testing in milling -- Part 1: Face milling*, International Standard Organization (ISO).

[14] Zhu, D., Zhang, X. & Ding, H. 2013, "Tool wear characteristics in machining of nickel-based superalloys", *International Journal of Machine Tools and Manufacture,* vol. 64, pp. 60-77.

[15] Akhtar, W., Sun, J., Sun, P., Chen, W. & Saleem, Z. 2014, "Tool wear mechanisms in the machining of Nickel based super-alloys: A review", *Frontiers of Mechanical Engineering*, vol. 9, no. 2, pp. 106-119.

[16] Liao, Y. & Shiue, R. 1996, "Carbide tool wear mechanism in turning of Inconel 718 superalloy", *Wear*, vol. 193, no. 1, pp. 16-24.

[17] Song, X.Y. & Zhao, J. 2010, "Failure Mechanisms of Carbide Tool in High Speed Milling of Inconel 718", *Advanced Materials Research*Trans Tech Publ, , pp. 1920.

[18] Jianxin, D., Lili, L., Jianhua, L., Jinlong, Z. & Xuefeng, Y. 2005, "Failure mechanisms of TiB 2 particle and SiC whisker reinforced Al 2 O 3 ceramic cutting tools when machining nickel-based alloys", *International Journal of Machine Tools and Manufacture*, vol. 45, no. 12, pp. 1393-1401.

[19] Usui, E., Shirakashi, T. & Kitagawa, T. 1978, "Analytical prediction of three dimensional cutting process—Part 3: Cutting temperature and crater wear of carbide tool", *Journal of Manufacturing Science and Engineering*, vol. 100, no. 2, pp. 236-243.

[20] Devillez, A., Schneider, F., Dominiak, S., Dudzinski, D. & Larrouquere, D. 2007, "Cutting forces and wear in dry machining of Inconel 718 with coated carbide tools", *Wear*, vol. 262, no. 7, pp. 931-942.

[21] Li, L., He, N., Wang, M. & Wang, Z. 2002, "High speed cutting of Inconel 718 with coated carbide and ceramic inserts", *Journal of Materials Processing Technology*, vol. 129, no. 1, pp. 127-130.

[22] Chen, X. & Li, H. 2009, "Development of a tool wear observer model for online tool condition monitoring and control in machining nickel-based alloys", *The International Journal of Advanced Manufacturing Technology*, vol. 45, no. 7-8, pp. 786-800.

[23] Ezugwu, E., Wang, Z. & Machado, A. 1999, "The machinability of nickel-based alloys: a review", *Journal of Materials Processing Technology*, vol. 86, no. 1, pp. 1-16.

[24] Huang, Y. & Liang, S.Y. 2004, "Modeling of CBN tool flank wear progression in finish hard turning", *Journal of manufacturing science and engineering*, vol. 126, no. 1, pp. 98-106.

[25] Costes, J., Guillet, Y., Poulachon, G. & Dessoly, M. 2007, "Tool-life and wear mechanisms of CBN tools in machining of Inconel 718", *International Journal of Machine Tools and Manufacture*, vol. 47, no. 7, pp. 1081-1087.

[26] Ezugwu, E.,O., Bonney, J. & Yamane, Y. 2003, "An overview of the machinability of aeroengine alloys", *Journal of Materials Processing Technology*, vol. 134, no. 2, pp. 233-253.

[27] Li, H., Zeng, H. & Chen, X. 2006, "An experimental study of tool wear and cutting force variation in the end milling of Inconel 718 with coated carbide inserts", *Journal of Materials Processing Technology*, vol. 180, no. 1, pp. 296-304.

[28] Khidhir, B.A. & Mohamed, B. 2010, "Machining of nickel based alloys using different cemented carbide tools", *Journal of Engineering science and technology*, vol. 5, no. 3, pp. 264-271.

[29] Kasim, M.S., Haron, C.C., Ghani, J., Sulaiman, M. & Yazid, M. 2013, "Wear mechanism and notch wear location prediction model in ball nose end milling of Inconel 718", *Wear,* vol. 302, no. 1, pp. 1171-1179.

[30] Lim, S. 1998, "Recent developments in wear-mechanism maps", *Tribology International,* vol. 31, no. 1, pp. 87-97.

[31] Lim, C., Lim, S. & Lee, K. 1999, "Wear of TiC-coated carbide tools in dry turning", *Wear,* vol. 225, pp. 354-367.

[32] Jaffery, S. & Mativenga, P. 2009, "Study of the use of wear maps for assessing machining performance", *Proceedings of the Institution of Mechanical Engineers, Part B: Journal of Engineering Manufacture,* vol. 223, no. 9, pp. 1097-1105.

[33] Kuttolamadom, M. 2012, *Prediction of the Wear & Evolution of Cutting Tools in a Carbide/Ti-6Al-4V Machining Tribosystem by Volumetric Tool Wear Characterization & Modeling,* Clemson University.

[34] Sharman, A., Hughes, J. & Ridgway, K. 2006, "An analysis of the residual stresses generated in Inconel 718™ when turning", *Journal of Materials Processing Technology,* vol. 173, no. 3, pp. 359-367.

[35] Outeiro, J., Pina, J., M'saoubi, R., Pusavec, F. & Jawahir, I. 2008, "Analysis of residual stresses induced by dry turning of difficult-to-machine materials", *CIRP Annals-Manufacturing Technology,* vol. 57, no. 1, pp. 77-80.

[36] Kortabarri, A., Madariag, A., Fernandez, E., Esnaol, J. & Arrazola, P. 2011, "A comparative study of residual stress profiles on Inconel 718 induced by dry face turning", *Procedia Engineering,* vol. 19, pp. 228-234.

[37] Ranganath, S., Guo, C. & Holt, S. 2009, "Experimental investigations into the carbide cracking phenomenon on Inconel 718 superalloy material", *ASME 2009 International Manufacturing Science and Engineering Conference*American Society of Mechanical Engineers, , pp. 33.

[38] Taylor, F.W. 1907, "The art of cutting metals", *Scientific American*, vol. 63, pp. 25942-25944.

[39] Yen, Y., Söhner, J., Lilly, B. & Altan, T. 2004, "Estimation of tool wear in orthogonal cutting using the finite element analysis", *Journal of Materials Processing Technology*, vol. 146, no. 1, pp. 82-91.

[40] Takeyama, H. & Murata, R. 1963, "Basic investigation of tool wear", *Journal of Manufacturing Science and Engineering*, vol. 85, no. 1, pp. 33-37.

[41] Koren, Y., Ko, T., Ulsoy, A.G. & Danai, K. 1991, "Flank wear estimation under varying cutting conditions", *Journal of dynamic systems, measurement, and control*, vol. 113, no. 2, pp. 300-307.

[42] Kramer, B.M. & von Turkovich, B.F. 1986, "A Comprehensive Tool Wear Model", *CIRP Annals - Manufacturing Technology*, vol. 35, no. 1, pp. 67-70.

[43] Attanasio, A., Ceretti, E., Rizzuti, S., Umbrello, D. & Micari, F. 2008, "3D finite element analysis of tool wear in machining", *CIRP Annals-Manufacturing Technology*, vol. 57, no. 1, pp. 61-64.

[44] Xiaoli, L. 1999, "On-line detection of the breakage of small diameter drills using current signature wavelet transform", *International Journal of Machine Tools and Manufacture*, vol. 39, no. 1, pp. 157-164.

[45] Alaniz-Lumbreras, P.D., Gómez-Loenzo, R.A., Romero-Troncoso, R.d.J., Peniche-Vera, R.d.R., Jáuregui-Correa, J.C. & Herrera-Ruiz, G. 2006, "Sensorless detection of tool breakage in milling", *Machining Science and Technology*, vol. 10, no. 2, pp. 263-274.

[46] Segreto, T., Simeone, A. & Teti, R. 2012, "Sensor fusion for tool state classification in nickel superalloy high performance cutting", *Procedia CIRP*, vol. 1, pp. 593-598.

[47] Teti, R., Jemielniak, K., O'Donnell, G. & Dornfeld, D. 2010, "Advanced monitoring of machining operations", *CIRP Annals-Manufacturing Technology*, vol. 59, no. 2, pp. 717-739.

[48] Wang, M. & Wang, J. 2012, "CHMM for tool condition monitoring and remaining useful life prediction", *The International Journal of Advanced Manufacturing Technology*, vol. 59, no. 5-8, pp. 463-471.

[49] Segreto, T., Simeone, A. & Teti, R. 2013, "Multiple sensor monitoring in nickel alloy turning for tool wear assessment via sensor fusion", *Procedia CIRP*, vol. 12, pp. 85-90.

[50] Cho, S., Binsaeid, S. & Asfour, S. 2010, "Design of multisensor fusion-based tool condition monitoring system in end milling", *The International Journal of Advanced Manufacturing Technology*, vol. 46, no. 5-8, pp. 681-694.

[51] Trejo-Hernandez, M., Osornio-Rios, R.A., Romero-Troncoso, R.d.J., Rodriguez-Donate, C., Dominguez-Gonzalez, A. & Herrera-Ruiz, G. 2010, "FPGA-based fused smart-sensor for tool-wear area quantitative estimation in CNC machine inserts", *Sensors*, vol. 10, no. 4, pp. 3373-3388.

[52] Kai-feng Zhang, Hui-qun Yuan , Peng Nie 2015, "A method for tool condition monitoring based on sensor fusion", *Journal of Intelligent Manufacturing,* vol. 26, no. 5, pp. 1011-1026.

[53] Scheffer, C., Engelbrecht, H. & Heyns, P. 2005, "A comparative evaluation of neural networks and hidden Markov models for monitoring turning tool wear", *Neural Computing & Applications,* vol. 14, no. 4, pp. 325-336.

[54] Fang, N., Pai, P.S. & Edwards, N. 2012, "Tool-edge wear and wavelet packet transform analysis in high-speed machining of Inconel 718", *Strojniški vestnik-Journal of Mechanical Engineering,* vol. 58, no. 3, pp. 191-202.

[55] Choi, Y., Narayanaswami, R. & Chandra, A. 2004, "Tool wear monitoring in ramp cuts in end milling using the wavelet transform", *The International Journal of Advanced Manufacturing Technology,* vol. 23, no. 5-6, pp. 419-428.

[56] Chuangwen, X. & Hualing, C. 2007, "A research of tool wear recognizing based on wavelet packet pretreated and neural network", *Journal of System Design and Dynamics,* vol. 1, no. 4, pp. 760-770.

[57] Jemielniak, K., Kossakowska, J. & Urbański, T. 2011, "Application of wavelet transform of acoustic emission and cutting force signals for tool condition monitoring in rough turning of Inconel 625", *Proceedings of the Institution of Mechanical Engineers, Part B: Journal of Engineering Manufacture,* vol. 225, no. 1, pp. 123-129.

[58] Schmitz, T.L., Karandikar, J., Kim, N.H. & Abbas, A. 2011, "Uncertainty in machining: Workshop summary and contributions", *Journal of Manufacturing Science and Engineering,* vol. 133, no. 5, pp. 051009.

[59] Li, X. & Patri, K.V. 1999, "Wavelet packet transforms of acoustic emission signals for tool wear monitoring", *Journal for Manufacturing Science & Technology,* vol. 1, no. 2, pp. 89-93.

[60] Kamarthi, S., Kumara, S. & Cohen, P. 2000, "Flank wear estimation in turning through wavelet representation of acoustic emission signals", *Journal of Manufacturing Science and Engineering,* vol. 122, no. 1, pp. 12-19.

[61] Wu, Y. & Du, R. 1996, "Feature extraction and assessment using wavelet packets for monitoring of machining processes", *Mechanical systems and signal processing,* vol. 10, no. 1, pp. 29-53.

[62] Antić, A., Šimunović, G., Šarić, T., Milošević, M. & Ficko, M. 2013, "Model sustava za klasifikaciju trošenja alata pri obradi tokarenjem", *Tehnički vjesnik,* vol. 20, no. 2, pp. 247-254.

[63] He, K., Jia, M.P. & Zhao, Z.Z. 2013, "Quality Monitoring of Surface Roughness and Roundness Using Hidden Markov Model", *Advanced Materials Research*Transaction of Technical Publication in Advanced Materials Research, , pp. 308.

[64] Hong, G., Rahman, M. & Zhou, Q. 1996, "Using neural network for tool condition monitoring based on wavelet decomposition", *International Journal of Machine Tools and Manufacture,* vol. 36, no. 5, pp. 551-566.

[65] Scheffer, C. & Heyns, P. 2004, "An industrial tool wear monitoring system for interrupted turning", *Mechanical Systems and Signal Processing,* vol. 18, no. 5, pp. 1219-1242.

[66] Wang, W., Hong, G., Wong, Y. & Zhu, K. 2007, "Sensor fusion for online tool condition monitoring in milling", *International Journal of Production Research*, vol. 45, no. 21, pp. 5095-5116.

[67] Patra, K., Pal, S.K. & Bhattacharyya, K. 2007, "Application of wavelet packet analysis in drill wear monitoring", *Machining Science and Technology*, vol. 11, no. 3, pp. 413-432.

[68] Li, P., Hao, C. & Zhu, S. 2007, "Machining tools wear condition detection based on wavelet packet", IEEE International Conference on Machine Learning and Cybernetics, , pp. 1559.

[69] Karandikar, J.M., Abbas, A.E. & Schmitz, T.L. 2014, "Tool life prediction using Bayesian updating. Part 1: Milling tool life model using a discrete grid method", *Precision Engineering*, vol. 38, no. 1, pp. 9-17.

[70] Karandikar, J.M., Abbas, A.E. & Schmitz, T.L. 2014, "Tool life prediction using Bayesian updating. Part 2: Turning tool life using a Markov Chain Monte Carlo approach", *Precision Engineering*, vol. 38, no. 1, pp. 18-27.

[71] Salonitis, K. & Kolios, A. 2013, "Reliability assessment of cutting tools life based on advanced approximation methods", *Procedia CIRP*, vol. 8, pp. 397-402.

[72] Braglia, M. & Castellano, D. 2014, "Diffusion theory applied to tool-life stochastic modeling under a progressive wear process", *Journal of Manufacturing Science and Engineering*, vol. 136, no. 3, pp. 031010.

[73] Braglia, M., Castellano, D. & Frosolini, M. 2014, "Stochastic theory of tool life–Theoretical developments on the injury theory", *International Journal of Mathematical Modelling and Numerical Optimisation,* vol. 5, no. 4, pp. 265-279.

[74] Gilks, W.R., Richardson, S. & Spiegelhalter, D. 1995, *Markov Chain Monte Carlo in Practice*, Taylor & Francis.

[75] Hoff, P.D. 2009, *A First Course in Bayesian Statistical Methods*, Springer.

[76] Andrieu, C., De Freitas, N., Doucet, A. & Jordan, M.I. 2003, "An introduction to MCMC for machine learning", *Machine Learning*, vol. 50, no. 1-2, pp. 5-43.

[77] Metropolis, N., Rosenbluth, A.W., Rosenbluth, M.N., Teller, A.H. & Teller, E. 1953, "Equation of state calculations by fast computing machines", *The Journal of chemical physics*, vol. 21, no. 6, pp. 1087-1092.

[78] Lynch, S.M. 2007, *Introduction to applied Bayesian statistics and estimation for social scientists,* Springer.

[79] Haario, H., Saksman, E. & Tamminen, J. 1999, "Adaptive proposal distribution for random walk Metropolis algorithm", *Computational Statistics*, vol. 14, no. 3, pp. 375-396.

[80] Rosenthal, J.S. 2011, "Optimal proposal distributions and adaptive MCMC", *Handbook of Markov Chain Monte Carlo,* , pp. 93-112.

[81] Haario, H., Saksman, E. & Tamminen, J. 2001, "An adaptive Metropolis algorithm", *Bernoulli,* , pp. 223-242.

[82] Solonen, A. 2006, *Monte Carlo Methods in Parameter Estimation of Nonlinear Model*, Lappeenrant University of Technology.

[83] Mira, A. 2001, "On Metropolis-Hastings algorithms with delayed rejection", *Metron*, vol. 59, no. 3-4, pp. 231-241.

[84] Koenigsberger, F. & Sabberwal, A. 1961, "An investigation into the cutting force pulsations during milling operations", *International Journal of Machine Tool Design and Research*, vol. 1, no. 1, pp. 15-33.

[85] Kline, W., DeVor, R. & Lindberg, J. 1982, "The prediction of cutting forces in end milling with application to cornering cuts", *International Journal of Machine Tool Design and Research*, vol. 22, no. 1, pp. 7-22.

[86] Fu, H.J., DeVor, R.E. & Kapoor, S.G. 1984, "A Mechanistic Model for the Prediction of the Force System in Face Milling Operations", *Journal of Manufacturing Science and Engineering*, vol. 106, no. 1, pp. 81-88.

[87] Fussell, B. & Srinivasan, K. 1989, "An investigation of the end milling process under varying machining conditions", *Journal of Manufacturing Science and Engineering*, vol. 111, no. 1, pp. 27-36.

[88] Altintas, Y. & Yellowley, I. 1989, "In-Process Detection of Tool Failure in Milling Using Cutting Force Models", *Journal of Manufacturing Science and Engineering*, vol. 111, no. 2, pp. 149-157.

[89] Altintas, Y., Spence, A. & Tlusty, J. 1991, "End milling force algorithms for CAD systems", *CIRP Annals-Manufacturing Technology*, vol. 40, no. 1, pp. 31-34.

[90] Shao, H., Wang, H.L. & Zhao, X.M. 2004, "A cutting power model for tool wear monitoring in milling", *International Journal of Machine Tools and Manufacture*, vol. 44, no. 14, pp. 1503-1509.

[91] Choudhury, S. & Rath, S. 2000, "In-process tool wear estimation in milling using cutting force model", *Journal of Materials Processing Technology,* vol. 99, no. 1, pp. 113-119.

[92] Rubenstein, C. 1976, "An Analysis of Tool Life Based on Flank-Face Wear—Part 1: Theory", *Journal of Engineering for Industry,* vol. 98, no. 1, pp. 221-226.

[93] Waldorf, D.J., Kapoor, S.G. & DeVor, R.E. 1992, "Automatic recognition of tool wear on a face mill using a mechanistic modeling approach", *Wear,* vol. 157, no. 2, pp. 305-323.

[94] Sandvik, C. 2006, *Steel milling stars, GC4240 and GC1030, C-1140, A pair of grades that won't crack under pressure*, Sandvik Coromant, Sweden.

[95] Lagarias, J.C., Reeds, J.A., Wright, M.H. & Wright, P.E. 1998, "Convergence properties of the Nelder--Mead simplex method in low dimensions", *SIAM Journal on optimization,* vol. 9, no. 1, pp. 112-147.

[96] Haykin, S.S. 2001, *Kalman filtering and neural networks*, Wiley Online Library.

[97] Mohammadi, H., Ravindra, D. & Patten, J. 2013, "A first investigation of green lasers in Micro-Laser Assisted scratch tests on silicon", *28th Annual Meeting of the American Society for Precision Engineering, ASPE 2013*.

[98] Mohammadi, H., Poyraz, H.B., Ravindra, D. & Patten, J.A. 2014, "An experimental study on single point diamond turning of an unpolished silicon wafer via micro-laser assisted machining", *Advanced Materials Research*Trans Tech Publ, , pp. 175.

[99] 'Mohammadi, H. & Patten, J. 2015, "Micro-laser assisted drilling of single crystal silicon in ductile regime", *American Society for Precision Engineering (ASPE),* .

[100] Mohammadi, H. & Patten, J.A. 2016, "Laser Augmented Diamond Drilling: A New Technique to Drill Hard and Brittle Materials", *Procedia Manufacturing,* vol. 5, pp. 1337-1347.

[101] Wan, E.A. & Van Der Merwe, R. 2000, "The unscented Kalman filter for nonlinear estimation", *IEEE Symposium on Adaptive Systems for Signal Processing, Communications, and Control.*, pp. 153.

[102] Arulampalam, M.S., Maskell, S., Gordon, N. & Clapp, T. 2002, "A tutorial on particle filters for online nonlinear/non-Gaussian Bayesian tracking", *IEEE Transactions on Signal Processing,* vol. 50, no. 2, pp. 174-188.

[103] Wang, P. & Gao, R.X. 2016, "Markov Nonlinear System Estimation for Engine Performance Tracking", *Journal of Engineering for Gas Turbines and Power*, vol. 138, no. 9, pp. 091201.

[104] Wang, P. & Gao, R.X. 2016, "Stochastic Tool Wear Prediction for Sustainable Manufacturing", *Procedia CIRP*, vol. 48, pp. 236-241.

[105] Sun, J., Rahman, M., Wong, Y. & Hong, G. 2004, "Multiclassification of tool wear with support vector machine by manufacturing loss consideration", *International Journal of Machine Tools and Manufacture,* vol. 44, no. 11, pp. 1179-1187.

[106] Cho, S., Asfour, S., Onar, A. & Kaundinya, N. 2005, "Tool breakage detection using support vector machine learning in a milling process", *International Journal of Machine Tools and Manufacture,* vol. 45, no. 3, pp. 241-249.

[107] Fish, R.K., Ostendorf, M., Bernard, G.D. & Castanon, D.A. 2003, "Multilevel classification of milling tool wear with confidence estimation", *IEEE Transactions on Pattern Analysis and Machine Intelligence,* vol. 25, no. 1, pp. 75-85.

[108] Bishop, C.M. 2006, *Pattern Recognition and Machine Learning,* Springer, USA.

[109] Ozel, T., Llanos, I., Soriano, J. & Arrazola, P. 2011, "3D finite element modelling of chip formation process for machining Inconel 718: comparison of FE software predictions", *Machining Science and Technology,* vol. 15, no. 1, pp. 21-46.

[110] Mitrofanov, A., Babitsky, V. & Silberschmidt, V. 2004, "Finite element analysis of ultrasonically assisted turning of Inconel 718", *Journal of Materials Processing Technology,* vol. 153, pp. 233-239.

[111] Lorentzon, J., Järvstråt, N. & Josefson, B. 2009, "Modelling chip formation of alloy 718", *Journal of Materials Processing Technology,* vol. 209, no. 10, pp. 4645-4653.

[112] Byun, T. & Farrell, K. 2003, "Tensile properties of Inconel 718 after low temperature neutron irradiation", *Journal of Nuclear Materials,* vol. 318, pp. 292-299.

[113] Pereira, J.M. & Lerch, B.A. 2001, "Effects of heat treatment on the ballistic impact properties of Inconel 718 for jet engine fan containment applications", *International Journal of Impact Engineering,* vol. 25, no. 8, pp. 715-733.

[114] Shankar, P., Fazelpour, M. & Summers, J. 2013, "An Energy-Based Approach for Design of Meso-Structures with High Shear Flexure", *ASME International Design Engineering Technical Conferences and Computers and Information in Engineering Conference* Portland, OR, DETC2013-12292.

[115] Fazelpour, M. & Summers, J.D. 2014, "Evolution of Meso-Structures for Non-Pneumatic Tire Development: A Case Study", *ASME International Design Engineering Technical Conferences and Computers and Information in Engineering Conference* Buffalo, NY, DETC2014-34184.

[116] Fazelpour, M., Shankar, P. & Summers, J. 2016, "Developing Design Guidelines for Meso-Scaled Periodic Cellular Material Structures Under Shear Loading", *ASME International Design Engineering Technical Conferences and Computers and Information in Engineering Conference* Charlotte, NC, DETC2016-59082.

[117] Antani, K., Madadi, A., Kurz, M.E., Mears, L., Funk, K. & Mayorga, M.E. 2012, "Robust work planning and development of a decision support system for work distribution on a mixed-model automotive assembly line", *ASME 2012 International Manufacturing Science and Engineering Conference collocated with the 40th North American Manufacturing Research Conference and in participation with the International Conference on Tribology Materials and Processing*American Society of Mechanical Engineers, , pp. 613.

[118] Fazelpour, M. & Summers, J.D. 2013, "A comparison of design approaches to meso-structure development", *ASME 2013 International Design Engineering Technical Conferences and Computers and Information in Engineering Conference*American Society of Mechanical Engineers, , pp. V03AT03A052.

[119] Gabriel, T. 2013, "Manufacturing Complexity: The Effects of Common Attributes of Manufacturing System Design on Performance", *Academy of Information and Management Sciences Journal*, vol. 16, no. 1, pp. 75.

[120] Sridhar, S., Fazelpour, M., Gill, A.S. & Summers, J.D. 2016, "Accuracy and Precision Analysis of the Graph Complexity Connectivity Method", *Procedia CIRP*, vol. 44, pp. 163-168.

[121] Immelt, J. 2014, *GE Minds and Machines*, GE Global Research, Niskayuna, NY.

[122] General-Electric 2014, *GE 2014 Annual Report*, General Electric.

List of Journal Articles

[1] **Akhavan Niaki F.**, Michel M., Mears L. (2016) "State of Health Monitoring in Machining: Extended Kalman Filter for Tool Wear Assessment in Turning IN718 Hard-to-Machine Alloy", Journal of Manufacturing Processes, Vol. 24, Part 2, pp. 361-369.

[2] **Akhavan Niaki F.**, Ulutan D., Mears, L. (2016) "Parameter Inference under Uncertainty in End-Milling γ'-Strengthened Difficult-to-Machine Alloy", ASME Journal of Manufacturing Science and Engineering, Vol. 138, No. 8, pp. 061014,1 - 061014,10.

[3] **Akhavan Niaki F.,** Feng L., Ulutan D., Mears, L. (2016) "A Wavelet Based Data-Driven Modeling for Tool Wear Assessment of Difficult to Machine Materials", Int. J. Mechatronics and Manufacturing Systems, Vol. 9, No. 2, pp.97 -121.

[4] **Akhavan Niaki F.**, Ulutan D., Mears, L. (2015) "Stochastic Tool Wear Assessment in Milling Difficult to Machine Alloys", Int. J. Mechatronics and Manufacturing Systems, Vol. 8, Nos. 3/4, pp.134 -159.

[5] **Akhavan Niaki, F.**, Mears, L., "A Probabilistic-Based Study on Fused Direct and Indirect Methods for Tracking Tool Flank Wear on Rene-108, Nickel-Based Alloy", in Press for SAGE Journal of Engineering Manufacture.

[6] **Akhavan Niaki, F.**, Mears, L., "State of Health Monitoring in Machining: A Comprehensive Study on the Effect of Tool Wear on Surface Integrity of IN718 Nickel-based Alloy", Journal of Manufacturing Processes. (Manuscript in progress)

Published Conference Proceedings, Presentations & Posters

[1] **Akhavan Niaki, F.**, Pleta, A., Mears, L., (2015) "Superalloy Machining Tool Wear: State Estimation and Alternative Path Planning for Mitigation" International Conference on Precision, Meso, Micro and Nano Engineering (COPEN 2015), December 10-12, Bombay, India.

[2] **Akhavan Niaki, F.**, Ulutan, D., Mears, L., (2015) "Wavelet Based Multi Sensor Fusion for Tool Condition Monitoring of Hard to Machine Materials using Recurrent Neural Network" IEEE International Conference on Multisensor Fusion and Integration for Intelligent Systems (MFI 2015), September 14-16, 2015, San Diego, California.

[3] **Akhavan Niaki, F.**, Ulutan, D., Mears, L., (2015) "In-Process Tool Flank Wear Estimation in Machining Gamma-Prime Strengthened Alloys Using Kalman Filter" 43rd North American Manufacturing Research Conference (NAMRC 2015), June 8-12, 2015, Charlotte, North Carolina.

[4] **Akhavan Niaki, F.**, Ulutan, D., Mears, L., (2015) "Parameter Estimation Using Markov Chain Monte Carlo Method in Mechanistic Modeling of Tool Wear During Milling" ASME 2015 International Manufacturing Science and Engineering Conference (MSEC 2015), June 8-12, 2015, Charlotte, North Carolina.

[5] Bardis, V., **Akhavan Niaki, F.**, Ulutan, D., Mears, L., (2015) "Investigation of the Relationship Between Vibration Data and Tool Wear During End Milling of Gamma Prime Strengthened Alloys" ASME 2015 Engineering Conference (MSEC 2015), June 8-12, 2015, Charlotte, North Carolina.

[6] **Akhavan Niaki, F.**, Ulutan, D., Mears, L., (2015) “Parameter Estimation in Mechanistic Tool Wear Model: A Bayesian Approach” 2015 TMS Annual Meeting & Exhibition, March 15-19, 2015, Orlando, Florida. (Presentation)

[7] **Akhavan Niaki, F.**, Mears, L., (2015) “Stochastic State and Parameter Estimation for Intelligent Manufacturing Processes” NSF Workshop on Effective State Estimation, John Hopkins University, Baltimore, MD, July 2015. (Poster)

[8] **Akhavan Niaki, F.**, Mehta, P., Mears, L., (2014) “Online Parameter Estimation Using Square Root Unscented Kalman Filter (SR-UKF) in Turning of a Slender Bar,” ASME 2015 International Manufacturing Science and Engineering Confere**n**ce, Detroit, Michigan, June 10-13, 2014. (Poster)